Quark Physics Laboratory, Physics Program,
Graduate School of Advanced Science and Engineering

Master's Thesis

Development and Performance Evaluation of Silicon Strip Detector for Next Generation High Luminosity Heavy-Ion Collision Experiments

Rento Yamada

February 21st 2025

Supervisor: Prof. Yorito Yamaguchi

Chief Examiner: Prof. Yorito Yamaguchi

Vice Examiner: Prof. Ken-Ichi Ishikawa

Abstract

The strong interaction described by Quantum Chromodynamics (QCD) forms various phases of matter, including extreme states such as the Quark-Gluon Plasma and high-density nuclear matter inside a neutron star, depending on a condition of temperature and baryon density. These states are actively studied both experimentally and theoretically. Particularly in the finite baryon density region, where first-principle calculations with lattice QCD are challenging, experimental studies play a crucial role.

The Compressed Baryonic Matter (CBM) experiment at the GSI-FAIR accelerator, a next-generation high-luminosity heavy-ion collision experiment, is scheduled to begin in 2029. The CBM experiment aims to generate and investigate a high-density partonic matter and its propertties using high-intensity heavy-ion beams of up to 1×10^9 Au ions per second. The study in this thesis focuses on the development and performance evaluation of the primary tracking detector in the CBM experiment, the Silicon Tracking System (STS). A STS sensor is a double-sided silicon strip detector with a strip width of $58\,\mu m$ and a thickness of $320\,\mu m$. Charged particle tracks are reconstucted using hits at eight layers of sensors. Due to a large number of particles produced in a heavy-ion collision and the high collision rate, the position resolution, time resolution, and detection efficiency of the STS are critical to the success of the experiment.

Currently, some of STS sensors are installed in the J-PARC E16 experiment as the innermost tracking detector, where they are tested with high-intensity proton beams under a magnetic field. The J-PARC E16 experiment aims to observe a modification in the in-medium spectral functions of vector mesons as a possible signature of chiral symmetry restoration using a high-intensity proton beam of 1×10^{10} protons per 2-second spill. An accurate tracking of electrons and positrons for mass reconstruction is crucial for capturing the mass modification of vector mesons. The use of STS sensors, which has a good time resolution ($\sim 5\,nsec$), is therefore also advantageous for the E16 experiment.

In a test experiment conducted in November 2023 at KEK using an electron beam, A STS sensor achieved a time resolution of approximately $5\,nsec$ and a detection efficiency exceeding 98.5%, confirming that they meet both the performance requirements of the E16 experiment and the design goals of the CBM STS. Subsequently, installation of STS sensors in the E16 experiment was completed in May 2024. During the E16 commissioning run (Run-0e), the STS successfully operated under a magnetic field, confirming its proper functionality. This run was also the first to acquire data using online trigger selection. Furthermore, the analysis of data obtained without a magnetic field showed a detection efficiency of approximately 94% (for a single side of the sensor) associated with reconstructed standalone tracks of the outer tracker (GEM tracker). Future challenges for performance evaluation include further analysis of data obtained under a magnetic field and evaluation of 2D cluster detection efficiency and position resolution using both sides of the sensor.

In preparation for the first physics run of the E16 experiment, scheduled to begin in the spring of 2025, detector adjustments are currently underway.

概要

　量子色力学 (QCD) によって記述される強い相互作用は、多彩な相構造を持つ物質状態を形成し、クォーク・グルーオン・プラズマや中性子星内部の高密度核物質などの極限状況下での物質状態が、実験、理論両面から活発に研究されている。特にバリオン数有限密度領域では、格子 QCD 理論による第一原理計算が難しく、実験研究によって開拓される。

　次世代高輝度重イオン衝突実験として、GSI-FAIR 加速器の Compressed Baryonic Matter (CBM) 実験が 2029 年に開始する。CBM 実験は 1×10^9 金イオン/秒もの大強度重イオンビームを用いて、高密度なパートン物質を生成し、その性質を調べることを目的とする。本研究の目的は CBM 実験主飛跡検出器 Silicon Tracking System (STS) の開発、及びその性能評価である。STS センサはストリップ幅 $58\,\mu m$、厚さ $320\,\mu m$ の両面読み出しのシリコンストリップ検出器であり、センサ 8 層で荷電粒子の飛跡再構成を行う。1 回の重イオン衝突で大量の粒子が生成され、その衝突頻度も高いために STS による荷電粒子位置分解能、時間分解能、検出効率は実験の成否を決める重要な要素である。

　現在、STS センサを J-PARC E16 実験に、最内層の飛跡検出器として実装し、磁場中での大強度ビームを用いた試験を行っている。J-PARC E16 実験は、1×10^{10} 陽子/(2 秒 spill) の大強度の陽子ビームを用いて、原子核内で崩壊したベクトル中間子の質量変化を捉え、カイラル対称性の部分的回復を検証する実験である。この質量変化を捉えるためには、質量再構成に用いる電子・陽電子を、正確にトラッキングすることが重要であり、時間分解能が優れた ($\sim 5\,nsec$) STS センサを実装することは、E16 実験にとっても利点がある。

　2023 年 11 月に行った KEK での電子ビームを用いた動作試験では、時間分解能 $\sim 5\,nsec$、検出効率 98.5%以上を達成し、E16 実験の要求性能および CBM STS の設計目標を満たすことを確認した。続けて 2024 年 5 月に E16 への実装を完了し、E16 の検出器動作試験運転では、磁場環境下での STS の正常動作を確認した。また、この試験では、初めてのオンライントリガー選択によるデータ取得を実現した。さらに、磁場なし環境下でのデータ解析から、再構成したトラックに対する検出効率 $\sim 94\%$ (センサ片面) を得ることができた。トラックの質を考慮しなければならないが、この結果は E16 実験の要求性能を満たす。今後の性能評価の課題として、磁場あり環境下でのデータのさらなる解析、センサ両面を用いた 2 次元クラスタの検出効率および位置分解能の評価などが挙げられる。

　また、現在、2025 年春以降に予定されている E16 の物理データ取得運転に向けて、検出器の調整と準備を進めている。

Contents

Chapter 1

Introduction

1.1 Exploring nuclear matter via heavy-ion collision experiment

1.1.1 QCD phase diagram

The strong interaction described by Quantum Chromodynamics (QCD) governs the behavior of nuclear matter, exhibiting a rich variety of phases depending on temperature and baryon density. Figure 1.1 conceptually illustrates the QCD phase diagram, where the vertical axis represents temperature T and the horizontal axis represents baryon chemical potential μ_B. Cold nuclear matter, such as that found in ordinary nuclei, exists in the "hadronic phase", composed primarily of protons and neutrons. However, under extreme conditions of high temperature and/or high density, nuclear matter transitions can occur into interesting states characterized by the deconfinement of quarks and gluons, as described below.

At high temperatures and low baryon densities (upper-left region of the QCD phase diagram), the Quark-Gluon Plasma (QGP) emerges, where quarks and gluons are no longer confined within hadrons. It is believed that the universe existed in the QGP phase during the extremely early stages (approximately 10^{-6} to 10^{-5} seconds) after the Big-Bang. Understanding this state is crucial for exploring the early universe and the fundamental properties of QCD, and it has been well studied both experimentally and theoretically. A transition from QGP to a hadron phase occurs via a smooth "crossover" at $T \sim 160\,\mathrm{MeV}$ [1,2].

In contrast, at high baryon densities (the right region of the diagram), the phase structure is poorly understood. Various interesting states of matter are predicted in this region. One such state is "quarkyonic matter," where quark density dominates, yet the system exhibits hadronic-like properties near the Fermi-surface [3]. This state is important because such a high quark density is expected to influence particle production and transport properties through interactions between deconfined quarks and confined hadronic modes. In the context of a neutron star, quarkyonic matter is important for understanding compositions of its inner core and determining the equation of state (EOS), which governs properties such as mass-radius relationships and pressure-density correlations [4]. Another interesting prediction is "color superconductivity", where quarks, like electrons in ordinary superconductors, form Cooper pairs due to attractive interactions mediated by gluons. This state exhibits unique symmetry breaking and may lead to observable effects, such as changes in heat capacity and magnetic properties [5].

Additionally, the high-density region is also predicted to host a first-order phase transition between hadronic and quark matter phases, with a corresponding "QCD critical point" marking

the transition to a second-order phase. Identifying this critical point is one of the major goals of heavy-ion collision experiments [6,7]. However, theoretical calculations in this region are exceedingly challenging due to the "sign problem" in lattice QCD at finite μ_B, which prevents first-principles calculations from being directly applied [8, 9]. This limitation has made it difficult to accurately predict the properties of matter in this region, leaving many open questions about the nature of the phase transitions and an existence of intermediate phases such as quarkyonic matter.

This is why experiments are so important. Heavy-ion collision experiments at high baryon densities can help us explore nuclear. These experiments are crucial for revealing new aspects of the QCD phase diagram and for addressing problems that cannot be solved by theory alone.
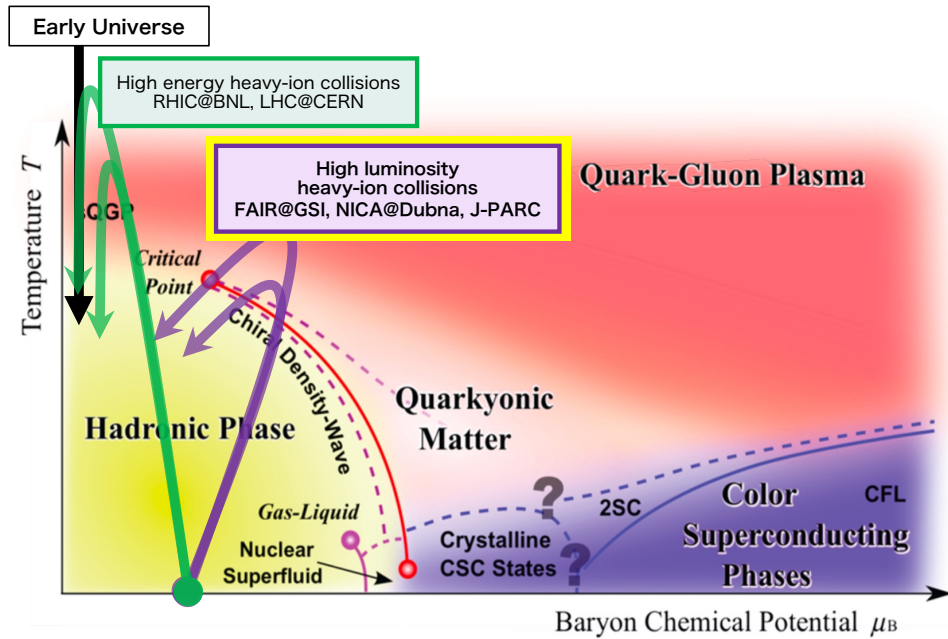
Figure 1.1: Sketch of the phase diagram for strongly-interacting matter [7].

1.1.2   Heavy-ion collision experiment

Such various states of nuclear matter are experimentally produced over a wide range of temperatures and densities by colliding nuclei at high energies. This section discusses the control of temperature and density through beam energy, past and future of heavy-ion collision experiments.

Control of temperature and density in heavy-ion collision experiment

One of the key features of high-energy heavy-ion collision experiments is the ability to control, to some extent, the temperature of the produced QGP and the quark number density by varying the collision energy $\sqrt{s_{NN}}$[1]. Figure 1.2 shows the rapidity ($y_{\mathrm{cm}} = 0$) distributions of the net proton

---

[1] $\sqrt{s_{NN}} = \sqrt{(E_1 + E_2)^2 - (\vec{p_1} + \vec{p_2})^2 c^2}$, where E_1, E_2 are the energies of the colliding nucleons, and $\vec{p_1}, \vec{p_2}$ are their momenta. Note that $\sqrt{s_{NN}}$ represents the center-of-mass energy per nucleon pair, not the total center-of-mass energy of the colliding nuclei.

number (number of protons minus number of antiprotons) in central nucleus-nucleus collisions (0-5% centrality) at various energies [10]. This distribution can be considered equivalent to the rapidity distribution of the net baryon number after nuclear collisions. Furthermore, it can be said to share the same shape as the rapidity distribution of the net quark number.
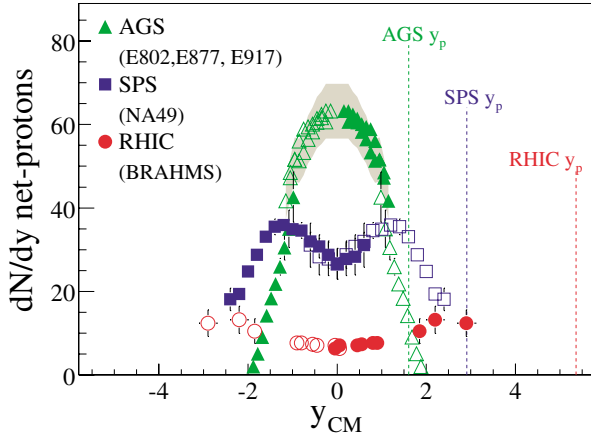
Figure 1.2: The rapidity distribution of net proton production from head-on heavy-ion collisions.   The three data sets represent collisions at different accelerators: Au+Au collisions at the AGS ($\sqrt{s_{NN}} = 5\,\mathrm{GeV}$), Pb+Pb collisions at the SPS ($\sqrt{s_{NN}} = 17\,\mathrm{GeV}$), and Au+Au collisions at RHIC ($\sqrt{s_{NN}} = 200\,\mathrm{GeV}$). For each data set, events with 0-5% centrality were selected [10].

Figure 1.3: Differences in Collisions Depending on $\sqrt{s_{NN}}$ [11].

The rapidity distribution at RHIC is characterized by a very flat shape and relatively low height. This is because, at extremely high energies reached by RHIC ($\sqrt{s_{NN}} \gtrsim 100,\mathrm{GeV}$), as shown in the top panel of Figure 1.3 quarks inside incident nuclei essentially pass through a collision point without stopping. At high energies, the nucleon-nucleon interaction (scattering cross-section) becomes smaller, resulting in insufficient stopping during a collision. Consequently, high-energy density generated near a collision point remains, which thermalizes to produce high-temperature matter. However, the net quark density around a collision point becomes small.

In contrast, the rapidity distribution at AGS exhibits a bell-shaped distribution centered around $y_{\mathrm{cm}} = 0$. This is because, at the energy range of AGS, as shown in the bottom panel of Fig. 1.3, colliding nuclei stop each other, concentrating all baryons around $y_{\mathrm{cm}} = 0$. This occurs because the nucleon-nucleon interaction becomes stronger while the initial kinetic energy of the nucleons is lower.

However, if $\sqrt{s_{NN}}$ is reduced excessively, incident particles may not interact, or even if they do, sufficient compression may not occur, resulting in no significant increase in density. Nevertheless, it is expected that up to approximately $\sqrt{s_{NN}} \simeq 4\,\mathrm{GeV}$, lowering the energy will lead to an increase in net quark density [11, 12].

The past and future of heavy-ion collision experiments

The study of QCD matter using high-energy heavy-ion collision experiments began in the 1980s. Since then, experiments have been conducted at accelerator facilities worldwide, with the highest priority placed on increasing the collision energy.

In 2000, heavy-ion collisions with $\sqrt{s_{NN}} = 200\,\mathrm{GeV}$ at the RHIC accelerator at Brookhaven National Laboratory (BNL) in the United States provided an evidence for creation of QGP [13, 14]. Since then with LHC at CERN, it has been established that nuclear matter in the high-temperature, low-density region can be generated. Currently, we are in a phase of conducting precise measurements of the properties of nuclear matter in this region and studying mechanisms of thermal equilibration. This corresponds to the green arrows in Fig. 1.1.
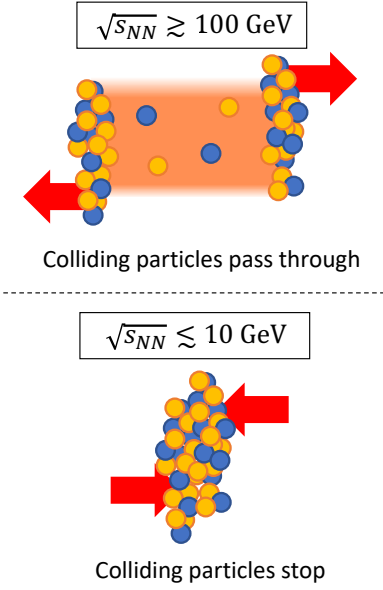
As collision energy increased, RHIC and LHC not only confirmed creation of QGP but also hinted at the possibility of its formation in smaller systems, such as proton-proton collisions, and at lower energy region. These phenomena are extremely rare and have only been discovered thanks to advances in the recent experimental technology. It is very likely that similar phenomena already occurred at AGS and SPS but remained undetectable due to the technological limitations at that time. Using modern advanced accelerators and detectors, exploring the energy range from a few GeV to several tens of GeV opens new possibilities. If highly statistical and precise measurements can be made in this energy range, it may be possible to study interesting phenomena such as first-order phase transitions and the phases that emerge in high-density regions. In other words, we should refocus on the low-energy region we once passed through and push forward into the new frontier of studying high-baryon-density regions.

Beam-Energy Scan (BES)

To explore this high baryon density region, experiments have been conducted to investigate the $\sqrt{s_{NN}}$ dependence in heavy-ion collisions. This study, aimed at probing the matter existing in various regions of the QCD phase diagram, is known as the "Beam-Energy Scan (BES)". This experiment is one of the key research topics in current high-energy heavy-ion collision studies. At present, RHIC, the central facility for this project, conducted the "RHIC-BES program" from around 2010 to 2015. This program investigated $\sqrt{s_{NN}}$ dependence in the $\sqrt{s_{NN}} = 7.7\text{-}20\,\mathrm{GeV}$ region by significantly lowering the collision energy of heavy-ion collisions. Subsequently, the second phase of the program, known as "RHIC-BES-II", was conducted from 2019 to 2021 [11].

The RHIC-BES program has suggested the possibility of the existence of a QCD critical point and signs of a phase transition in the high baryon density region. In particular, in the measurement of higher-order moments of "Net-proton fluctuations", non-monotonic behavior was observed around $\sqrt{s_{NN}} = 7.7$, which may indicate the existence of a QCD critical point [15]. In addition, in the measurement of collective flow, there are signs of softening of the equation of state (EoS) in the low-energy region, which is an important clue suggesting the existence of a first-order phase transition [15].

Similar experiments are being conducted at various locations around the world, in addition to RHIC. Figure 1.4 shows how the collision energy relates to the collision rate in these heavy-ion collision experiments. RHIC-BES-II, NA61/SHINE, STAR-FXT, and HADES are either currently operational or have completed their operations, while SIS100-CBM, NICA-MPD, and J-PARC-HI

are part of future plans. As shown in the figure, future experiments are expected to achieve collision rates that are two to four orders of magnitude higher than those of previous experiments. This advance is expected to allow measurements such as the signs observed in the RHIC-BES program to be made with higher statistics and precision, providing unprecedentedly detailed information. [16].

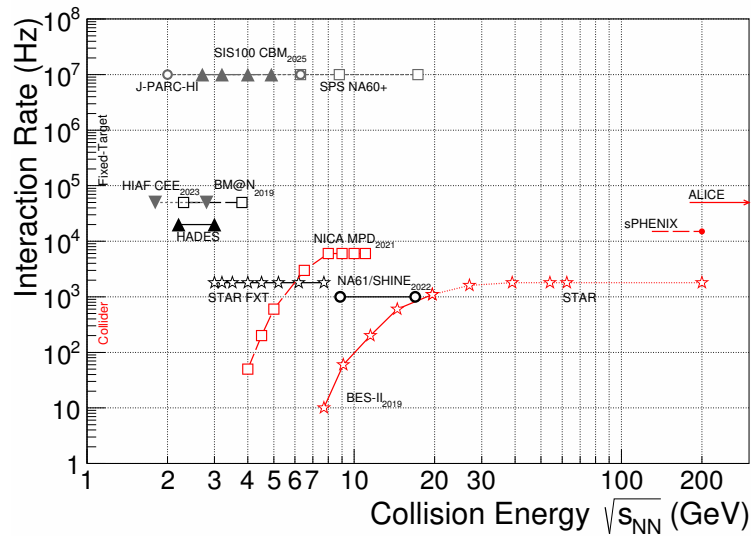Figure 1.4: Interaction rates achieved by existing and planned heavy-ion experiments are shown as a function of center-of-mass energy. Red symbols represent collider mode, while black and gray symbols indicate fixed-target mode. The solid curve corresponds to running facilities/experiments, the long-dashed line represents approved projects, and the short-dashed line indicates those in a conceptual design stage [16].

1.2 FAIR CBM experiment

The CBM experiment is a next-generation high-luminosity heavy-ion collision experiment that will be conducted at FAIR, which is currently under construction in Darmstadt, Germany [17]. The purpose of this experiment is to investigate the QCD phase diagram in the region of high net-baryon densities and moderate temperatures, using heavy-ion collisions. A key feature of the CBM experiment is its very high interaction rate, reaching up to 10 MHz in Au+Au collisions at maximum energy (45 AGeV). This interaction rate is approximately 10^4 times higher than that of the RHIC BES program. The experimental setup consists of a fixed-target forward spectrometer and primarily uses streaming data acquisition [18].

1.2.1 FAIR

The FAIR (Facility for Antiproton and Ion Research) in Darmstadt is planned as a platform for experiments across various fields, including nuclear physics, hadron physics, atomic physics, and plasma physics. The centerpiece of this facility is the heavy-ion synchrotron SIS100, installed in a tunnel with a total length of approximately 1100 m. The tunnel is designed to accommodate the SIS300 synchrotron in the future [17].

Figure 1.5 shows the existing facilities (blue) and planned future installations (red) of the FAIR. The existing GSI accelerators serve as the first stage of acceleration for the SIS100 and SIS300 synchrotrons.

The beams used in the CBM experiment are primary beams supplied by the SIS100/300 synchrotrons. At SIS100, the maximum energy of protons reaches 29 GeV, while that of Au ions reaches 11 AGeV (Table 1.1). Furthermore, the Slow Extraction from the synchrotron provides the beam at the CBM cave with a continuous structure. This ensures a uniform temporal distribution of beam particles, enabling an increase in the collision rate. The beam intensity can reach up to 10^9 ions/sec, and assuming a 1% interaction probability in the target, the interaction rate is expected to be 10 MHz [18,19].

Table 1.1: FAIR beam energy [17].

Synchrotron	Heavy-ion (Au) beam		Light nuclei beam		Proton beam	
	E_{beam}	$\sqrt{s_{NN}}$	E_{beam}	$\sqrt{s_{NN}}$	E_{beam}	$\sqrt{s_{NN}}$
SIS100	11 AGeV	4.7 GeV	0.5 - 14 AGeV	1.6 - 5.4 AGeV	29 GeV	7.5 GeV
SIS300 (tentative)	35 AGeV	8.2 GeV	0.5 - 45 AGeV	1.6 - 9.7 AGeV	90 GeV	13.1 GeV

1.2.2 The physics program of the CBM experiment

The purpose of the CBM experiment is to explore the QCD phase diagram in the region of high density and moderate temperature using high-energy nucleus-nucleus collisions. In this region, the experiment investigates the properties of nuclear matter at densities close to those in the cores of neutron stars, the possibility of a phase transition from hadronic matter to quark-gluon matter at the critical point of the QCD phase diagram, the existence of quarkyonic matter, and signs of chiral symmetry restoration.
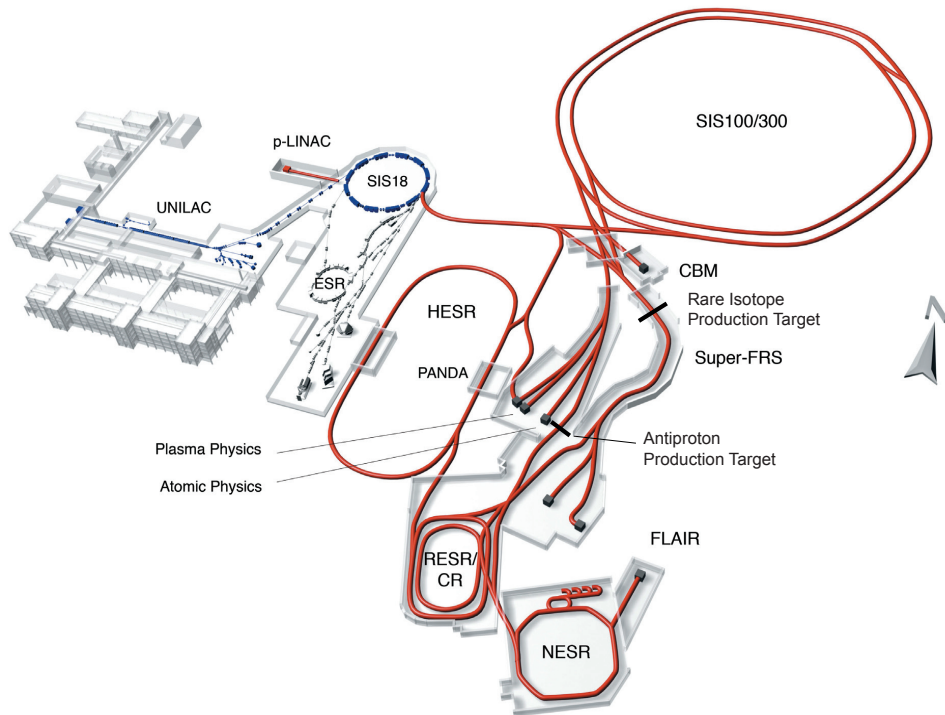
Figure 1.5: Layout of the Facility for Antiproton and Ion Research (FAIR) [17].

Among observables, the following key measurements will be carried out by CBM [15]:

- Differential collective flow of protons, pions, and deuterons to study the symmetric and asymmetric dense nuclear matter equation of state.

- Higher-order proton cumulants and cumulant ratios to search for the QCD critical point and study medium properties at high baryon densities.

- Hyperon correlations and (multi) hypernuclei to study hyperon-nucleon and hyperon-hyperon interactions, with impacts for the QCD phase diagram and our understanding of the inner structure of compact stars.

- Dilepton spectra and collective flow to characterize the medium temperature, study the chiral symmetry restoration and search for the first-order phase boundary in the high baryon density region.

- Global polarization and spin alignment at extreme baryon densities to study vorticity and spin transport.

For example, as shown in the previous section, the RHIC-BES program observed a non-monotonic behavior in the higher-order moments of net-proton fluctuations around $\sqrt{s_{NN}} = 7.7$ GeV. This behavior could be a possible indication of the existence of the QCD critical point. However, except for the fixed-target collision at $\sqrt{s_{NN}} = 3.0$ GeV, the RHIC-BES measurements have not provided sufficient rapidity coverage and statistical precision necessary for this analysis. To properly investigate this phenomenon, an experiment must be conducted with high statistics and rapidity coverage —this is precisely the role entrusted to the CBM experiment [15].

To conduct these studies, the CBM experiment will investigate collisions of heavy-ion and proton beams with fixed heavy-ion targets at the beam energies listed in Table 1.1. Heavy-ion collisions in this energy range are ideal for examining the properties of high-density nuclear matter. Figure 1.6 shows the energy density $\varepsilon(t)$ and the net baryon density $\rho(t)$ at the center of the fireball as a function of time for central Au+Au collisions at beam energies of 5 AGeV and 10 AGeV [20]. These behaviors are predicted by various transport models and hydrodynamic calculations. As suggested by these simulations, all models suggest that at a beam energy of 10 AGeV, densities up to eight times the saturation density ($\rho_0 \simeq 0.17\,\mathrm{fm}^{-3}$) can be achieved. Under such circumstances, nucleons overlap, and a transition to a mixed phase of baryons and quarks is expected. Furthermore, these simulations suggest that the fireball stays within the phase coexistence region (yellow region) for a relatively extended period at 5 AGeV and exits this phase at higher energies [19, 20].
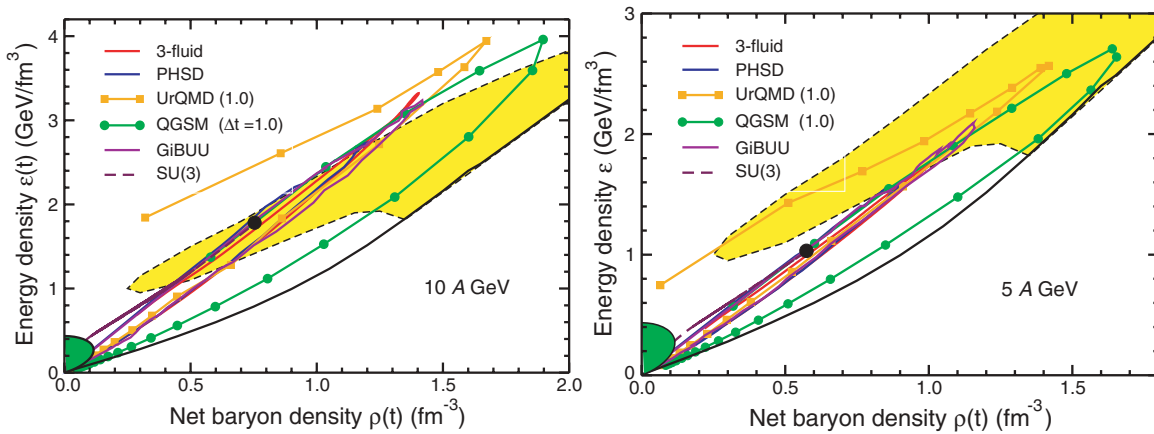
Figure 1.6: The phase trajectories ($\rho(t)$, $\varepsilon(t)$) at the center of a head-on Au+Au collision for various bombarding energies are shown as obtained using the indicated models, along with the schematic phase boundary. The yellow region represents the coexistence region, while areas below the black line ($\varepsilon(\rho, T = 0)$) are considered inaccessible. The symbols on the URQMD and QGSM curves are separated by the time intervals indicated in parentheses (fm/c) [20].

1.2.3   CBM spectrometer

The CBM experiment aims to measure almost all particles produced in nuclear collisions with high precision, focusing on quantities like yields, distributions, correlations, and fluctuations. To detect rare observables, particle tracks from each collision are reconstructed and analyzed in real time. This method introduces a new approach to data acquisition in high-energy physics, as CBM operates without a conventional trigger system [18].

The CBM experiment aims to begin operations in late 2028, and the setup of the detectors is currently underway. Figure 1.7 shows the setup of the CBM experiment. Immediately behind the target, a dipole magnet is positioned, housing the collision point detector (MVD) and the silicon strip detector (STS). These detectors are used for track reconstruction and momentum measurement. For lepton identification, either MUCH for muons or RICH for electrons is employed, with the choice depending on the operating mode. Additionally, a Transition Radiation Detector (TRD) for electron identification and a Time-of-Flight detector (TOF) for charged particle identification are installed. These detectors acceptance covers forward angles of up to 25 degrees [18].

STS
Silicon Tracking System*
MVD
Micro Vertex Detector*
* magnetic field

MuCh or RICH
MuonChamber System/
Ring Imaging Cherenkov
Detector

TRD
Transition Radiation
Detector

ToF
Time-of-Flight Detector

ECAL
Electromagnetic
Calorimeter
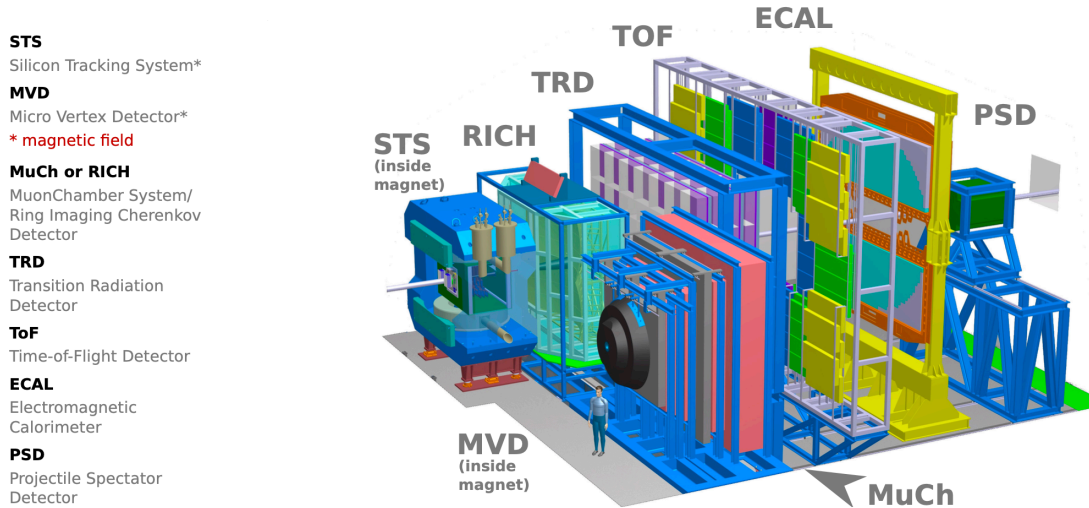
PSD
Projectile Spectator
Detector

Figure 1.7: The CBM experimental setup at FAIR [19].

1.2.4   Silicon Tracking System (STS)

The STS (Silicon Tracking System) is the main tracking detector of the CBM experiment. Installed in a $1\,\mathrm{T}$ dipole magnet, it reconstructs tracks of charged particles and measures their momenta. In particular, accurate track reconstruction in a high-rate interaction environment is critical. To achieve this, a detector with high time resolution, position resolution and detection efficiency is essential, and the STS fulfils these requirements.

Details of the STS are discribed in Chapter 2. This section outlines the design objectives of the STS and provides an overview of its collaboration with the J-PARC E16 experiment.

Design constraints and requrements

The detector performance requirements are summarised in Table 1.2. This section focuses on the unique characteristics of high-luminosity heavy-ion collision experiments, in particular strip occupancy and radiation resistance.

• **Maximum strip occupancies**   In the CBM experiment, at an interaction rate of up to $10\,\mathrm{MHz}$, the hit rate in the innermost region of the STS reaches up to $10\,\mathrm{MHz/cm^2}$, decreasing by two orders of magnitude in the outer regions. To account for this, the strip lengths are adjusted to keep the maximum strip occupancy[2] to a few percent.

• **Radiation-tolerance**   According to the simulations with FLUKA[3], the most exposed sensor position experiences $1\times10^{12\sim13}\,\mathrm{n_{eq}/cm^2}$/1 month. To withstand approximately 10 months of exposure, a radiation tolerance of up to $1\times10^{14}\,\mathrm{n_{eq}/cm^2}$ is required [18].

---

[2]Strip occupancy = Number of activated strips / Total number of strips
[3]A standard package for the calculation of non-ionising radiation. It provides the best physical description, especially for low energy neutrons.

Table 1.2: Design constraints and requirements for STS [18].

Parameter	Value
Aperture	$2.5° < \Theta < 25°$
Spatial resolution	$25\,\mu\mathrm{m}$
Maximum strip occupancies	a few%
Signal shaping time	20 nsec level
Single-hit efficiency	close to 100%
Track reconstruction efficiency	95%
Radiation-resistance (integrated fluence)	$1 \times 10^{14}\,\mathrm{n_{eq}}\,/\mathrm{cm}^2$
Momentum resolution	$\Delta p/p \approx 1\%$

Collaboration with the J-PARC E16 experiment

The STS is currently being tested using beams of SIS18, an existing synchrotron at GSI in the mCBM program (FAIR Phase-0) [21]. However, testing under actual experimental conditions, such as in a magnetic field and with high-intensity beams, remains insufficient. To address this, the STS sensors are installed as the innermost tracking detector of the J-PARC E16 experiment, where it undergoes performance evaluation and operational testing using high-intensity beams (1×10^{10} proton per 2-sec spill) in a magnetic field (1.77 T). The interaction rate in the J-PARC E16 experiment reaches 10 MHz, which is equivalent to CBM. The J-PARC E16 experiment is an excellent experiment for testing the operation of STS.

The introduction of the STS into the E16 experiment also provides benefits for the experiment itself. The E16 experiment aims to verify the partial restoration of spontaneously broken chiral symmetry through electron-positron pair measurements using high-intensity proton beams (Chapter 3). To measure this restoration phenomenon, precise tracking of electrons (positron) is essential. The primary tracking detector in the E16 experiment, the GEM tracker (GTR), has a relatively large time resolution of 300 nsec, which leads to a high fake track rate under high-rate intaraction. Therefore, a tracking detector with a high time resolution on the order of a few nsec is required. To meet this requirement, the introduction of the STS has been considered, and it is expected to contribute to improving the accuracy of track reconstruction in the E16 experiment.
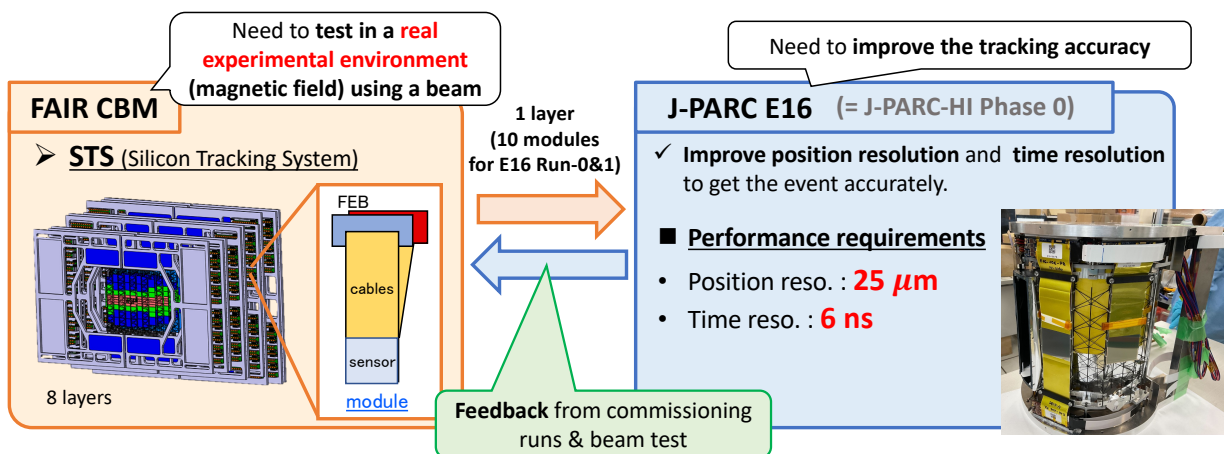

Figure 1.8: Collaboration between the CBM experiment and the J-PARC E16 experiment: STS

Additionally, it is important to note that the E16 experiment represents the initial stage of the J-PARC-HI program, corresponding to Phase 0. The J-PARC-HI project is currently being led by H. Sako, and in the future, there are plans to convert the E16 beamline (high-p beamline, Section 3.4.2) to heavy ion acceleration [22]. The collaboration between these two programs, which have similar goals, is crucial for leading progress in this field. The collaboration between the CBM and the J-PARC E16 is also important in this context.

1.3   Purpose of my study and thesis outline

The purpose of my study is to develop and evaluate the main tracking detector (STS) for the next-generation high-luminosity heavy-ion collision experiment (CBM). Therefore, the STS sensors were installed in the J-PARC E16 experiment and performance evaluation and operation tests were carried out. As mentioned above, this also has advantages for the J-PARC E16 experiment.

The STS was first installed and started operating in the J-PARC E16 experiment commissioning run (Run-0d) in 2023. During this commissioning run, we were unable to obtain much performance evaluation data due to some reasons such as insufficient preparation and a shortened beam time due to a fire. Therefore, in November 2023, we carried out a performance evaluation using an electron beam. Here, we tested the E16 STS DAQ system and evaluated its fundamental sensor performance, including time resolution and detection efficiency. In the fifth commissioning run (Run-0e) of the J-PARC E16 experiment, which was carried out in May 2024, we collected data and evaluated the performance, including operation verification under the actual experimental conditions, such as in a magnetic field and under high-rate conditions. This thesis reports on the results of the STS peformance evaluation through these two tests.

This thesis is made up of seven chapters, and Chapter 1 begins with the QCD phase diagram, and briefly summarises the future mission of heavy ion collision experiments and the CBM experiment. The remaining chapters are organised as follows:

- Chapter 2 explains the CBM STS. Starting with the detection principle of silicon strip detector, it explains the basic performance of sensors, readout chips, and the layout of the CBM STS.

- Chapter 3 explains the J-PARC E16 experiment, the experimental stage. The physics of the E16 experiment, the beamline, and the spectrometer.

- Chapter 4 explains the installation of the STS for the J-PARC E16 experiment. It details the requirements for the STS in the context of E16, the structure of the E16 STS Chamber, and the E16 STS readout chain.

- Chapter 5 reports on the test experiment conducted using the electron beam at KEK. This chapter primarily focuses on the evaluation of time resolution and detection efficiency of the STS sensor.

- Chapter 6 reports on the operational results of the STS during Run-0e of the J-PARC E16 experiment. This chapter discusses the performance of the STS under actual experimental conditions and its operational stability in a magnetic field.

- Chapter 7 reports summary and outlook.

Chapter 2

Silicon Tracking System (STS)

The Silicon Tracking System (STS) is the primary tracking detector in the CBM experiment. The STS was designed based on the constraints outlined in Table 1.2. First, the principles of silicon detectors are described, followed by an explanation of the CBM STS module, including its sensors and front-end boards. Finally, the layout of the CBM STS is discussed.

2.1   Principles of silicon detectors

2.1.1   P/N-type semiconductors

Silicon forms a crystal with a regular structure, and the energy states occupied by electrons within the crystal are distributed in nearly continuous ranges called energy bands. In this energy band structure, there is a "valence band", which is typically filled with electrons, and a "conduction band", which is at a higher energy level and can conduct electricity when electrons are present. The region between the valence band and the conduction band, where no electron states exist, is called the forbidden band or bandgap. The bandgap of silicon is approximately $1.12\,\mathrm{eV}$ at room temperature. This energy gap is significantly larger than the thermal energy ($k_B T = 0.025\,\mathrm{eV}$) of an electron at room temperature, meaning that only a small fraction of electrons can thermally excite into the conduction band, leaving silicon with low electrical conductivity under normal conditions [23].
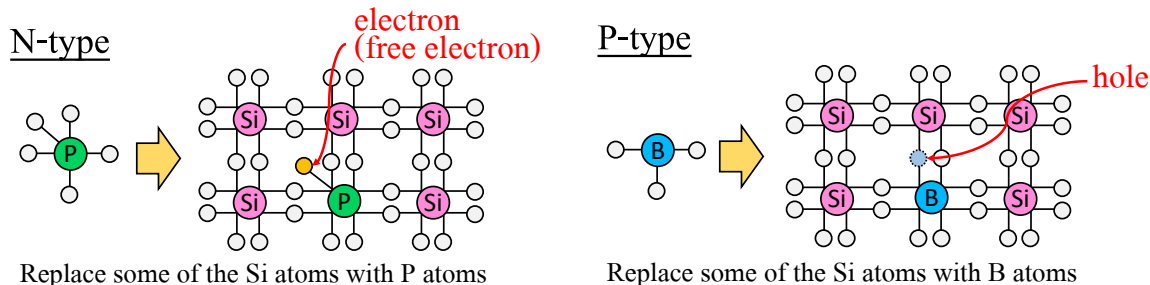

Figure 2.1: p/n-type silicon semiconductors.

The electrical properties of silicon are determined by impurities within the crystal. For example, when impurities with five valence electrons, such as phosphorus (P), arsenic (As), or antimony (Sb),

15

are added to silicon, which has four valence electrons, one extra electron is left after bonding with silicon atoms. This electron can easily move to the conduction band, allowing it to contribute to charge transport in silicon. A semiconductor that has loosely bound electrons due to such impurities is called an "n-type" semiconductor (Figure 2.1 left). The charge carriers responsible for charge transport in a silicon crystal are collectively referred to as "carriers". Conversely, when impurities with three valence electrons, such as boron (B), aluminum (Al), or gallium (Ga), are added to silicon, holes act as carriers and help in charge movement, turning the semiconductor into a "p-type" semiconductor (Figure 2.1 right). Additionally, n-type and p-type semiconductors with very high levels of impurities are called n^+ and p^+ semiconductors, respectively, while n-type semiconductors with low levels of impurities are called n^-.

2.1.2 P-N junction and depletion layer

N-type and p-type semiconductors are typically used in combination. At the junction between p-type and n-type semiconductors, electrons diffuse from the electron-rich n-type semiconductor to the p-type semiconductor, while holes diffuse from the hole-rich p-type semiconductor to the n-type semiconductor. In this process, electrons and holes neutralize each other near the interface. This creates a region at the p-n junction interface that is devoid of carriers, known as the "depletion layer". In the p-type region of the depletion layer, negatively charged acceptor ions that have received electrons are present, while in the n-type region, positively charged donor ions that have received holes are present. Due to the electrostatic attraction between these donor and acceptor ions, an internal electric field is generated within the depletion layer.

As the depletion layer begins to form, free electrons in the n-type semiconductor are blocked and pushed back by the internal electric field, preventing further diffusion. Similarly, holes in the p-type semiconductor are also blocked and repelled by the internal electric field. In this way, the diffusion of majority carriers stops, and equilibrium is established [23].
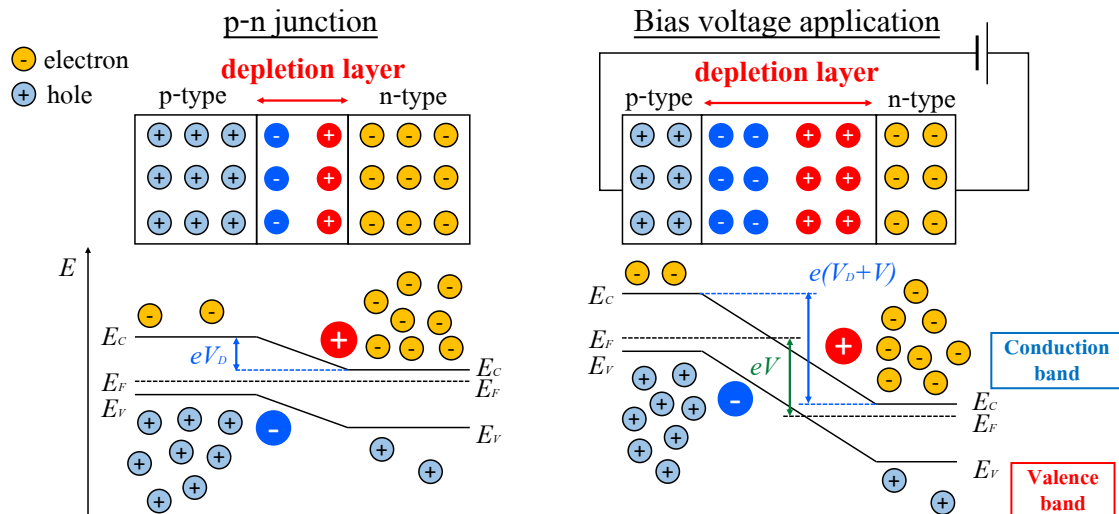

Figure 2.2: pn-junction and energy band structure.

Additionally, in terms of the energy band structure, when a p-n junction is formed, the Fermi levels align, causing the energy bands to bend in the depletion layer region, creating a step. This

step, represented by the voltage V_D, is called the diffusion potential. For example, in the case of a p-n junction formed with silicon, the diffusion potential is approximately 0.6 to 0.7 V (Fig. 2.2 left).

The depletion layer is usually small, so applying a positive voltage to the n-type semiconductor and a negative voltage to the p-type semiconductor can widen the depletion layer (Fig. 2.2 right). This voltage orientation is called "reverse bias". The thickness of the depletion layer increases with the magnitude of the reverse bias, but when a large reverse bias is applied, the current suddenly flows in the reverse direction at a certain voltage. This phenomenon is called "breakdown".

2.1.3   Detection principles of silicon detectors

There are two detection methods for silicon detectors used for high-energy particles: the scintillator type, which detects particles indirectly by causing a scintillator to emit light, and the direct type, which detects high-energy particles directly. In general, direct-type detectors are used for tracking detection.

When a charged particle enters a direct-type silicon detector, it loses energy along a straight path, which depends on the type and energy of the particle. This interaction between the charged particle and electrons in the silicon generates electron-hole pairs. By layering silicon detectors and recording the points where the charged particle passes as electrical signals, its track can be reconstructed. Additionally, the number of electron-hole pairs created depends only on the energy loss of the particle, not on the particle type (at 300 K, one electron-hole pair is generated for every 3.62 eV of energy lost). This means that by measuring the amount of charge, we can estimate the particle's energy loss [23].

The common types of silicon tracking detectors are strip-type and pixel-type detectors. Strip-type detectors are further classified into single-sided silicon strip detectors (SSSD) and double-sided silicon strip detectors (DSSD). Since the CBM STS sensor is a DSSD, the following section will provide an explanation of this type.

Double-sided Silicon Strip Detector (DSSD)

Figure 2.3 is a conceptual diagram of the DSSD. Structurally, p+ type semiconductor strips are placed on one side of an n-type semiconductor plate (n-type semiconductor bulk), while n+ type semiconductor strips are arranged on the opposite side. Additionally, aluminum electrodes for current readout are connected to the strips (Fig. 2.3 shows the AC readout type). Compared to the DC readout type, the AC readout type has the advantage that dark current from each strip does not flow into the signal line. The CBM STS sensor also uses this AC readout configuration.

When a charged particle enters the depletion layer expanded by the bias voltage, it loses energy within the silicon depletion layer. This energy loss generates a number of electron-hole pairs in the depletion layer, proportional to the energy deposited by the charged particle. The resulting electrons and holes are collected by the n^+ and p^+ strips, respectively, due to the reverse bias voltage. These collected electrons and holes are then read out as an electrical current through aluminum strips, allowing the detection of the particle's track.

In this process, the n^+ strips are inherently electrically connected to the n-type semiconductor bulk, causing electrons generated in the depletion layer to be detected equally by all n+ strips. To prevent this, double-sided silicon strip detectors insert p-stop regions, which are p^+ type strips, between the n^+ strips. The p-stop regions create depletion layers between themselves and the n-type semiconductor bulk. As a result, the depletion layers formed by the p^+ strips and the p-stops

17

merge, electrically isolating each n+ strip from one another.

In an orthogonal-type DSSD, where the p-side and n-side strips are arranged perpendicular to each other, high position resolution can be achieved in both directions. However, to align the readout directions geometrically, the readout electrodes on one side must be positioned in a different direction from the strips (DML: Double MetalLayer). The DML often increases the total capacitance of the strips, which can affect signal quality and overall detector performance. Therefore, the CBM STS sensor is a non-orthogonal type DSSD, with the p-side strips slightly angled (Fig. 2.3 right)[1]. This angle is called the "stereo angle" [24].
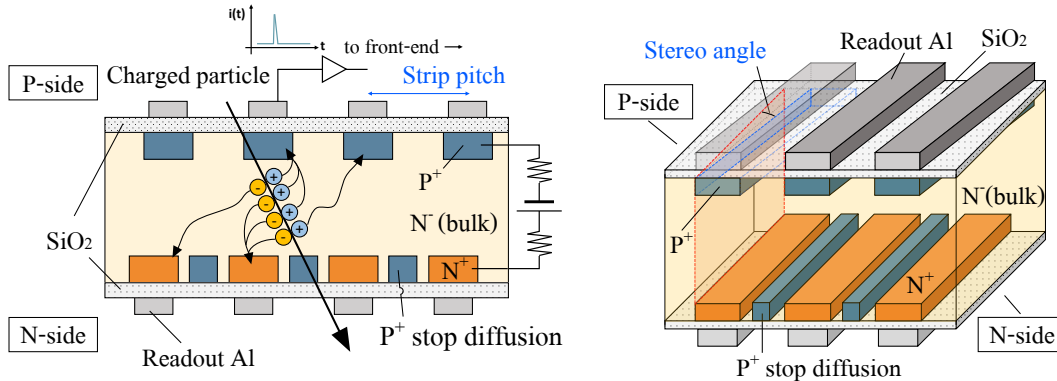

Figure 2.3: Structure of DSSD (left) and explanation of stereo angle (right).

2.2   STS module

The basic building block of the STS is the detector module. It includes a double-sided silicon sensor connected to two front-end boards (FEB-8) via thin microcables. Each side of the sensor has 1024 strips, linked to an FEB-8 that holds 8 custom-designed ASICs (STS-MUCH XYTER). Groups of 128 strips are connected to pairs of microcables, that carry analog signals to the FEB-8.

Modules with different form factors (sensor sizes and microcable lengths) will be produced based on their position in the final detector. Figure 2.4 shows a prototype of the detector module. The main components are described in the following sections.
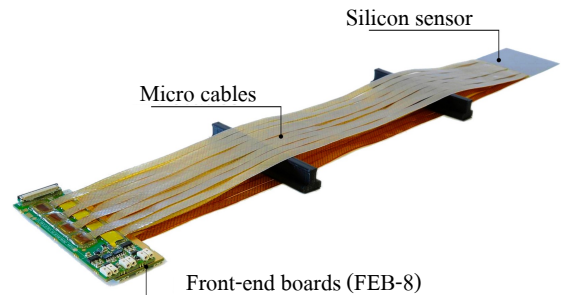

Figure 2.4: The STS module: This is the functional building block of the STS [19].

2.2.1   Silicon sensor

The CBM STS sensor is a non-orthogonal type DSSD sensor manufactured by Hamamatsu Photonics. On both sides of an n-type wafer with a thickness of $320\,\mu m$, 1024 n-type (or p-type) strips are arranged with a pitch of $58\,\mu m$. The strips on the p-side are tilted by 7.5 degrees relative to the n-side strips. This design minimizes the number of ghost hits while providing sufficient

---

[1]However, The short strips at the edge of the p-side are interconnected using a second metallization layer (DML) on the sensor (Appendix A.1).

resolution along the direction of the strips. The basic specifications are shown in Table 2.1. The sensors are designed with four different strip lengths and are planned to be arranged to maintain a maximum strip occupancy of a few percent, in accordance with the particle density in the STS detector region (Figure 2.5) [18].

Table 2.1: Basic specifications of the CBM STS sensor.

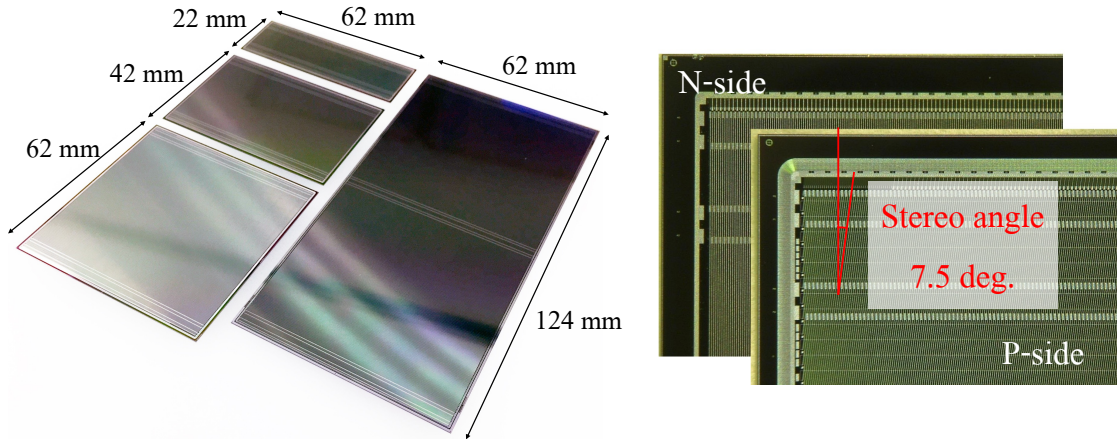| Parameter	Value
Size	$62 \times 22/42/62/124 \, \text{mm}^2$
Sensitive area	$60 \times 20/40/60/120 \, \text{mm}^2$
Thickness	$320 \, \text{µm} \; (0.37\% \, \text{X}_0)$
Strip pitch	$58 \, \text{µm}$
Stereo angle	7.5deg.
Number of Strips	1024
Position resolution	(x) $15 \, \text{µm}$, (y) $110 \, \text{µm}$
Time resolution	$\sim 6 \, \text{nsec}$

Figure 2.5: The CBM06 silicon sensors family for the tracking system. Sensors will be produced with the same width of 62 mm and four different strip lengths (22 mm, 42 mm, 62 mm and 124 mm), matching the track densities in the STS detector [19].

2.2.2   Micro-cable

Low-mass micro cables are used to transfer signals from the sensors to the FEB-8. They are covered with a shielding layer in order to reduce the electromagnetic interference and noise level. For the signal transmission, two layers of microcable with aluminum strips and 116 µm pitch are used (The sensor strips are divided into two layers of cables, one for even-numbered strips and one for odd-numbered strips.). They are separated with a meshed spacer in order to reduce the parasitic inter-layer capacitance, see Figure 2.6. The supporting material for the aluminum strips is 20 µm polyimide [19].
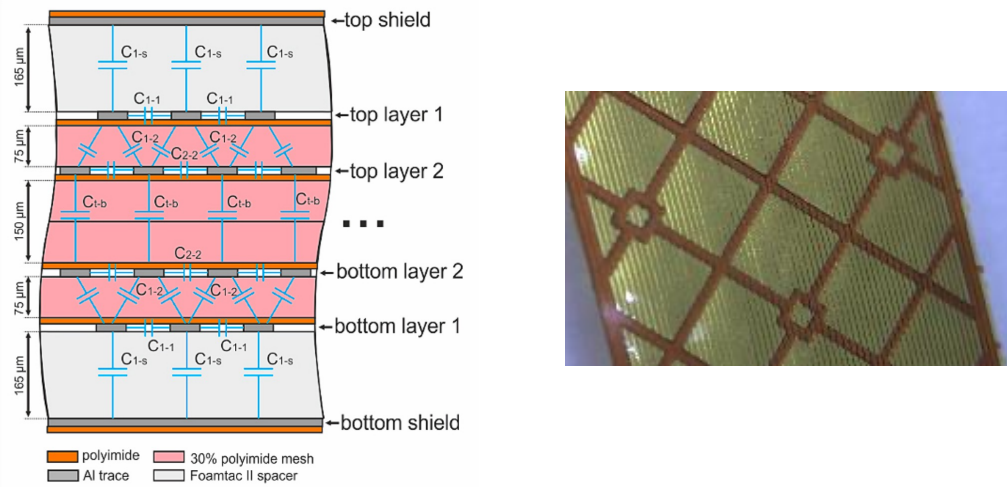
Figure 2.6: Cross section of a stack of readout microcables [19] (left) and photo of microcables (right). The diagram illustrates the effective capacitances between the different cable layers.

2.2.3   FEB-8

The FEB-8 (Front End Board) is a readout board equipped with eight STS-XYTER (SMX) ASICs. Each ASIC is capable of reading out 128 channels, allowing a single FEB-8 to read out 1024 channels (one side of the sensor). There are two types of FEB-8 with geometrically symmetric signal arrangements, and different types are used for the two sides of the sensor. The SMXs on the FEB-8 are connected to the silicon body via micro-cables. Below is a description of the ASIC, the SMX.

STS-MUCH XYTERv2

The STS-MUCH XYTERv2 (STS-MUXH X, Y, Coordinate, Time, and Energy Read out, (SMX)) is a self-triggered, continuous readout ASIC developed for the silicon strip detectors and GEM detectors in the CBM experiment. The specifications of the SMX are shown in Table 2.2 [25].
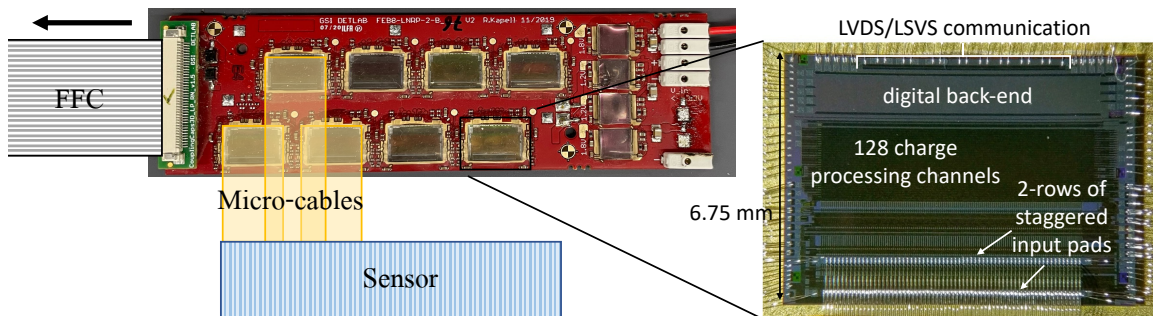

Figure 2.7: FEB-8 (left) and STS-MUCH XYTERv2 (right) [25].

Table 2.2: Basic specifications of STS-XYTER [25].

Parameter	Value
Number of channels	$128 + 2\,\mathrm{ch}$
Input capacitance (detector + cable)	$30\,\mathrm{pF}$
ENC (Equivalent Noise Charge) @30 pF	$900\,\mathrm{e^-}$
ADC bit	5-bit
TDC bit	14-bit

A simplified circuit diagram of the SMX is shown in Figure 2.8. The charge signals generated by the detector are processed by a Charge Sensitive Amplifier (CSA), which integrates the signals. The output from the CSA is then sent to the Polarity Selection Circuit (PSC), which adjusts the signal polarity. This component is essential for reading out the SSD, where charge signals with different polarities are input from both sides. The output signal from the PSC is divided into two paths, where signal shaping is performed by the fast SHAPER (shaping time: 30 nsec) and the slow SHAPER (shaping time: 90, 160, 220, 280 nsec, used at 90 nsec in the J-PARC E16 experiment). In the discriminator logic (DISCR LOGIC, 320 MHz, 14-bit), a timestamp is recorded, while in the ADC logic (flash ADC, 5-bit), the peak value of the waveform corresponding to the incident charge is recorded. By dividing the signal into these two paths, it is possible to record both time and charge with high resolution. Additionally, by changing the capacitance value of the CSA, the system can switch between the STS mode (ADC range: 0-14 fC) and the MUCH mode (ADC range: 0-90 fC). For STS readout, the STS mode is used [25].
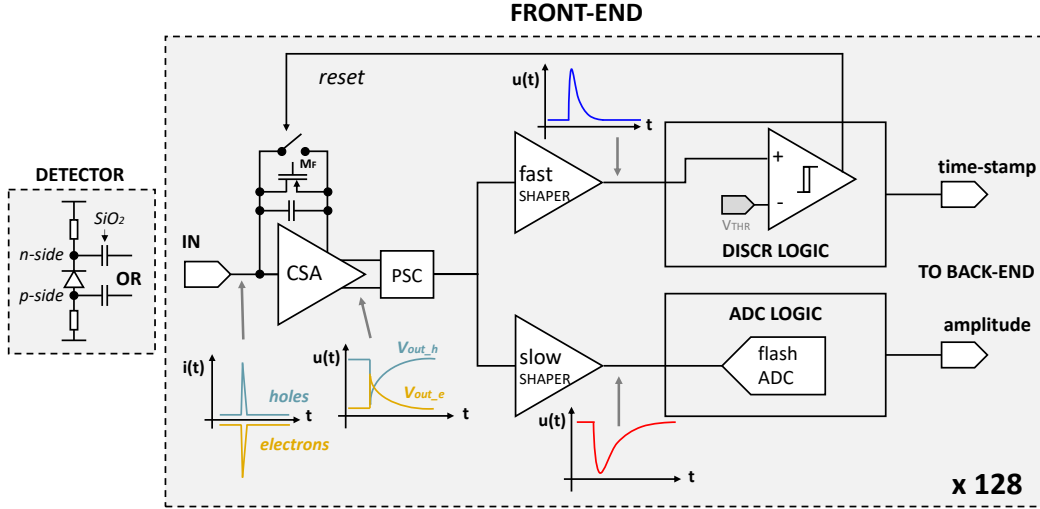

Figure 2.8: SMX circuite [25].

Hit generation mechanism

In self-trigger mode, hit information is generated according to the following procedure (Figure 2.9 and Figure 2.10). First, each time the signal from the fast SHAPER exceeds the threshold of the discriminator, the value of the timestamp is stored in the latch. When the signal from the slow SHAPER exceeds the lowest threshold of the 5-bit ADC discriminator, the storage of the timestamp

into the latch is blocked by the block_ts signal. When the signal from the slow SHAPER reaches its peak and returns to the lowest threshold of the ADC discriminator, the data valid flag is asserted, and the hit data is written to the FIFO. Subsequently, the state of the channel is reset by the reset signal. If a new hit occurs during this process, the event missed flag is added to the hit information [25].
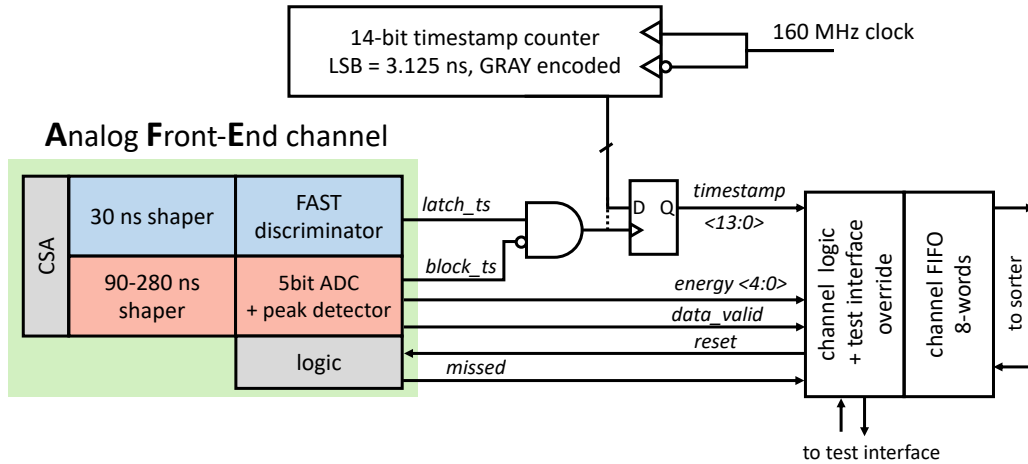

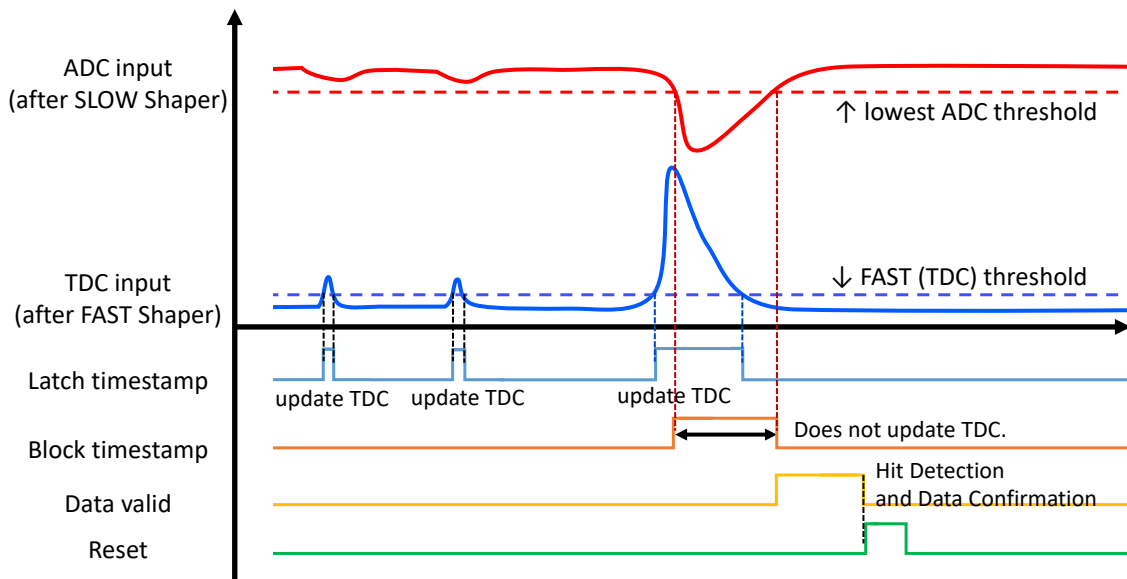Figure 2.9: Hit generation mechanism [19, 25].

Figure 2.10: Timing scheme of the hit generation [25].

To correctly acquire hit data, it is essential to set appropriate thresholds, particularly ensuring that the timing discriminator threshold (FAST threshold) is set sufficiently lower than the lowest ADC (adc = ch1) threshold. This ensures that the timestamp value is latched each time the initial

ADC discriminator is triggered. If the FAST threshold is set higher than the lowest ADC threshold, as shown in Figure 2.11, hits that exceed the lowest ADC threshold but do not exceed the FAST threshold will have the timing of the previous hit recorded. Refer to Appendix C.2 for the proper method of threshold adjustment [25].
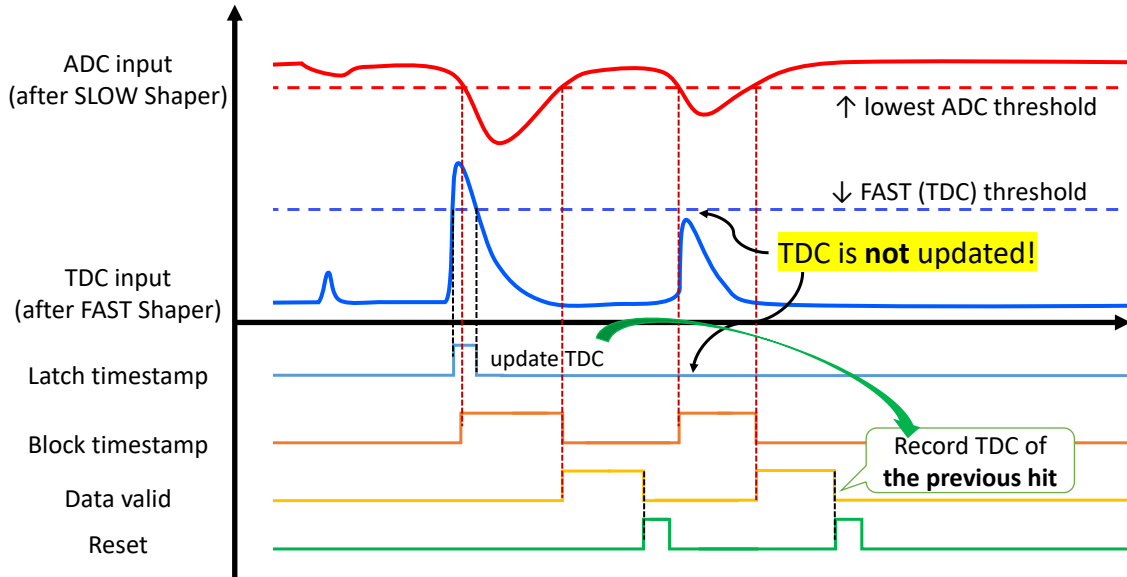

Figure 2.11: Timing scheme of the hit generation when the FAST threshold is higher than the lowest ADC threshold.

2.3   CBM STS layout

The smallest unit of the STS is a module, as described in the previous section. These modules are grouped into sectors for readout purposes. The sectors are mounted onto a carbon fiber support structure, forming a ladder that is mechanically and electrically integrated into a tracking station. The readout direction of each module is oriented toward its respective end. Multiple ladders are then aligned side by side to form a single plane, referred to as a station (Figure 2.12).

The STS comprises eight stacked stations, covering an acceptance range of $2.5° < \Theta < 25°$. Station 1 is positioned 30 cm downstream of the target, with subsequent stations spaced 1 cm apart (Figure,2.13). The setup includes 106 detector ladders, 896 modules, and 14,336 STS-XYTER ASICs, housed within a $2\,m^3$, $1\,T$ dipole magnet [26]. This design facilitates the reconstruction of tracks and momentum determination for a variety of charged particles from beam-target interactions [18].
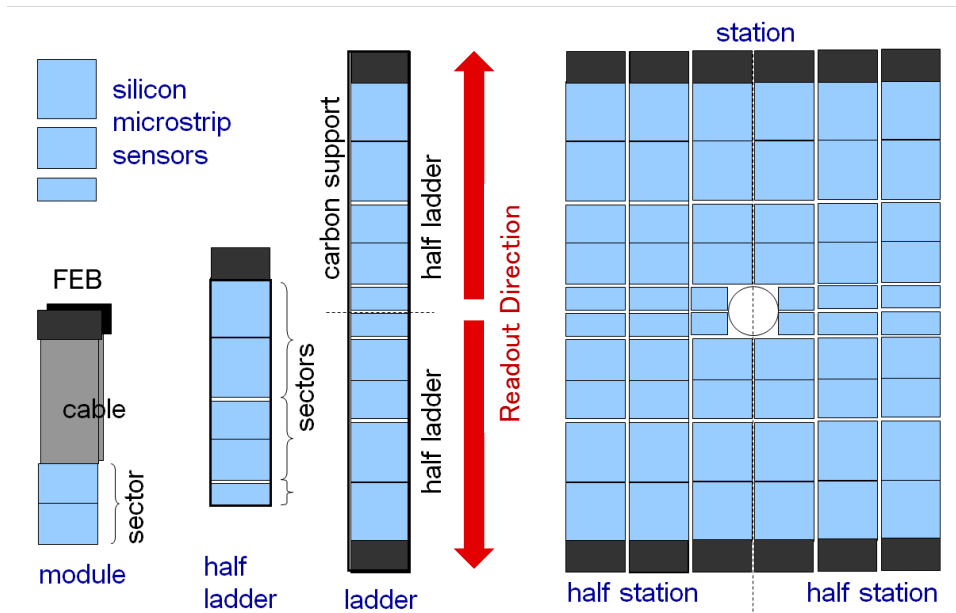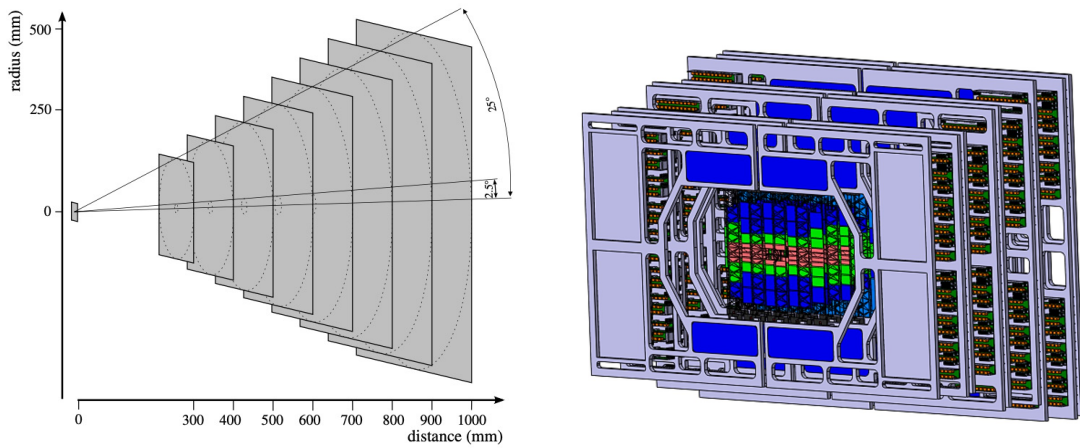
Figure 2.12: Conceptional layout of the tracking stations and their building blocks [18].

(a) Concept of STS tracking stations covering the polar angles 2.5 deg. $< \Theta < 25$ deg.

(b) Eight tracking stations for the STS detector

Figure 2.13: CBM STS layout [18, 19].

Chapter 3

J-PARC E16 experiment

The J-PARC E16 experiment aims to experimentally investigate the partial restoration of chiral symmetry in dense matter by studying changes in the properties of vector mesons. In this experiment, we aim to observe changes in the in-medium spectral functions of vector mesons as a possible signature of chiral symmetry restoration. Specifically, we measure the $\beta\gamma$ dependence of the mass distribution of vector mesons through their decays into electron pairs ($\rho, \omega, \phi \to e^+e^-$), as electron pairs are minimally affected by final-state interactions. These measurements are carried out in proton-nucleus (p+A) collisions at a proton beam energy of $30\,\mathrm{GeV}$.

This section provides an overview of the J-PARC E16 experiment. First, the physics background and previous studies are introduced. Next, the objectives and current status of the E16 experiment are explained. Finally, a brief description of the beamline and each detector is provided.

3.1 Physics background

Chiral symmetry in quantum chromodynamics (QCD) is a fundamental symmetry that exists in the idealized scenario where quark masses are zero and is an intrinsic property of the QCD Lagrangian. This symmetry permits left-handed and right-handed quarks to transform independently. However, in the actual vacuum state, this symmetry is spontaneously broken.

The quark condensate $\langle\bar{q}q\rangle$ is the order parameter of chiral symmetry, serving as an indicator of chiral symmetry breaking and playing a crucial role in the dynamical generation of quark masses. Light quarks, such as u and d quarks with bare masses of only a few MeV, acquire significant dynamical masses through interactions with the QCD vacuum. This process can be expressed as:

$$M_q = m_q + \Sigma_q, \tag{3.1}$$

where m_q is the bare quark mass, and Σ_q represents the vacuum interaction contribution, closely linked to $\langle\bar{q}q\rangle$. Σ_q reflects quantum fluctuations and the non-trivial QCD vacuum structure, leading to dynamical masses around 300 MeV for light quarks. Consequently, most hadron masses arise not from bare quark masses but from spontaneous chiral symmetry breaking [27].

Furthermore, the spontaneous breaking of chiral symmetry, as described by the Nambu-Goldstone (NG) theorem, leads to the emergence of massless pseudoscalar particles. In QCD, these particles manifest as pions. The nonzero mass of physical pions arises from contributions due to finite quark

masses, which explicitly break chiral symmetry. This relationship is quantitatively expressed by the Gell-Mann-Oakes-Renner (GOR) relation [28]:

$$m_\pi^2 f_\pi^2 = -\frac{1}{2}(m_u + m_d)\langle \bar{u}u + \bar{d}d \rangle, \tag{3.2}$$

Here, m_π represents the pion mass, f_π denotes the pion decay constant, and m_u and m_d are the bare masses of the u and d quarks. This equation demonstrates how the pion mass is determined by the breaking of chiral symmetry.

Chiral symmetry breaking is expected to be partially restored under finite temperature and finite density conditions, and these dependencies have been quantitatively investigated using the Nambu-Jona-Lasinio (NJL) model [27,29]. The quark condensate $\langle \bar{q}q \rangle$, as shown in Fig. 3.1, depends on temperature T and density ρ and exhibits the following characteristics:

- **Phase transition-like behavior at finite temperature**: The quark condensate decreases sharply near the critical temperature T_c, indicating phase transition-like behavior.

- **Linear decrease at finite density**: At finite density ρ, the condensate exhibits an approximately linear dependence.
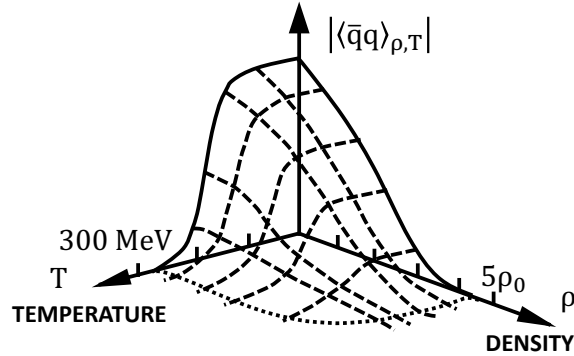

Figure 3.1: The condensate $\langle \bar{q}q \rangle$ as a function of density ρ and temperature T. The density is given in units of nuclear matter density $\rho_0 = 0.17\,\text{fm}^{-3}$ [28].

The spontaneous breaking of chiral symmetry is a fundamental concept for understanding the properties of the QCD vacuum. Experimentally observing the partial restoration of chiral symmetry under finite temperature and density conditions remains a significant challenge. Understanding this phenomenon is essential for gaining deeper insights into the mechanism of hadron mass generation and the fundamental nature of QCD.

3.2   Previous study

To investigate the partial restoration of spontaneously broken chiral symmetry, it is essential to quantitatively evaluate the quark condensate under high-temperature or high-density conditions. However, the quark condensate $\langle \bar{q}q \rangle$ is not directly observable, making direct measurement impossible. As a result, efforts have focused on measuring the masses of hadrons, which are influenced by the quark condensate, by analyzing their mass spectra in various media. Among these, vector mesons have been extensively used as probes to study the effects in finite-density media. Vector mesons are particularly important for exploring the QCD vacuum because their masses primarily arise from the quark masses due to minimal interaction terms and because they decay into lepton pairs, which are unaffected by strong interactions. Therefore, they serve as critical probes for investigating the QCD vacuum.

3.2.1   QCD sum rules

Theoretically, the masses of vector mesons are predicted to decrease inside nuclear matter. Figure 3.2 presents the theoretical predictions for the mass changes of vector mesons in a finite-density environment based on the QCD sum rules, as proposed by T. Hatsuda and S. H. Lee [30]. In this figure, the horizontal axis represents the density ρ, normalized by the nuclear saturation density ρ_0. According to these theoretical predictions, at nuclear saturation density ρ_0, the masses of ρ and ω mesons are expected to decrease by approximately $120 \sim 180\,\mathrm{MeV}/c^2$, while the mass of the ϕ meson is predicted to decrease by about $20 \sim 40\,\mathrm{MeV}/c^2$.
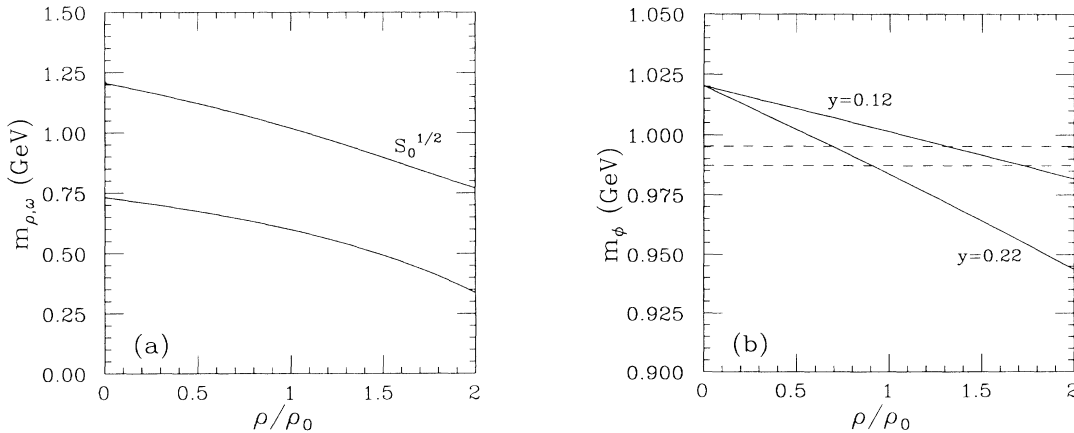

Figure 3.2: Density dependence of the mass of vector mesons calculated using QCD sum rules [30]. Panel (a) shows ρ and ω mesons, while panel (b) illustrates ϕ mesons. $\sqrt{S_0}$ represents the threshold where the calculation method is applicable. The parameter y denotes the strangeness content in nucleons, assumed in the paper to be within the range $0.12 < y < 0.22$.

P. Gubler and K. Ohtani combined the QCD Sum Rules with the Maximum Entropy Method (MEM) to derive the relationship between the masses of mesons in nuclear matter and the strangeness quark condensate in nucleons [31]. The strangeness quark condensate in nuclear matter is related

to the expectation value of the strangeness quark condensate in a single nucleon as follows:

$$\langle \bar{s}s \rangle_\rho = \langle \bar{s}s \rangle_0 + \langle N | \bar{s}s | N \rangle \rho, \tag{3.3}$$

The relationship between the strange sigma term, expressed using $\langle \bar{s}s \rangle_\rho$ as:

$$\sigma_{sN} = m_s \langle N | \bar{s}s | N \rangle, \tag{3.4}$$

and the peak value of the ϕ meson mass spectrum at nuclear densities is plotted in Fig. 3.3. From this figure, it can be seen that the mass shift of the ϕ meson and σ_{sN} have a proportional relationship, which can be expressed as follows:

$$\frac{m_\phi(\rho)}{m_\phi(0)} - 1 = \left[b_0 - b_1 \left(\frac{\sigma_{sN}}{1\,\text{MeV}} \right) \right] \frac{\rho}{\rho_0}, \tag{3.5}$$

Here, the coefficients are given as:

$$b_0 = (1.00 \pm 0.34) \cdot 10^{-2},$$
$$b_1 = (2.86 \pm 0.48) \cdot 10^{-4}.$$

From this equation, it can be seen that the sign of the mass shift changes when $\sigma_{sN}/1\,\text{MeV}$ equals $b_0/b_1 = 34.9 \pm 13.1$.
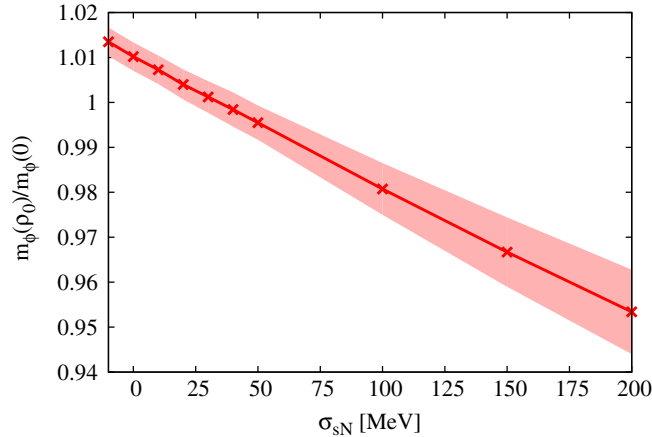

Figure 3.3: Dependence of σ_{N_s} for ϕ mesons in nuclear matter density [31].

Experimentally, measuring the masses of hadrons in finite-density environments requires the production of vector mesons within nuclei and the subsequent measurement of their masses. Prior experiments include heavy-ion collision experiments such as the NA60 experiment conducted at CERN and the HADES experiment at GSI. In the NA60 experiment, changes in the mass spectrum of the ρ meson were observed, which were ultimately concluded to result from a broadening of the mass width. Similarly, the HADES experiment reported changes in the mass spectrum of the ω meson.

On the other hand, proton and photon beam experiments, such as the CBELSA-TAPS experiment at ELSA and the CLAS experiment at Jefferson Laboratory, have investigated the behavior of ρ, ω, and ϕ mesons in medium. However, these experiments did not observe definitive mass changes that could be directly linked to the partial restoration of chiral symmetry. In contrast, the KEK-PS E325 experiment observed a significant mass reduction for the ϕ meson.

3.2.2   KEK-PS E325 experiment

The KEK-PS E325 experiment was the first in the world to demonstrate that the mass of the ϕ meson decreases within nuclear matter. This experiment was conducted at the KEK proton synchrotron, where $12\,\mathrm{GeV}$ protons were incident on carbon and copper targets. The mass spectra of vector mesons were measured through the reaction:

$$p + A \rightarrow \rho, \omega, \phi + X \rightarrow e^+ e^- + X', \tag{3.6}$$

where vector mesons decay into electron-positron pairs.

Figure 3.4a shows the invariant mass spectrum of $e^+ e^-$ pairs obtained in the E325 experiment. The fitting in Fig. 3.4a represents the observed invariant mass distribution of $e^+ e^-$ pairs, modeled as contributions from hadronic decay processes, including $\rho \rightarrow e^+ e^-$, $\omega \rightarrow e^+ e^-$, $\phi \rightarrow e^+ e^-$, $\eta \rightarrow e^+ e^- \gamma$, and $\omega \rightarrow e^+ e^- \pi^0$, as well as background estimated using the event-mixing method.

From this analysis, an excess in yield is observed on the low-mass side of the ω meson peak, in the region of $0.6 \sim 0.76\,\mathrm{GeV}/c^2$. This excess is interpreted as a modification of the mass spectra of ρ and ω mesons.

To reproduce the observed mass distribution, a comparison was made between the data and a model that considers mass modifications of mesons in a medium. In this model, the density dependence of the ρ and ω meson masses is assumed as follows:

$$\frac{m_\omega(\rho)}{m_\omega(0)} = 1 - k\frac{\rho}{\rho_0}, \tag{3.7}$$

where ρ represents the density of the system, and ρ_0 denotes the standard nuclear density. The fit to the data using this assumption yielded a value of $k = 0.092 \pm 0.002$, indicating that the masses of the ρ and ω mesons decrease by 9% at standard nuclear density.

Figure 3.4b shows the invariant mass distribution of $e^+ e^-$ pairs, fitted for the ϕ meson using a Breit-Wigner distribution combined with a quadratic polynomial for the background. For data obtained with a copper target in the region $\beta\gamma < 1.25$, an excess on the low-mass side of the ϕ meson peak was observed.

Similar to the approach above, the mass modification of the ϕ meson in a medium was modeled as:

$$\frac{m_\phi(\rho)}{m_\phi(0)} = 1 - k_1\frac{\rho}{\rho_0}, \tag{3.8}$$

and to explain the observed 22% excess in the ϕ meson mass for $\beta\gamma < 1.25$, a broadening of the decay width was also considered:

$$\frac{\Gamma_\phi(\rho)}{\Gamma_\phi(0)} = 1 + k_2\frac{\rho}{\rho_0}. \tag{3.9}$$

Using these models, the best-fit parameters were determined to be $k_1 = 0.034^{+0.006}_{-0.007}$ and $k_2 = 2.6^{+1.8}_{-1.2}$. These results indicate that at standard nuclear density, the ϕ meson mass decreases by 3.4% and its decay width increases by a factor of 3.6.

However, this result corresponds to σ_{sN} being greater than $100\,\mathrm{MeV}$ in the calculation of Eq. 3.5, which is inconsistent with recent lattice QCD data suggesting that σ_{sN} is less than $70\,\mathrm{MeV}$.
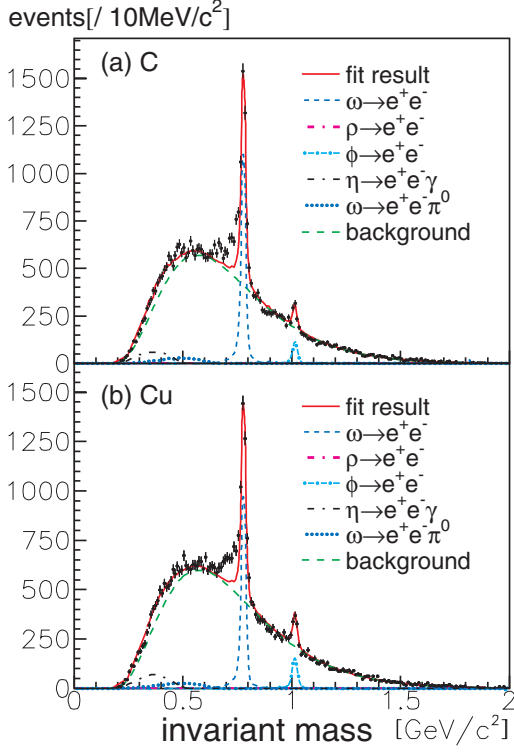
(a) Invariant mass distribution of e^+e^- pairs over the entire mass range [32]. The top panel shows the results for the C target, while the bottom panel corresponds to the Cu target. The solid lines represent the fitting results, which include contributions from $\omega \to e^+e^-$, $\phi \to e^+e^-$, $\eta \to e^+e^-\gamma$, $\omega \to e^+e^-\pi^0$, and the background.
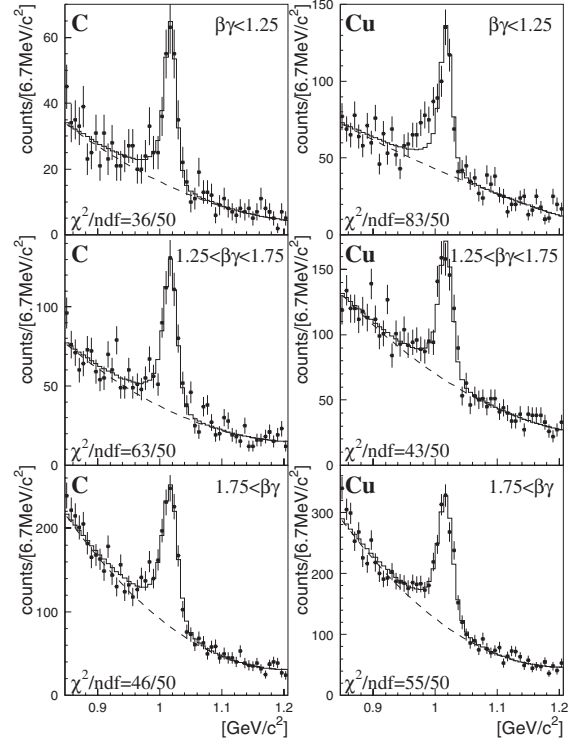
(b) Invariant mass distribution of e^+e^- pairs near the ϕ meson mass [33]. The solid lines represent the fitting results, which include the $\phi \to e^+e^-$ peak and the background. The left column shows the results for the C target, while the right column corresponds to the Cu target. Each is divided into three regions based on the value of $\beta\gamma$.

Figure 3.4: The invariant mass spectrum obtained from the KEK-PS E325 experiment.

3.3   Purpose of the J-PARC E16 experiment

Although many experiments have been conducted to study the mass distribution of vector mesons in nuclear matter, no clear conclusions have been reached. The main reasons for this are the lack of sufficient statistical precision and mass resolution. For example, in the KEK-PS E325 experiment, the analysis of the mass reduction of vector mesons depended heavily on models due to these limitations.

To address these issues, the J-PARC E16 experiment was designed. Similar to the KEK-PS E325 experiment, the J-PARC E16 experiment aims to measure the mass of vector mesons in nuclear matter by a high-intensity proton beam with nuclear targets. Compared to the KEK-PS E325 experiment, it offers the following advantages:

- 10 times higher beam intensity (1×10^{10} protons/spill ($2\,\mathrm{sec}$))

- 5 times greater acceptance

- 2 times higher production cross-section for ϕ mesons

- Improved mass resolution of approximately $5\,\mathrm{MeV}$

These improvements aim to achieve 100 times the statistical precision and twice the mass resolution compared to the preceding experiments.

Currently, multiple commissioning runs have been conducted since February 2020, with the latest commissioning run, Run-0e, completed in 2024. While discussions are still ongoing, the full-scale physics data acquisition run, Run-1, is expected to commence in the spring of 2025.

3.4   Experimental Facility

3.4.1   J-PARC

J-PARC (Japan Proton Accelerator Research Complex) is an experimental facility jointly constructed by KEK (High Energy Accelerator Research Organization) and JAEA (Japan Atomic Energy Agency). The facility provides high-energy proton beams and various secondary beams, succeeding the KEK-PS, which ceased operation in 2005. Figure 3.5 shows an aerial photograph of the J-PARC site. Negative hydrogen ions generated in the ion source are accelerated to 400 MeV in the LINAC linear accelerator. These ions pass through a carbon film, where they are converted to proton beams, and are then sent to the Rapid Cycling Synchrotron (RCS). Beams from LINAC are injected into RCS at a frequency of 324 MHz (3 nsec), using an adjustable injection pattern to fill a single RCS bucket at a desired intensity, with a maximum bucket length of 500 μsec. The protons in the RCS are then accelerated to 3 GeV and extracted by a kicker magnet. The extracted beam is transported to either the Materials and Life Science Experimental Facility (MLF) or the Main Ring (MR). Injection, acceleration, and extraction at the RCS are repeated at a frequency of 25 Hz.

The MR is a synchrotron with a circumference of about 1.6 km, where proton beams are accelerated up to 30 GeV before being directed to the Hadron Experimental Facility and the Neutrino Experimental Facility. In typical scattering experiments, since reactions are detected one event at a time, it is ideal to extract a low-intensity beam over an extended period of time. For this reason, beam transport to the Hadron Experimental Facility involves the "slow extraction (SX)" method, in which 10^{13} protons are extracted over a span of two seconds.
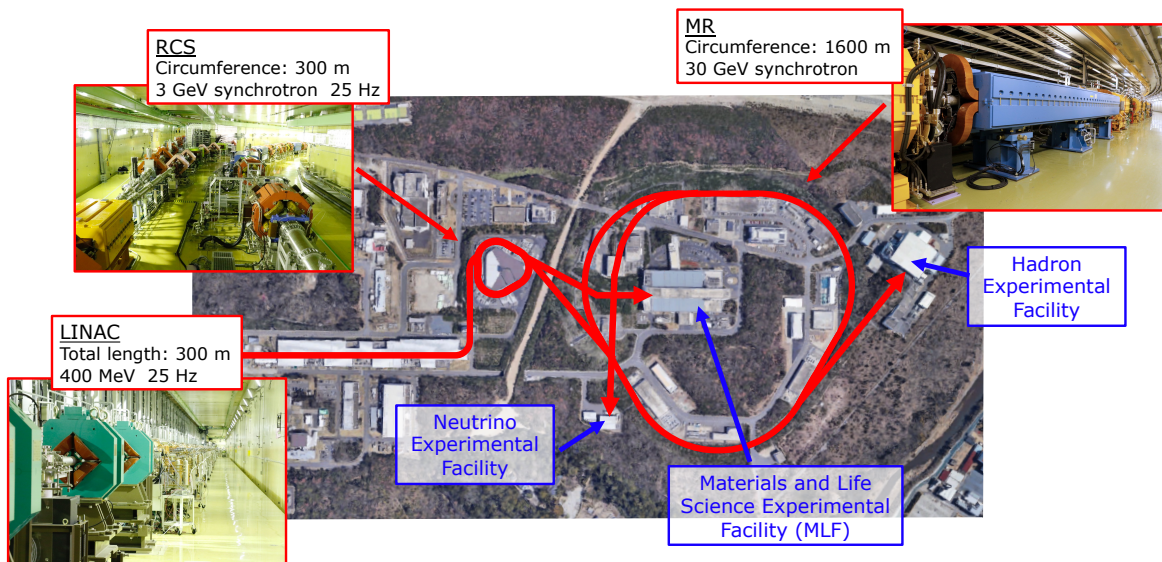

Figure 3.5: J-PARC aerial photograph: accelerators and experimental facilities [34].

3.4.2   Hadron experimental facility and high-p beamline

The proton beam extracted from the MR is transported through the primary beamline along a 200 m section called the switch yard (SY) to the secondary particle production target (T1) located

in the hadron experimental hall (Figure 3.6). Secondary particles, such as K, π mesons, and antiprotons, produced at the secondary particle production target are transported to their respective experimental areas via secondary beamlines.

The Lambertson magnet, located about 100 m upstream of T1 in the switchyard, splits the proton beam by about 0.02% and transports it to the high-p beamline in the hadron experimental hall. This high-momentum beamline is used in the E16 experiment. Fig. 3.6 shows the high-momentum beamline, the switchyard, and the hadron experimental hall.
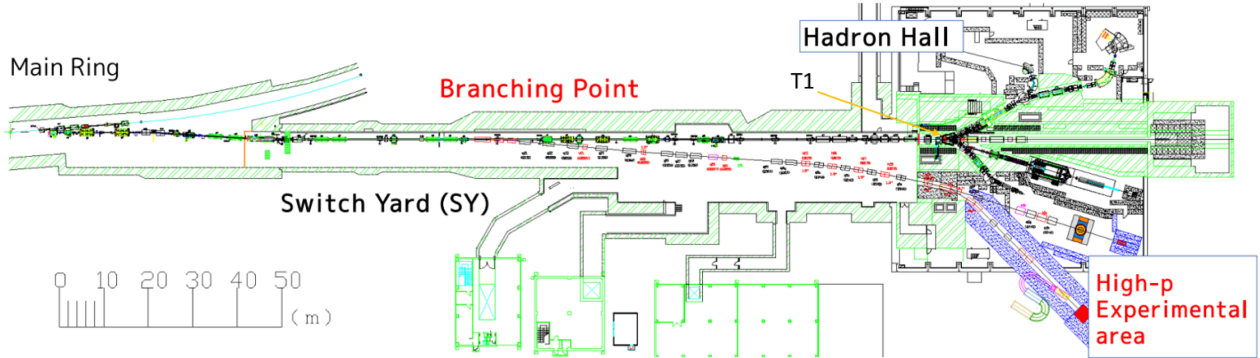

Figure 3.6: High-p beamline.

3.5   Target

In the E16 experiment, thin films of polyethylene, carbon, copper, and lead are used as nuclear targets. The thicker the target, the higher the number of reactions and the higher the yield, but the background due to electron pair production from gamma rays also increases. Therefore, the target thickness should be set so that the total interaction length is less than 0.2% and the radiation length is less than 0.5%. Specifically, one carbon target of 500 μm and two copper targets of 80 μm are used for Run-0 and Run-1.
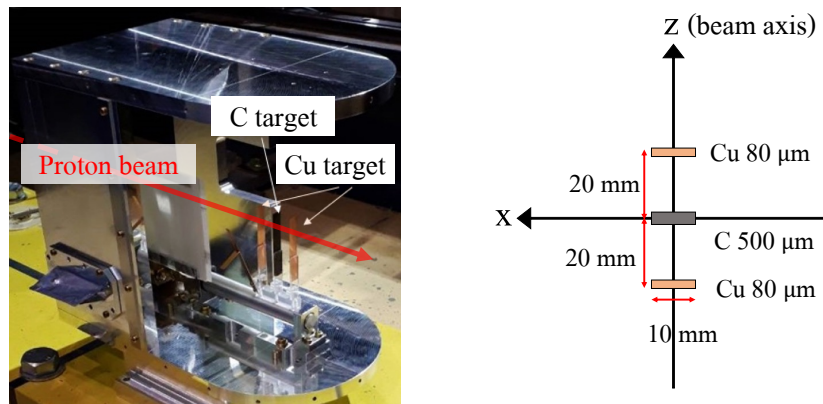

Figure 3.7: Target chamber (left) and target geometry (right) for commissioning runs and Run-1.

The targets are placed in a chamber filled with helium gas to reduce area activation caused by

beam energy loss. The left panel of Figure 3.7 shows the target chamber used during the commissioning runs and Run-1, while the right panel illustrates the geometry of the targets.

3.6   Spectrometer

The spectrometer used in the E16 experiment consists of four types of detectors, with their roles divided into two categories: momentum measurement and particle identification (electron identification). The STS and the GEM tracker (GTR) are used for momentum measurement. These two detectors detect the tracks of charged particles in a magnetic field and measure their momentum. Outside of these, the Hadron Blind Detector (HBD) and Lead Glass calorimeter (LG) are used for particle identification. A set of detectors is referred to as "one module." This set covers ±15 degrees vertically and 30 degrees horizontally (Figure 3.8 right). In Run-1 (2025. Spring-), eight modules in the central row are primarily used, covering ±135 degrees horizontally. In Run-2, additional modules in the upper and lower rows will be installed to cover ±45 degrees vertically (Figure 3.9). The modules are named counterclockwise, as shown in Figure 3.8 left. Modules in the central row are designated with numbers in the 100s, while those in the upper row are designated with numbers in the 200s. The following section explains the electromagnets and detectors used in the E16 experiment.
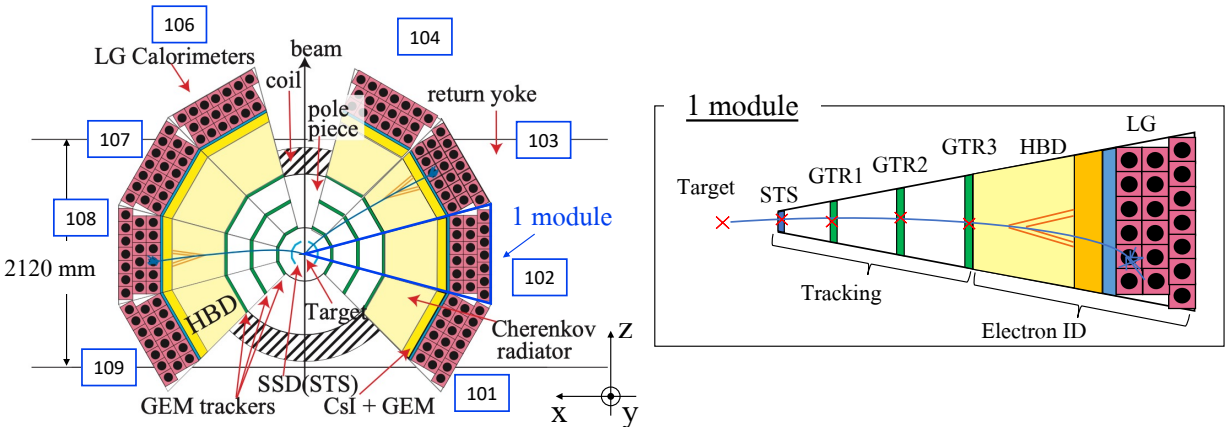

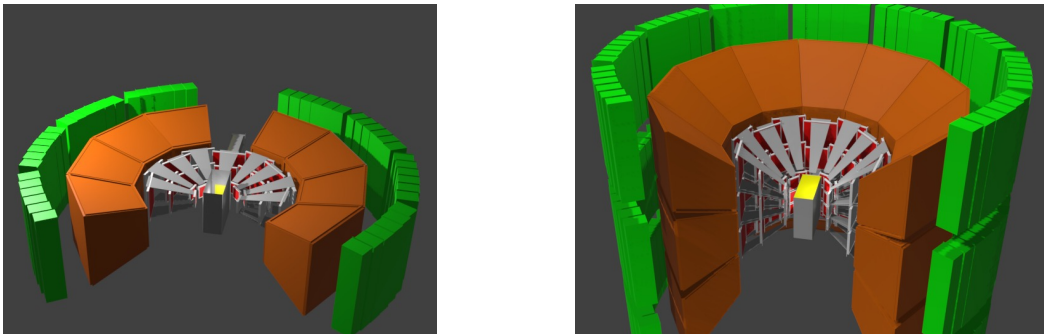Figure 3.8: J-PARC E16 spectrometer (top view).

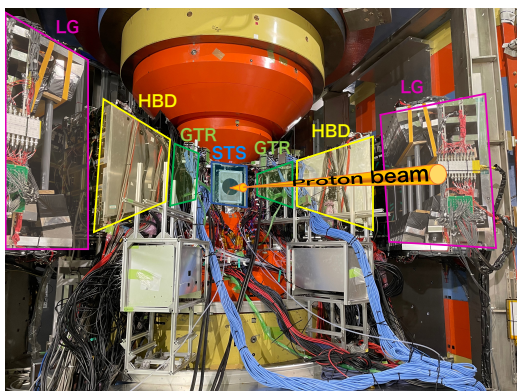Figure 3.9: J-PARC E16 Run-1 (left) and Run-2 (right) setups.

Figure 3.10: J-PARC E16 spectrometer in Run-0e.

Figure 3.11: FM magnet.

3.6.1   Magnet

For the spectrometer magnet, we use the so-called "FM magnet" used by the KEK-PS E325 experiment, which was originally the FM-Cyclotron at INS, University of Tokyo. The current flowing through the coil during the experiment was 2450 A, and the central magnetic field was 1.77 T. The yoke was 5.3 m wide, 4.9 m high, and 2.1 m deep, and the gap between the magnets was 400 mm (Fig. 3.11) [35].

3.6.2   Detectors

■ Tracking detectors

・Silicon Tracking System (STS)

The STS is the innermost tracking detector in the E16 experimental setup. Using the 60 mm square sensors from the CBM STS (Fig. 2.5), they are positioned about 120 mm from the center of the spectrometer. The STS was installed for the first time during the E16 commissioning run in 2023 (Run-0d). For more details on its installation in the E16 experiment, refer to Chapter 4.

・GEM Tracker (GTR)

The GTR is a micro-pattern gas detector that works in conjunction with the STS to detect charged particle tracks in the E16 experiment. A GEM (Gas Electron Multiplier) is a plate-shaped detector component with microscopic holes. It is manufactured by vapor-depositing metal onto both sides of a thin insulator and then perforating it with microscopic holes. When a voltage is applied between the metal layers, a high electric field is generated around the holes, as illustrated in Figure 3.12 (left). This electric field amplifies electrons that enter the holes.

The left pannel of Figure 3.13 illustrates a conceptual diagram of the GTR [36]. The GTR features a layered structure composed of the following components, arranged from top to bottom: Mylar, a MESH, three GEMs, a Read-Out foil, and an aluminum base frame. All components, except for the aluminum base frame, are mounted on square frames made of glass epoxy.
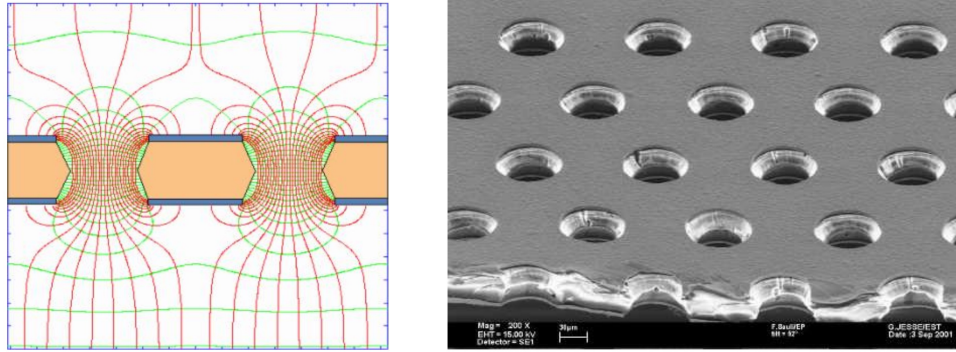
Figure 3.12: Conceptual diagram of GEM (left) and photograph (right) [37].

The chamber is filled with a mixed gas of $ArCO_2$ (70 : 30). Incoming electrons and positrons cause ionization reactions in the gas. The space between the MESH and the first GEM is called the "drift gap", where an electric field is applied in the direction from the GEM toward the MESH. This field causes electrons ionized in the drift gap to drift toward the GEM, where they are amplified. Similarly, electric fields are applied in the transfer and induction gaps shown in the diagram. These fields allow the electrons to be repeatedly amplified as they move toward the Read Out foil. The amplified electrons induce a negative charge on the electrodes of the foil, which is then read out as a data signal.

Each module consists of three layers of GTR chambers with inner dimensions of 100 mm square, 200 mm square, and 300 mm square, referred to as GTR100, GTR200, and GTR300, respectively. These layers are mounted on frames made of carbon fiber-reinforced plastic (CFRP), as shown in Fig. 3.13 right [36].
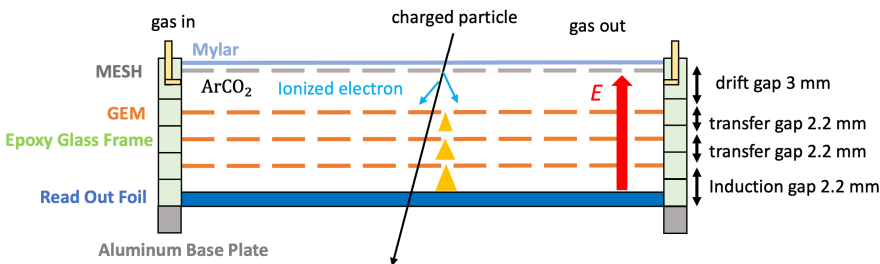

Figure 3.13: Conceptual diagram of GTR (left) and the CFRP frame and the provisionally mounted GTR are shown (right). The black frame is the CFRP frame, and from left to right on the middle tier are the GTR100, GTR200, and GTR300 [36].

The GTR readout foil strips are composed of X-strips and Y-strips arranged orthogonally to each other. To achieve the position resolution of $100\,\mu m$ required, the X-strip pitch is designed to be $350\,\mu m$, while the Y-strip pitch is $1400\,\mu m$. The signals from these strips are read out using the APV25 chip[1]. Although not shown in Fig. 3.13, the GTR300 also functions as a trigger for event selection. A circuit designed to read the trigger signal is connected to the back of the third GEM in the GTR300.

■ Particle ID detectors (Electron ID detectors)

・Hadron Brind Detector (HBD)

The Hadron Blind Detector (HBD) is a gas Cherenkov-type electron detector proposed by Y. Giomataris and G. Charpak [38], developed for the PHENIX experiment [39]. The HBD used in this experiment is based on the PHENIX design and features:

- CF_4 gas as both the radiator and amplification gas.
- GEMs as the amplification component.
- CsI photocathodes deposited on the GEM surface.

Unlike conventional electron detectors, which require mirrors and photomultiplier tubes, the HBD achieves large acceptance with this design. Electrons emit Cherenkov light in CF_4 gas, which is converted to photoelectrons by CsI photocathodes and amplified by the GEMs.

Pions, with a Cherenkov threshold of $4.0\,GeV/c$, emit minimal Cherenkov light in this experiment. Additionally, a reverse voltage between the MESH and the first GEM suppresses signals from pion ionization. These mechanisms enable a pion rejection rate of 98% and an electron detection efficiency of 68%.

The HBD readout pads are positioned $1400\,mm$ from the center. Figure,3.14 shows a conceptual diagram (left) and two HBD modules (right).
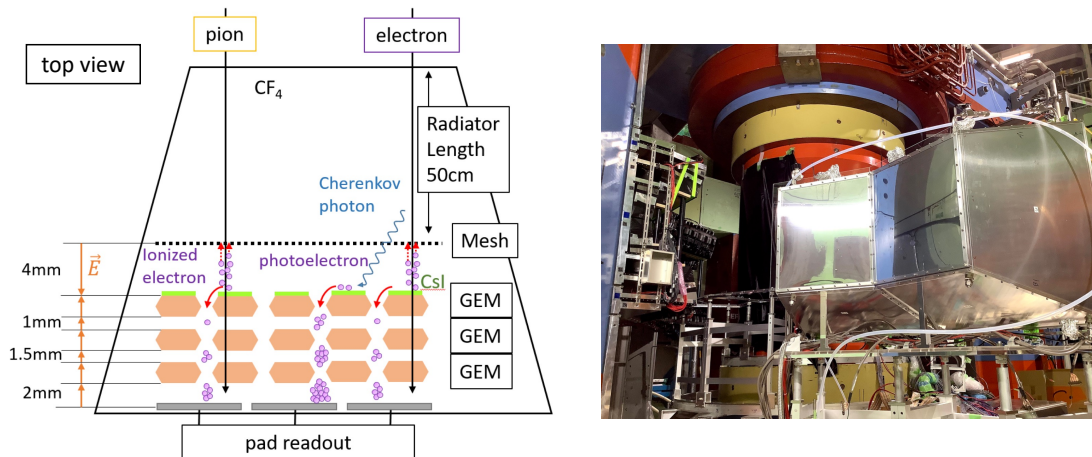

Figure 3.14: Conceptual diagram of HBD (left) and photo of two modules (right) [40].

<hr>

[1]The APV25 chip was developed by CMS for silicon strip detectors and has been widely used as a readout circuit for GEM detectors under the RD51 collaboration.

• Lead Glass Calorimeter (LG)

The Lead Glass Calorimeter (LG) is an electromagnetic calorimeter that uses lead glass as its radiator. It identifies electrons and positrons by leveraging the difference in the amount of light produced by electrons and pions in the lead glass. When an electron enters the lead glass, it emits photons via bremsstrahlung. These photons then generate electron-positron pairs through pair production. This process repeats, resulting in an electromagnetic shower and producing Cherenkov radiation.

The cross-section of bremsstrahlung for charged particles is inversely proportional to the square of the particle's mass, meaning the amount of light produced by pions is significantly smaller than that produced by electrons. Furthermore, while pions can produce Cherenkov light either directly or through nuclear reactions such as $\pi^0 \rightarrow \gamma + \gamma$, these contributions are minimal. Thus, by detecting the Cherenkov light with a photomultiplier tube and utilizing the difference in light intensity, electrons can be identified.

The LG achieves an electron detection efficiency of 90% and a pion rejection rate of 92.7% [40]. Figure 3.15 shows a photograph of one LG block (left) and a schematic diagram of one LG module (right).
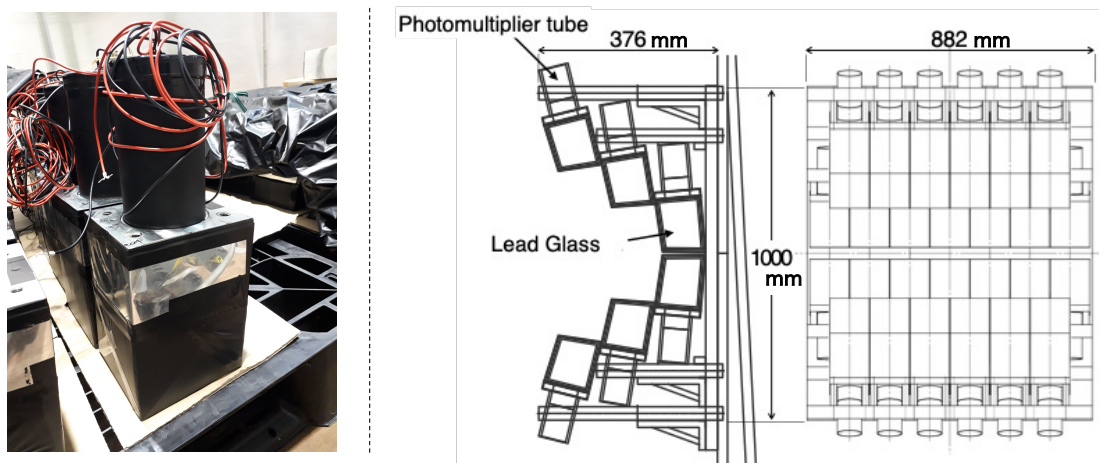

Figure 3.15: Photograph of one LG block (left) and a schematic diagram of one LG module (right).

3.7   E16 DAQ and Trigger System

The J-PARC E16 experiment acquires data using a trigger system. The trigger signal is generated from discriminator signals of 2,620 channels, including those from the third GTR layer (GTR300), the HBD, and the LG. Timing coincidences and position matching among these three detectors are used to identify two electron tracks originating from the target. The trigger decision and issuance are handled by the Belle-2 Universal Trigger Board 3 (UT3), which processes signals from multiple detectors and generates trigger signals to the data acquisition system.
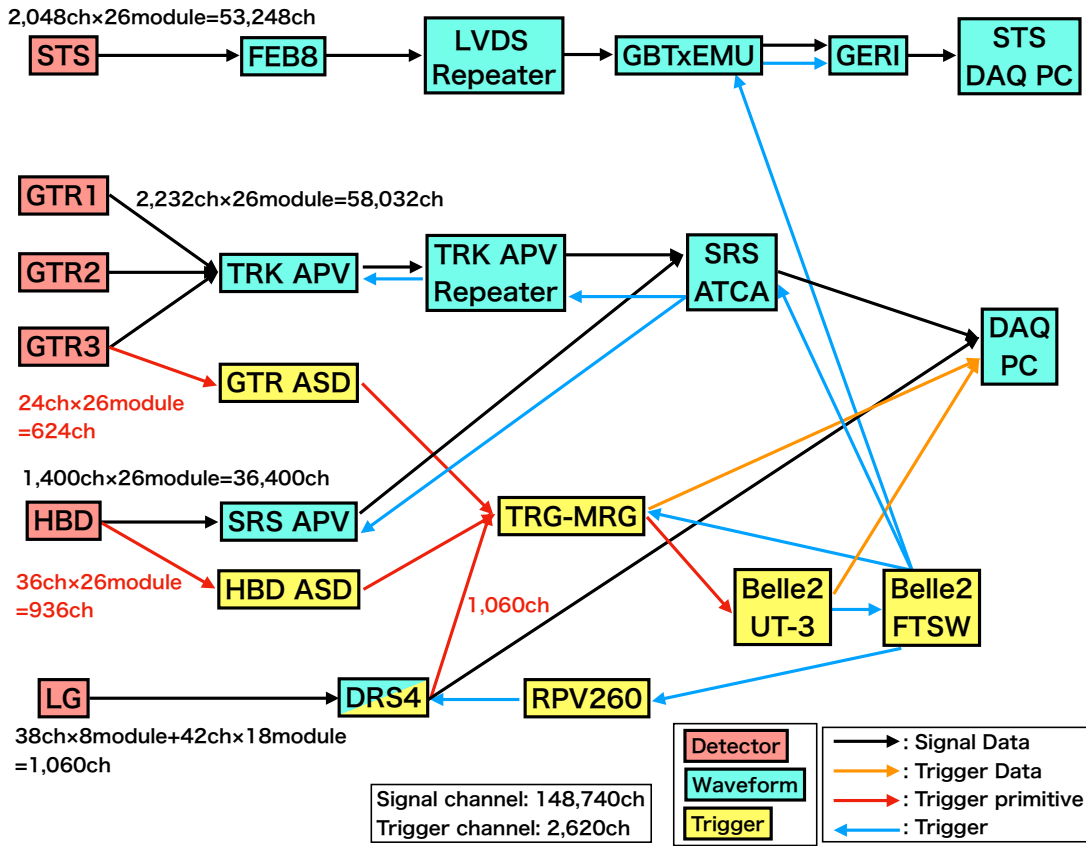
Figure 3.16: E16 DAQ and trigger system.

The primary background events consist of electron pairs generated by reactions such as

- $\pi^0 \to \gamma e^+ e^-$
- $\pi^0 \to 2\gamma$, $\gamma \to e^+ e^-$

However, electron pairs from these reactions typically have a small opening angle, allowing many of them to be rejected by applying a restriction on the opening angle. Through this process, the trigger rate is reduced to approximately 1 kHz while limiting the loss of ϕ-mesons to 26%.

Chapter 4

STS for the J-PARC E16 experiment

The CBM STS sensors were installed as the innermost tracking detector in the E16 experiment for the first time at the fourth E16 commissioning run in 2023 (Run-0d). Data acquisition from the STS using the E16 trigger was conducted for the first time at the fifth commissioning run in May 2024. This chapter explains the performance requirements for the innermost SSD of E16, the E16 STS chamber, the readout chain, and the installation status.

4.1   J-PARC E16 inneromost SSD performance requirements

The J-PARC E16 experiment aims to achieve 100 times more statistical data compared to the previous KEK-PS E325 experiment. To reach this goal, the innermost tracking detector (SSD) is required to have a detection efficiency of 95%. Additionally, the position resolution and time resolution required for the SSD to achieve the mass resolution goal of approximately $5\,\mathrm{MeV}/c^2$ in the E16 experiment are summarized in Table 4.1.

Table 4.1: Performance requirements for the innermost SSD in the J-PARC E16 experiment.

Parameter	Value
Position resolution (x)	$25\,\mathrm{\mu m}$
Time resolution	6 nsec
Detection efficiency	95%

4.1.1   Time resolution

The innermost SSD detects charged particle tracks in the E16 spectrometer with the GTR. For track candidates identified only by the three GTR layers, a time window of approximately 300 nsec is applied to correct the position of angled tracks using the timing of the hits (Section 6.2.2). During this 300 ns time window, particles such as electrons and positrons produced from the decay of ϕ mesons, as well as background particles originating from the proton beam halo, are detected simultaneously. To make full use of the high-intensity proton beam at J-PARC, a detector with both high rate capability and effective background suppression is essential.

In particular, since this experiment focuses on measuring lepton pairs, it is crucial to suppress the dominant hadronic background. The SSD works in combination with the GTR to select hits that match event timing with a high resolution of a few nanoseconds. By doing so, it becomes

possible to reduce fake hits. Only the track candidates associated with these hits are used, which effectively suppresses the background (Fig. 4.1).
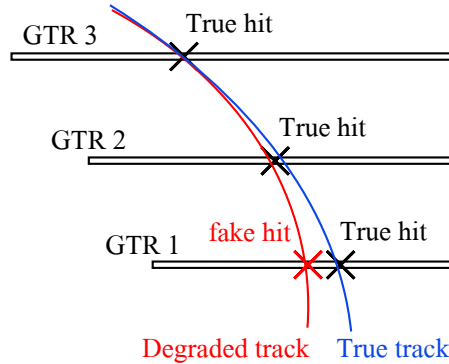

Figure 4.1: The true track and the track degraded by the GTR time resolution.

4.1.2   Detection efficiency

In the E16 spectrometer, each module is composed of six layers of detectors: SSD, three GTR layers, HBD, and LG. Therefore, the detection efficiency of each detector is crucial to ensure sufficient statistics. The detection efficiency of the innermost SSD alone is expected to reach 95% [1].

4.1.3   Position resolution

The mass resolution, when ignoring the background caused by fake tracks, shows little difference between configurations with and without the innermost SSD. This is because the SSD itself has a certain thickness, and its material budget degrades the mass resolution. Considering this material budget, a position resolution of 25 µm is required to achieve sufficient mass resolution.

Due to these requirements, the CBM STS came to be used as the E16 innermost SSD. Additionally until Run-0c, SSDs using the APV25 chip for readout were employed; however, these sensors were mounted on large-framed substrates. To facilitate the detector expansion planned for Run-2, the system transitioned to the CBM STS [41].

---

[1]This value applies to particles with momentum of $1\,\mathrm{GeV}/c$ or higher.

4.2 J-PARC E16 STS chamber

This section explains the chamber and sensor arrangement of the E16 STS.

Figure 4.2 (left) shows a 3D image of the E16 STS setup at the commissioning runs (Run-0d, Run-0e) and Run-1. Ten 62 mm square sensors (Section 2.2.1) equipped with FEB-8 (ver. 2.3) are mounted on eight ladders. Each ladder is 231 mm tall and can accommodate up to three sensors, allowing for future upgrades. Eight sensors (101-104, 106-109) are mounted at the center positions of the ladders. Two additional sensors, 206 and 207, are placed above sensors 106 and 107, respectively. Inside the setup, a target chamber is installed, containing experimental targets at its center.
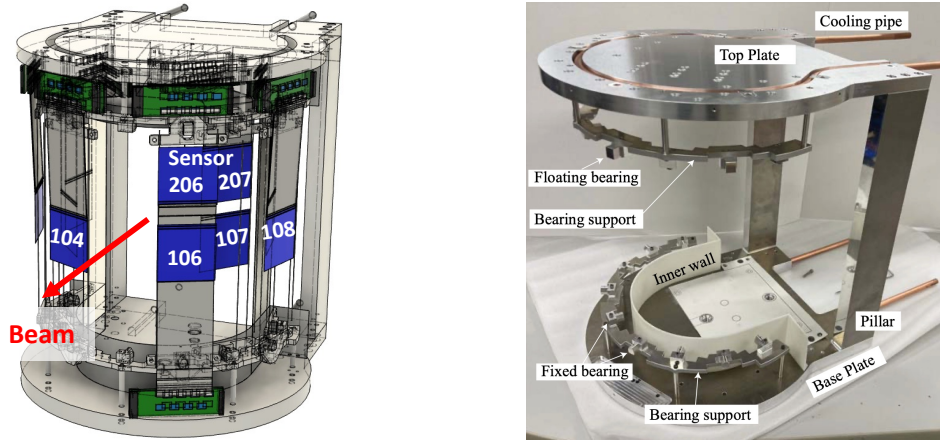

Figure 4.2: J-PARC E16 STS Chamber. Left figure shows a 3D image of the E16 STS Chamber for Run-1 (Run-0d, Run-0e). Right figure shows a photograph of the E16 STS chamber without the ladders installed.

Fig. 4.2 (right) shows a photograph of the constructed structure of the J-PARC STS chamber. Since thick materials are not permitted in the acceptance and beam-penetrating area, the J-PARC STS chamber was designed with the top and bottom plates supported by only two pillars located upstream in the configuration. Two copper pipes are installed inside the plates to provide water cooling for the FEB-8s. Aluminized mylar sheets (outer: 12.5 μm, inner: 25 μm) and black sheets ($115 \, \text{g/m}^2$) are used to cover the outer side (R = 170 mm) and inner side (R = 105 mm) of the structure, preventing light intrusion and electrical noise (Figure 4.5).

All modules are designated so that the side with the ladder structure corresponds to the P-side of the silicon sensor, while the side without the ladder structure corresponds to the N-side. Odd-numbered modules are oriented with their P-side facing outward, while even-numbered modules are oriented with their N-side facing outward. This alternating arrangement is designed to maximize acceptance. Odd-numbered modules are referred to as "inner ladders" and are positioned at a distance of 117.386 ± 0.16 mm from the center of the spectrometer. Even-numbered modules are referred to as "outer ladders" and are positioned at a distance of 148.81 ± 0.16 mm from the center of the spectrometer (Figure 4.3).
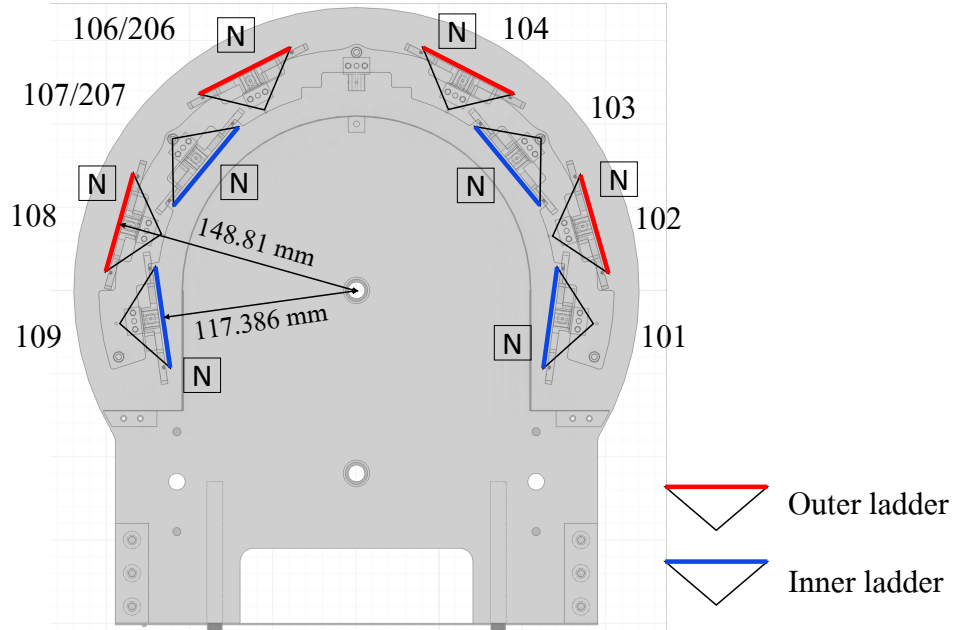
Figure 4.3: J-PARC E16 STS chamber top view image.

Table,4.2 summarizes the specifications of the ladders to be constructed. At the time of the design decision, custom micro-cables were unavailable. Therefore, existing cables that fit the required compact configuration were selected. Importantly, some modules use cables of the same length on both the P- and N-sides, which differs from the design of the CBM STS.

The installation of the ladders onto the chamber was completed in May 2023 before Run-0d. Figure 4.5 shows the STS chamber with all the ladders installed.

Table 4.2: Ladders to be constructed for Run-0d and Run-0e. *See Appendix A.2 for Run-1 ladders

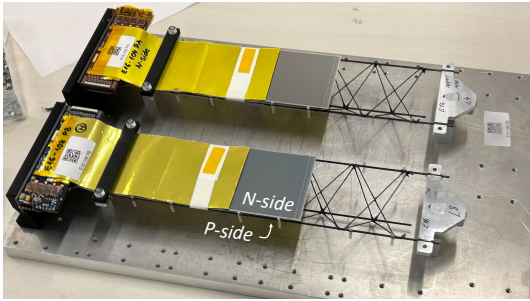| Ladder No.	Sensor No.	Micro-cable [mm] N	P	Radius ± 0.16 [mm]	Estimate data rate /ASIC [Mbps]
L9	109	142	131	117.386	110
L8	108	121	121	148.81	110
L7	107	121	110	117.386	240
	207	172.5	163.1	117.386	240
L6	106	121	121	148.81	320
	206	207.7	207.7	148.81	320
L4	104	121	121	148.81	240
L3	103	172.5	163.1	117.386	160
L2	102	121	121	148.81	80
L1	101	142	131	117.386	80

Figure 4.4: J-PARC E16 STS ladders. Ladders uninstalled from the chamber to repair: L8 and L4. The ladder side faces the P-side.
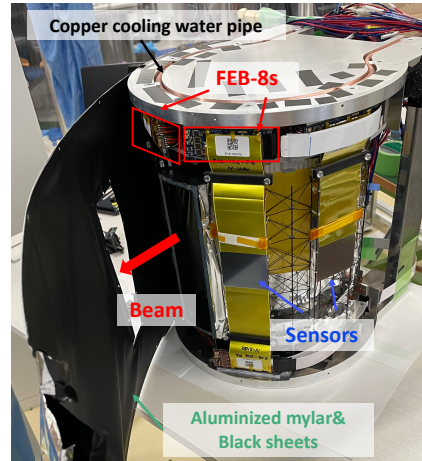

Figure 4.5: J-PARC E16 STS chamber with all ladders installed.

4.3   J-PARC E16 STS readout chain

This section provides an explanation of the STS readout chain used in the J-PARC E16 experiment. The DAQ (Data Acquisition) system for the STS independently, separate from other systems, as shown in Fig. 3.16. The E16 STS readout chain is essentially a modified version of a circuit originally designed for medium-scale experiments in the CBM. This section begins with an overview of the circuit, followed by details on its development and the functionality of its individual components.
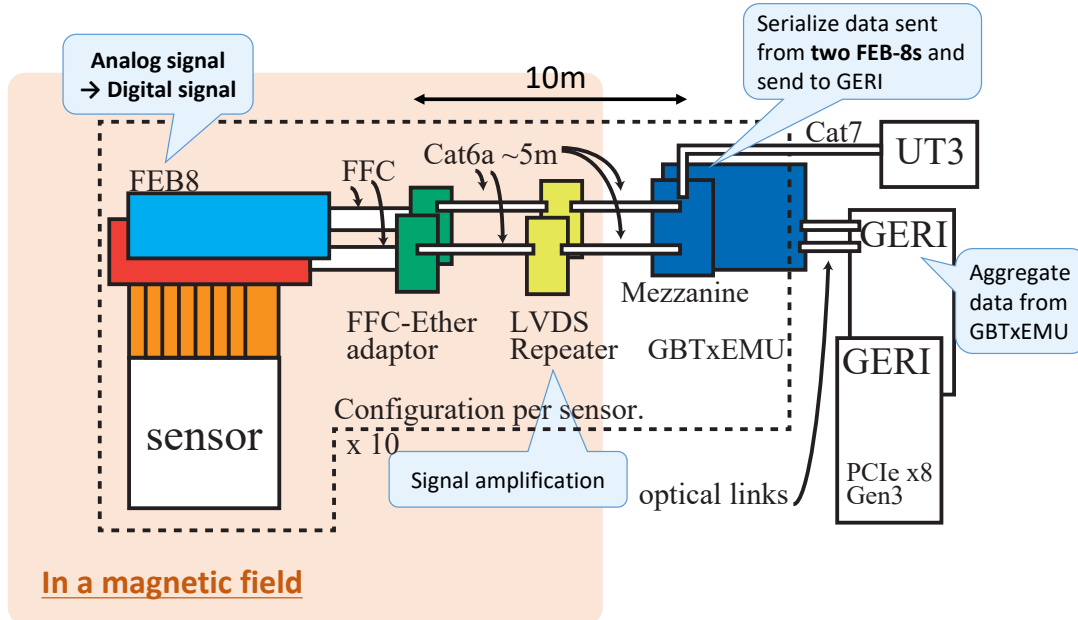

Figure 4.6: J-PARC E16 STS readout chain.

Figure 4.6 illustrates a schematic diagram of a single module in the STS readout chain. When a charged particle passes through the sensor, it deposits charge on the strips, which is sent as analog signals to the SMX on the FEB-8. The SMX processes this signal and transmits it downstream as digital signals. The signals, transmitted downstream via an FFC (Flexible Flat Cable), is further sent through a Cat6a cable for long-distance transmission, where it is received by the GBTxEMU. The GBTxEMU serializes data from two FEBs and combines it into one sensor's data. The data is then sent further downstream, where the GERI board integrates information from all sensors (up to seven sensors per GERI board) and transmits it to the PC.

In this readout chain, a component unique to the J-PARC E16 experiment is the LVDS repeater, which is used for long-distance transmission. The following sections describe this component, along with the modifications made for its implementation in J-PARC E16 experiment.

4.3.1   Development of the readout chain for the J-PARC E16 experiment

This section explains the modifications made to the readout chain for the installation of the STS in the J-PARC E16 experiment. The modifications were mainly focused on the following three aspects.

1. Long-distance transmission   The GBTxEMU used for STS data serialization in the E16 experiment differs from that used in the CBM experiment, as it has lower resistance to magnetic fields and radiation. Signals from the FEB-8 are transmitted downstream using FFC; however, FFC are not suitable for long-distance transmission and can only cover distances of up to approximately 30 cm. In the E16 experimental environment, their position is within a magnetic field region and exposed to significant radiation. Therefore, long-distance transmission of about 10 m is required. To address this, modifications were made to enable transmission from the FEB-8 to the GBTxEMU using 5 m Cat6a cables and LVDS repeaters (signal amplifying relays) [42].

2. High hit-rate capability   The expected interaction rate reaches to about 10 MHz by a fixed target with 1×10^{10} per spill beam of 30 GeV protons. The STS, located closest to the target, also experiences high hit rates. The highest hit rate is expected in the most forward 106 module, reaching up to 64 Mhits/sec [42]. With such a high hit rate, the bandwidth of a standard DAQ system is insufficient. To address this issue, the firmware was upgraded to serialize the data encoded by the FEB-8 using a GBT-FPGA and to decode it before reaching the GERI [42].

3. Recording of E16 trigger information   The E16 experiment mainly acquires data by triggering (Section 3.7). Therefore, firmwares of GERI and GBTxEMU were modified to perform online selection of hits at GERI according to the E16 trigger timing. This online selection system was implemented in April 2024 (Section 4.4). The Run-0e data-taking was conducted with this system.

4.3.2   Readout chain comporments

This section explains the key components of the readout chain in order, starting from the upstream.

FEB-8 (ver. 2.3)

See Section 2.2.3. Each board reads out one side of the sensor and transmits the signal downstream via an FFC.

LVDS Repeater

The FEB-8 transmits signals using LVDS differential signaling, which reduces external noise by utilizing the voltage difference between two wires. However, signal attenuation and noise become challenges in long-distance transmission. According to [42], Cat6a cables can reliably transmit signals up to 5 m.

Since the distance between the FEB-8 and the GBTx-EMU exceeds 10 m, two 5-m Cat6a cables (five per set) were connected via a repeater. This LVDS repeater board (Figure 4.7) was developed as described in [42]. Additionally, test experiments at KEK PF-AR (Chapter 5) revealed issues, leading to subsequent improvements.

GBTxEMU and FMC

The GBTxEMU (GBTx Emulator) board aggregates the data transferred from the FEB-8s and utilizes the GBT-FPGA for data transfer, slow control, and timing and trigger control. In the CBM experiment, the radiation-resistant GBTX ASIC chip is used. However, due to export restrictions on radiation-resistant technology, GBTX ASIC chips cannot be imported into certain regions, including Japan. To address this limitation, the GBTxEMU board was developed. It incorporates the GBT-FPGA [43], which replicates the basic functions of the GBTX ASIC using COTS (Commercial Off-The-Shelf) components, making it accessible in regions where GBTX ASIC chips are restricted (Figure 4.8 blue board).

Figure 4.7: LVDS Repeater.

For signal line input to the GBT, an FMC board is attached (Fig. 4.8 green board). In the CBM experiment, the FMC board is equipped with ZIF connectors to connect FFCs. However, since E16 uses Cat6a cables for input, a new FMC board was developed. This FMC board can accept signals from up to two FEB-8s.

GERI

Data from multiple GBTxEMU boards is transmitted via optical links to a board called GERI (GBTx Emulator Readout Interface) (Figure 4.9). The data received from the GBTxEMU is processed by GERI, which adds information such as timestamps and hit addresses, rearranges hit data, and transfers it to a PC via DMA (Direct Memory Access). The GERI board consists of a Trenz TEC0330, which features a PCI Express interface, and an FM-S18, which provides 8 SFP+ ports [42]. A single GERI board can connect to up to seven GBTs for data acquisition.
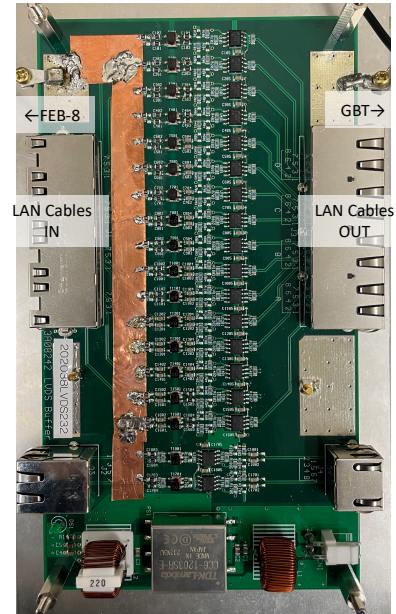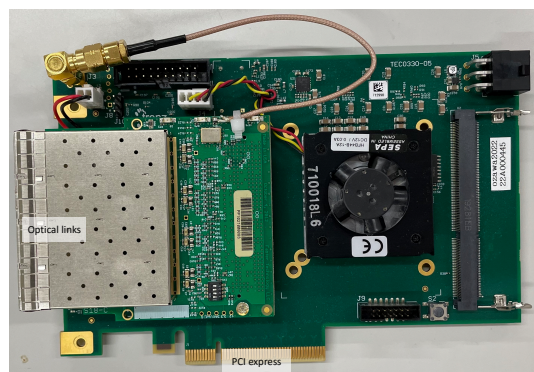
Figure 4.8: GBTxEMU and FMC board.

Figure 4.9: GERI board.

4.4   Online trigger selection

During Run-0e, data acquisition using an online trigger was implemented for the first time for the STS. This section explains the necessity of online trigger selection for the STS, the time synchronization of readout components, and the method of online trigger selection.

4.4.1   Necessity of online trigger selection

All detectors in the E16 experiment except STS acquire data using triggers (Section 3.7). On the other hand, the SMX ASIC, which is is the front-end circuit of the STS, operates under self-trigger mode and sends all the hit information downstream and can be recorded. The hits that corresponds to the E16 triggers can in principle be selected offline. However, it is impractical as the estimated data size would reach about 300 TB/day.[2] Therefore, online trigger selection has been implemented at GERI that sends only hit information that corresponds to the E16 trigger to the PC for recording. This greatly saves the computer resources required for recording and analysis.

4.4.2   Time synchronization of readout components

To perform online trigger selection, it is first necessary to synchronize the timing among the readout components. Generally, synchronization can be classified into the following three types:

1. **Frequency Synchronization** Frequency synchronization refers to the condition in which the clock frequencies at two points match.

2. **Phase Synchronization** Phase synchronization builds upon frequency synchronization and refers to the condition in which the timing of the clock edges is aligned.

3. **Time Synchronization** Time synchronization builds upon both frequency and phase synchronization, ensuring that the timestamps are also aligned.

---

[2]8-byte/hit $\times$ (1 G hit/sec (all FEB-8s) [42])$\times$3600 sec $\times$ 24 hours $\times$ (2 sec spill / 5.2 sec cycle) $\cong$ 300 TB.   *See Appendix B*

Time synchronization is meaningless unless "frequency synchronization" is performed accurately and precisely in the first place. Without it, the timing gradually drifts, much like two pendulums with slightly different lengths.

As shown in Figure 3.16, the STS readout chain operates independently of the E16 DAQ system. The clock master of the STS readout chain is the GERI boards, and all downstream STS readout components operate based on this clock. Furthermore, this clock is not even "frequency synchronized" with the E16 DAQ clock. Therefore, the arrival time of the E16 trigger at the STS readout chain are recorded and used to determine whether hits are coincident with the trigger. This will be explained in the next section. In Run-0e (Run-1), we used (will use) two GERI boards to result in two independent clocks (Figure 4.11). The acquisition of trigger information and the E16 timestamp is recorded by the GBTxEMU downstream of the GERI simultaneously.

The following provides a brief explanation of the time synchronization between STS readout components.
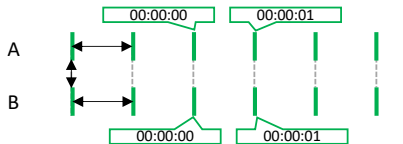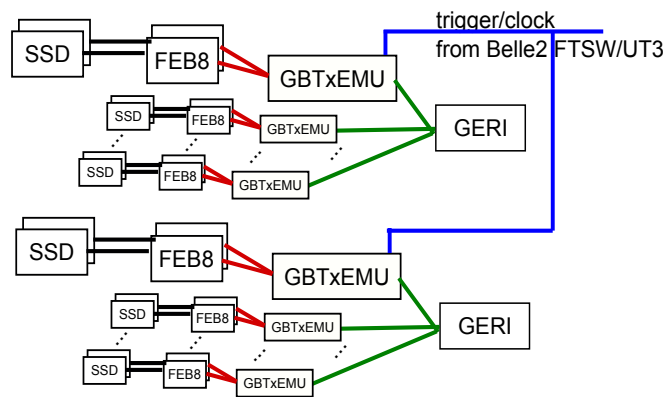

Figure 4.10: Three types of synchronization.

Figure 4.11: E16 STS readout chain.

GERI-GERI

Frequency synchronization between GERIs is not performed. Each GERI has one GBTxEMU to receive E16 triggers and timestamps (see the blue one in Fig. 4.11). Timestamp offsets are adjusted during offline analysis. The GERI clock runs at 40 MHz and records a 32-bit timestamp (`geriTimestamp`).

GERI-GBTxEMU

Using the 40 MHz clock supplied by GERI, GBTxEMU generates a 160 MHz clock and records a 320 MHz, 64-bit timestamp (`emu_tdc`). This clock is synchronized with the GERI clock.

GBTxEMU-SMX

The SMX does not generate a clock. Instead, it utilizes the rising and falling edges of the 160 MHz clock received from the GBTxEMU, producing a 320 MHz 14-bit timestamp (`smx_tdc`).

4.4.3   Data selection near the trigger time

Figure 4.12 shows the clock axes for each component (SMX, GBTxEMU, GERI, UT3) and the timings of STS hits and triggers on their respective time axes.
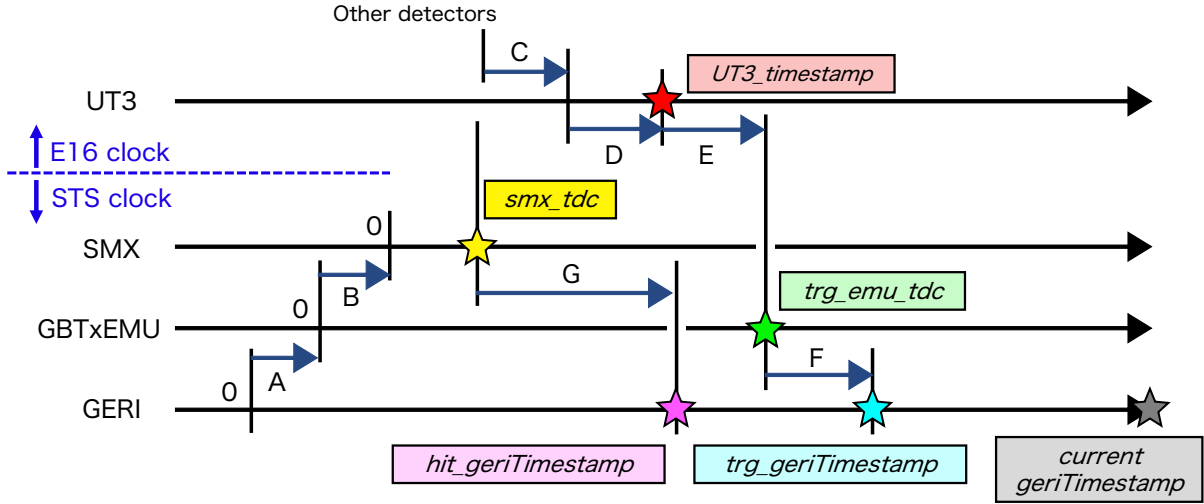

Figure 4.12: Illustration of time axes and event timing in the STS readout system.

The timestamps (stars) and their differences (the dark blue arrows) in Fig. 4.12, are as follows:

- ★ `UT3_timestamp`: The timestamp assigned to the trigger by UT3.

- ★ `trg_emu_tdc`: The GBTxEMU arrival time of the trigger data.

- ★ `trg_geriTimestamp`: The GERI arrival time of the trigger data.

- ★ `smx_tdc`: The SMX recording time of the hit data.

- ★ `hit_geriTimestamp`: The GERI arrival time of the hit data.

- ★ `current_geriTimestamp`: The current timestamp of GERI clock.

A: The time synchronization difference (path length + processing time).

B: The time synchronization difference (path length + processing time).

C: The time difference until data from other detectors arrives at UT3.

D: UT3 processing time.

E: The time difference from when the trigger timestamp is added by UT3 to when it arrives at GBTxEMU.

F: The time difference from when the trigger data arrives at GBTxEMU to when it arrives at GERI.

G: The time difference from when SMX attaches a timestamp to when it arrives at GERI.

Except for G, all other timestamp relationships have fixed latencies. Only G depends on the hit rate due to the buffer inside the SMX, where it may take anywhere from a few µsec to a few tens of µsec for data to be output from the SMX. Since the `UT3_timestamp` ★ is assigned using the E16DAQ clock, which is not synchronized with the STS clock, it cannot be used for online trigger selection. Additionally, although not shown in this figure, the arrival time of hit data at the GBTxEMU cannot be recorded due to limitations in data bandwidth between the GBTxEMU to the GERI.

For these reasons, online trigger selection is performed in two steps: a "coarse selection" using `trg_geriTimestamp` ☆ and `hit_geriTimestamp` ☆, and a "fine selection" using `trg_geriTimestamp` ☆ and `smx_tdc` ☆. Coarse selection is performed with a window width of a few µsec to several tens of sec, while fine selection is performed within a window width of 100 nsec to a few nsec. For details, see Appendix D.

This selection allows the acquisition of hit data near the trigger. Chapter 6 reports on the selection results from Run-0e data.

4.5   Installation in the experimental area

The STS chambers were installed in the E16 experiment for the first time during the commissioning run (Run-0d) conducted in June 2023. Figure 4.13 shows the installation of the chambers during Run-0e. To avoid interference with the beam pipe, which has a diameter of 300 mm, FFC-Ether adapters are supported by aluminum frame pillars.
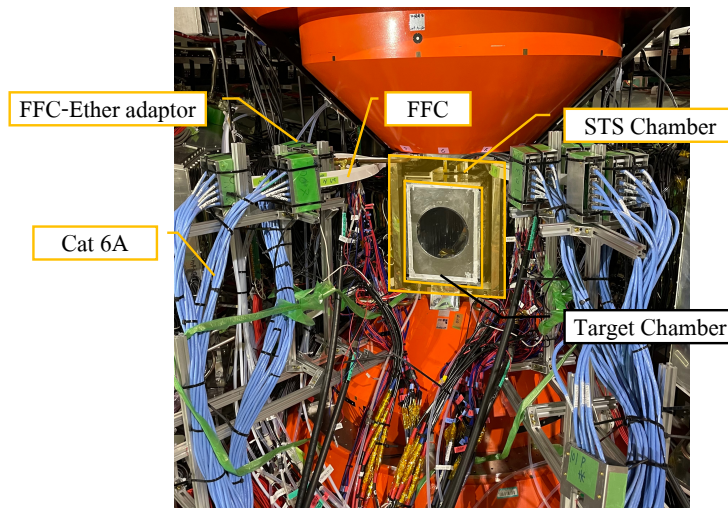

Figure 4.13: J-PARC E16 STS install at Run-0e.

The LVDS repeaters are installed under the stage in front of the FM magnet, where they amplify signals sent through 5-m Cat6a cables from the FFC-Ether adapters. Ferrite cores are attached to

the cables just before the input to suppress noise. The GBTxEMUs are positioned away from the FM magnet and the beam pipe.

4.6   Implementation of the power operation and monitoring system

The FEB-8 operates on two channels of low voltage (LV) at approximately 3 V, while the sensor itself requires a symmetric reverse bias voltage (HV) applied to both sides. Thus, operating a single sensor requires LV: 2×2 (for both sides) ch + HV: 2 ch = 6 channels. Additionally, power supplies are required for the GBT and repeater. Managing power for 10 sensors involves nearly 70 channels.

To operate these systems, it is necessary to link channel numbers with sensor names and device names. However, expecting shifters to memorize and manually operate these channel numbers is both challenging and risky. To address this, I developed a GUI from scratch using Python's "Tkinter" library, enabling operations via SNMP[3] communication commands. Figure 4.14 shows the block representing a sensor in this GUI. This GUI is an improved version, refined after the test experiments at the KEK PF-AR. During Run-0e, this GUI was used for power operations.

For monitoring and logging, "Prometheus" and "Grafana", which are also used by other E16 detectors, was utilized during Run-0e. However, alert settings were not implemented, making it one of the tasks planned for implementation before Run-1.
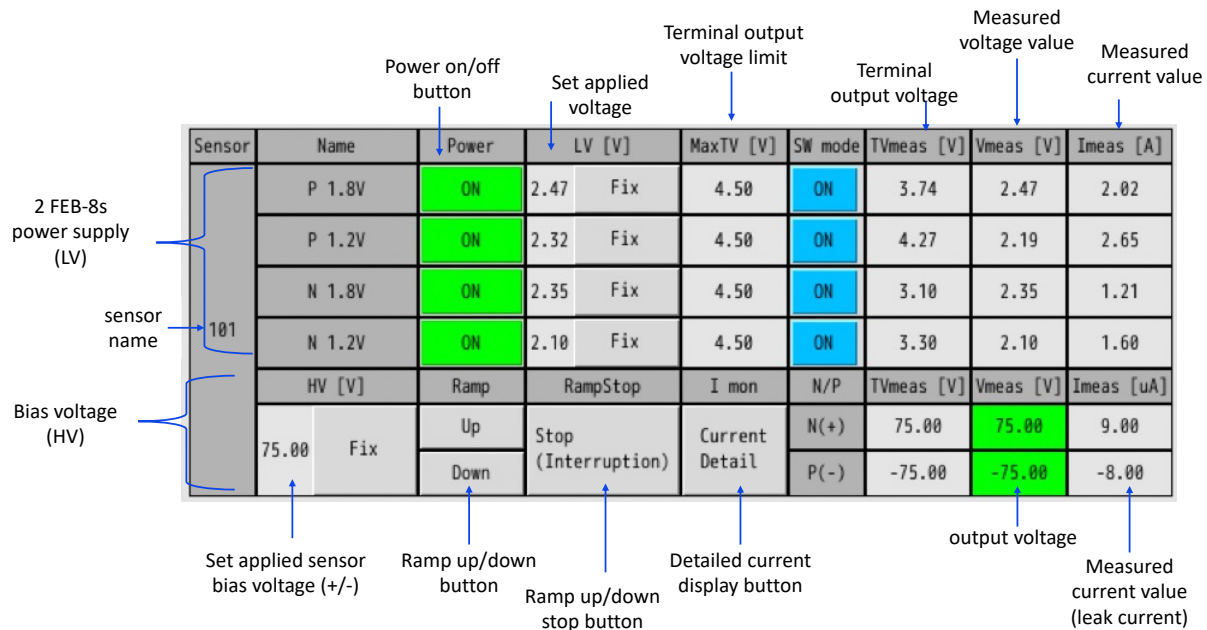

Figure 4.14: Created power operation GUI (block for one sensor). In the actual experiment, this block is replicated 10 times, with additional blocks for the GBT and repeater included on the same screen for centralized management. These displays are updated in real time every second.

---

[3]SNMP (Simple Network Management Protocol) is a communication protocol used to monitor and manage devices on a network, such as routers, switches, and servers. It allows for retrieving status information from devices and modifying their settings.

Chapter 5

Test at the KEK PF-AR test beamline

We conducted test experiments using an electron beam at the KEK PF-AR detector test beamline from November 17 to 21, 2023, to evaluate the performance of the sensor and E16 STS DAQ system.

5.1 Purpose

The purposes of this test experiment are as follows:

1. Performance evaluation of the sensor.

2. Performance evaluation of the E16 STS streaming DAQ system using an electron beam.

5.2 KEK PF-AR and detector test beamline

The PF-AR (Photon Factory Advanced Ring) is an electron storage ring located on the Tsukuba campus of KEK. It is part of the synchrotron radiation experimental facility known as the Photon Factory (PF). This high-energy accelerator primarily generates synchrotron radiation in the hard X-ray region, supporting a wide range of research fields, including materials science and life sciences [44].
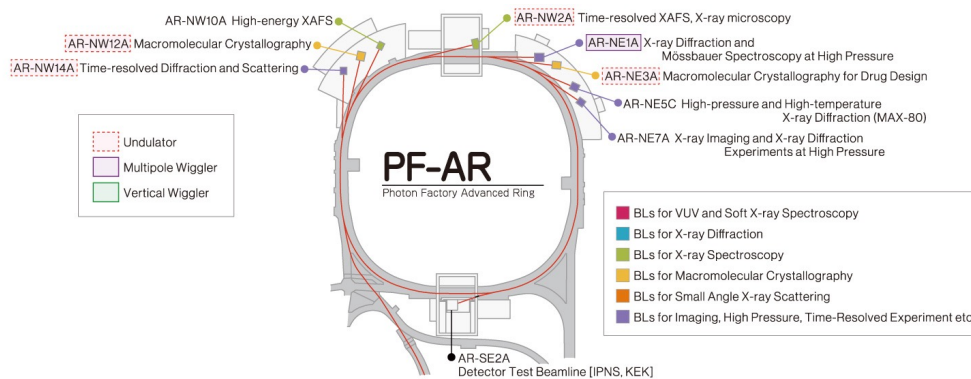

Figure 5.1: The top view of the PF-AR and its beamlines. The test beamline for detector test is shown at the bottom of the diagram, labeled as "AR-SE2A" [44].

The PF-AR was constructed by modifying the injector accelerator of "TRISTAN", which was used for top quark searches, and repurposed as a dedicated synchrotron light source. Table 5.1 summarizes the various parameters of the PF-AR. The PF-AR has a circumference of 377 m and operates as a single-bunch electron storage ring with an electron beam energy of 6.5 GeV (or 5.0 GeV) and a revolution period of 1.257 μsec. This enables the generation of high-intensity, high-energy synchrotron radiation, contributing to advanced research such as material microstructure analysis and the observation of fast phenomena [45].

Table 5.1: Basic specifications of PF-AR [45].

Parameter	Value
Beam energy	6.5 GeV / 5.0 GeV
Circumference	377 m
Initial current	60 mA
Emittance	293 nm rad
Number of bunches	1

As shown in Figure 5.1 the PF-AR is equipped with a total of eight synchrotron radiation beamlines, located on the northeastern and northwestern synchrotron radiation experimental floors and in the North Experimental Hall. In contrast, no synchrotron radiation beamlines are installed on the southern half of the accelerator. The PF-AR detector test beamline was constructed by effectively utilizing the unused space in the AR South Experimental Hall.

Figure 5.2 shows the vicinity of the test beam source within the storage ring in the accelerator tunnel and the arrangement of magnets along the test beamline, which extends through the concrete shielding into the AR South Experimental Hall.
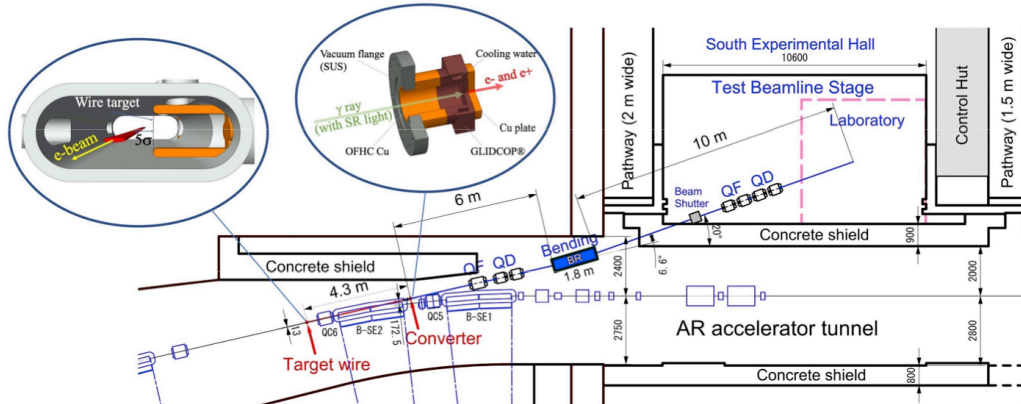

Figure 5.2: Overall layout of the PF-AR detector test beamline and perspective views of the wire target and the copper converter [46].

In this beamline, a wire target is installed in the storage ring to scrape the beam halo and generate photons. These photons are directed onto a copper converter, where electron-positron pairs are produced. The electron beam is then guided to the detector test area using an array of extraction magnets consisting of dipole and quadrupole magnets [46].

A beam with a maximum momentum of 5 GeV/c can be extracted, and the beam size at 1 m from the extraction point is $\sigma \simeq 8$ mm (x- and y-axes). Figure 5.3 shows a plot of the z-dependence of the

beam profile derived from measurements of a $3.0\,\mathrm{GeV}/c$ momentum beam [47]. In the experimental setup, QSF=16.19 A was used.

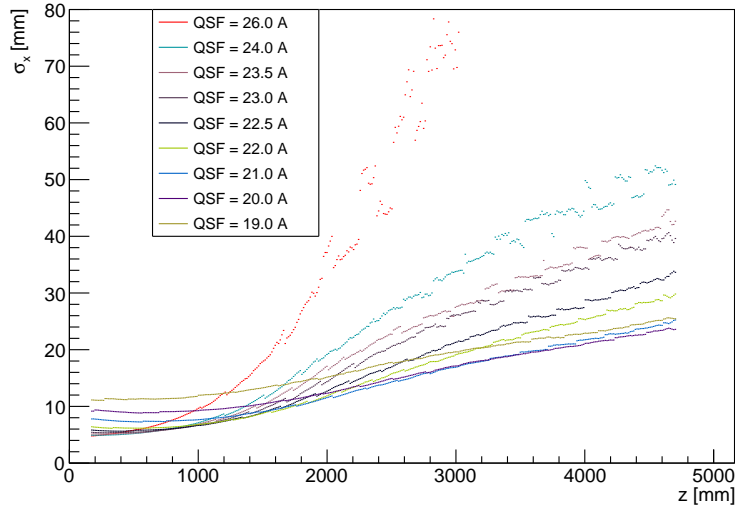Figure 5.3: The z-dependence of the beam profile. Using a magnet setting of AR $= 5.0\,\mathrm{GeV}$ and p $= 3.0\,\mathrm{GeV}$, the current of the QSF magnet was varied while tracking hit information from two jet chambers. The hit map was projected onto the x-axes, and the resulting σ values were obtained by fitting the distributions with a Gaussian function. z=0 is the extraction point [47].

5.3   Setup

In this test experiment, we used the actual E16 STS chamber. The readout chain was also nearly the final setup. The following sections provide detailed descriptions of the geometrical setup and the DAQ configuration.

5.3.1   Geometrical setup

Four scintillators, each with a size of $10 \times 10\,\mathrm{mm}^2$, were arranged to sandwich the STS chamber. Two scintillators were positioned crosswise in front of the chamber, while the other two were placed at the back. The setup was designed to evaluate a small spot on the sensor. The sensors were positioned approximately $3\,\mathrm{m}$ from the beam extraction point, with a distance of $1.5\,\mathrm{m}$ between the two sets of scintillators (S1 and S2) (Figure 5.4). The scintillator irradiation position and the central position of the beam were nearly aligned with the center of the sensor.

Specifically, the test was conducted using a single sensor (108) and a setup with three sensors. Figure 5.5 shows the top view of each setup.

- Setup A: Configuration where the beam is incident at 0 degrees to module 108.
- Setup B: Configuration where the beam is incident at 16 degrees to module 108.

- Setup C: Configuration using three sensors (modules 104, 107, and 108), where the beam is incident at 39 degrees to module 108.

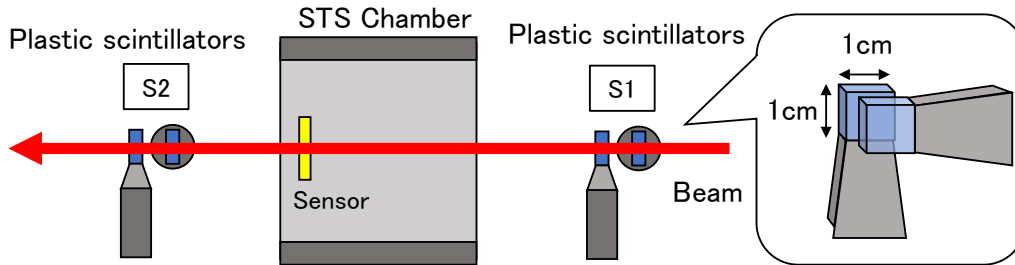The beam momentum was $3.0 \, \mathrm{GeV}/c$ for all setups.

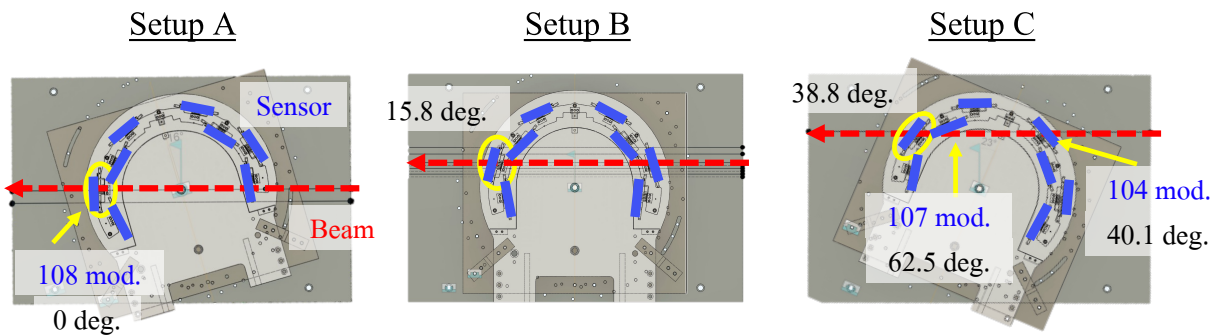Figure 5.4: Setup of STS chameber and scintillators.

Figure 5.5: Top view of each setup.

5.3.2   Readout chain

The readout chain was tested in a configuration that closely resembled the final setup. However, at this stage, the development of the E16 trigger acquisition system was not yet complete, and therefore, data acquisition using the trigger was not conducted. Instead, a standalone FEB-8, not connected to the sensor, was prepared, and coincidence signals from the scintillators were input into this FEB to record the signals (Figure 5.6).

Additionally, two types of timestamps were used in the following analysis: the SMX-recorded timestamp (smx_tdc), and the GERI-recorded timestamp (geriTimestamp).
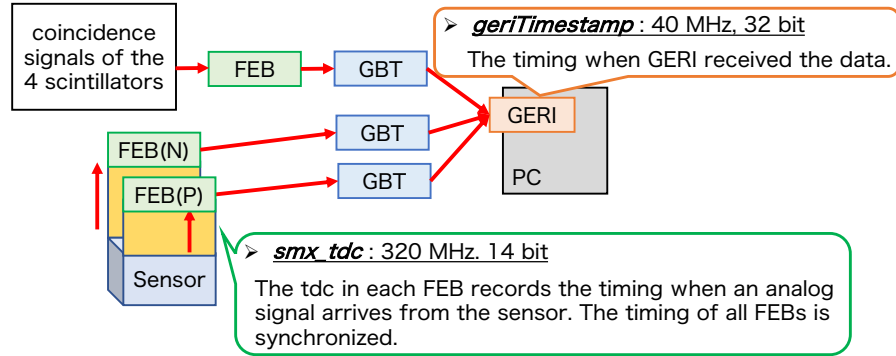
Figure 5.6: Readout chain of the test experiment.

5.4   Analysis and results

Setup C was designed to allow electrons to pass through three sensors for position resolution measurements. However, due to the steep incident angle and threshold effects (Section 5.5.2), the detection efficiency was low. Consequently, there was insufficient data for a detailed analysis. This report focuses on the results from the 108 N-side.

5.4.1   Threshold

During the test experiment, the TDC threshold settings were higher than the lowest ADC threshold, while the former should be set sufficiently lower than the latter not to loose efficiency (Section 2.2.3). Figure 5.7 shows the lowest ADC thresholds (hit thresholds) and TDC thresholds for the 108 N-side in each setup. These thresholds were calculated after the experiment using the calibration scan results (Appendix C.1).

(a) Setup A: 0 deg.   (b) Setup B: 16 deg.   (c) Setup C: 39 deg.
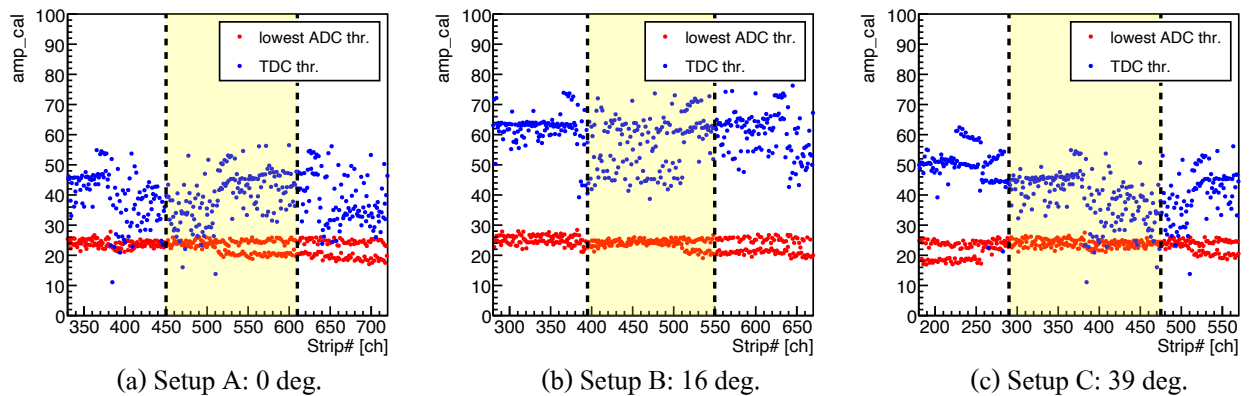
Figure 5.7: The lowest ADC thresholds (red) and TDC thresholds (blue) at the scintillator-constrained positions (yellow areas) on the 108 N-side. It can be observed that the TDC thresholds exhibit significant channel dependence. For reference, $1\,\mathrm{amp\_cal} = 0.056\,\mathrm{fC}$. The lowest ADC thresholds are approximately $1.4\,\mathrm{fC}$ across all setups. The average TDC thresholds are approximately $2.4\,\mathrm{fC}$ in setups A and C, and $3.0\,\mathrm{fC}$ in setup B.

The light yellow areas represent regions constrained by the scintillators. The lowest ADC thresholds were relatively uniform with minimal channel dependence, while the TDC thresholds exhibited significant channel dependence and were not set lower than the lowest ADC thresholds. Ideally, the TDC thresholds should be set sufficiently lower than the lowest ADC thresholds (Section 2.2.3). Additionally, in Setup B, which had a 16 degree incident angle, the TDC thresholds were set even higher. Considering these factors, the following results are presented.

5.4.2   Event selection

Figure 5.8 shows a histogram of the beam rate time structure reconstructed from the `geriTimestamp` of the scintillator coincidence signals. The histogram, with a bin width of one second, visualizes the beam rate characteristics. The beam rate remained stable at approximately 30 Hz for about 30 to 50 seconds, followed by a transient spike to around 200 kHz for 10 seconds, exhibiting an unusual pattern. This phenomenon is believed to result from beam injections occurring at intervals of roughly 30 seconds, although not perfectly periodic.

To ensure the accuracy of the analysis, data from the unstable beam rate region were excluded, and only the stable 30 Hz beam rate period was used
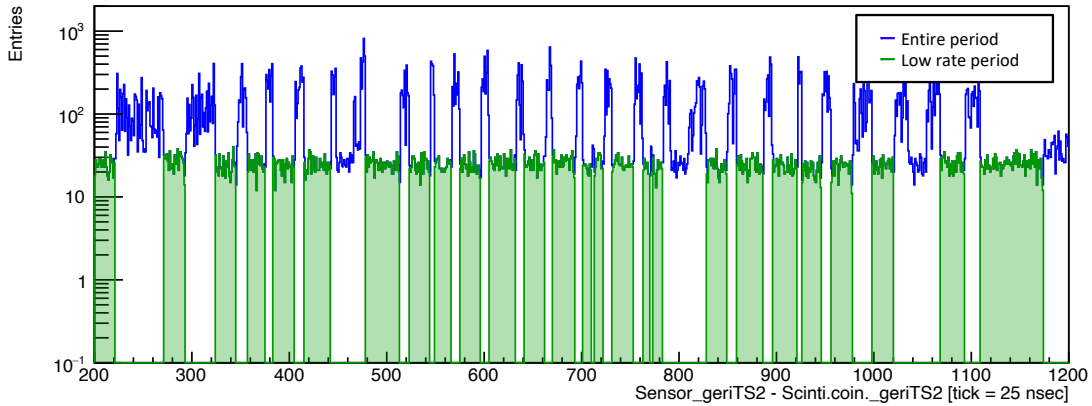

Figure 5.8: The time distribution (`geriTimestamp2`: 40 MHz, 64-bit) of the scintillator coincidence signals, reconstructed using `geriTimestamp`. Blue represents the entire period, while green represents the selected period.

Figure 5.9 shows the distribution of the difference between the scintillator coincidence signal and the `geriTimestamp2` (40 MHz, 64-bit, reconstructed from `geriTimestamp`) hits on the 108 N-side. A prominent peak is observed near 0, along with smaller peaks occurring every 50 ticks $\simeq 1.25\,\mu$sec. The peak near 0 is considered to represent the hits from the actual events of interest. TThe smaller peaks are likely hits that accidentally coincide with the scintillator signals from different beam cycle of PF-AR ring, considering that the PF-AR operates in a single-bunch mode with a revolution period of 1.257 μsec. To extract the peak near 0, the interval from -20 ticks to +40 ticks (1.5 μsec) was selected (The red-shaded area in Fig 5.9. Hereafter referred to as "`geriTimestamp` cut").

(a) Setup A: 0 deg.   (b) Setup B: 16 deg.   (c) Setup C: 39 deg.
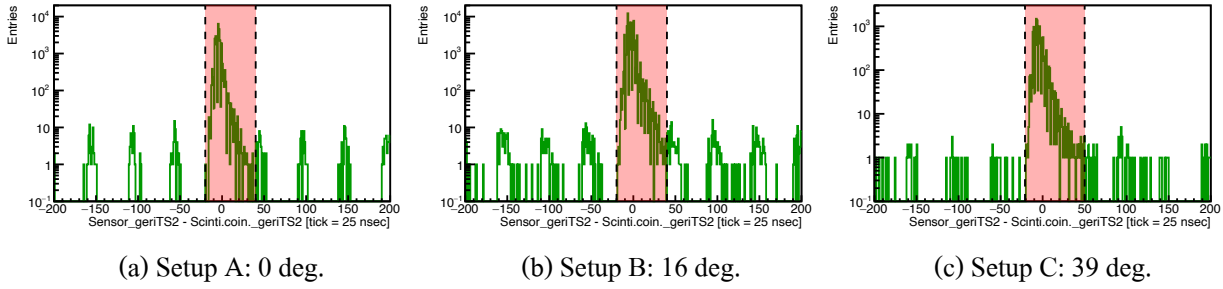
Figure 5.9: The `geriTimestamp2` difference between sensor hits and the scintillator coincidence signals in each setup. The red-shaded area is selected range, "`geriTimestamp cut`".

5.4.3   Hit profile

Based on the selected range in Fig. 5.8 and 5.9 from the previous section, the hit profile of sensor hits on the 108 N-side is shown in the upper panel of Figure 5.10. The green corresponds to the green selection range in Fig. 5.8 and 5.9 , while the red corresponds to the "`geriTimestamp cut`". This profile shows that the hit distribution aligns with the positions constrained by the scintillators, demonstrating that event selection based on the time structure is possible. Therefore, it can be concluded that our DAQ system is functioning successfully.
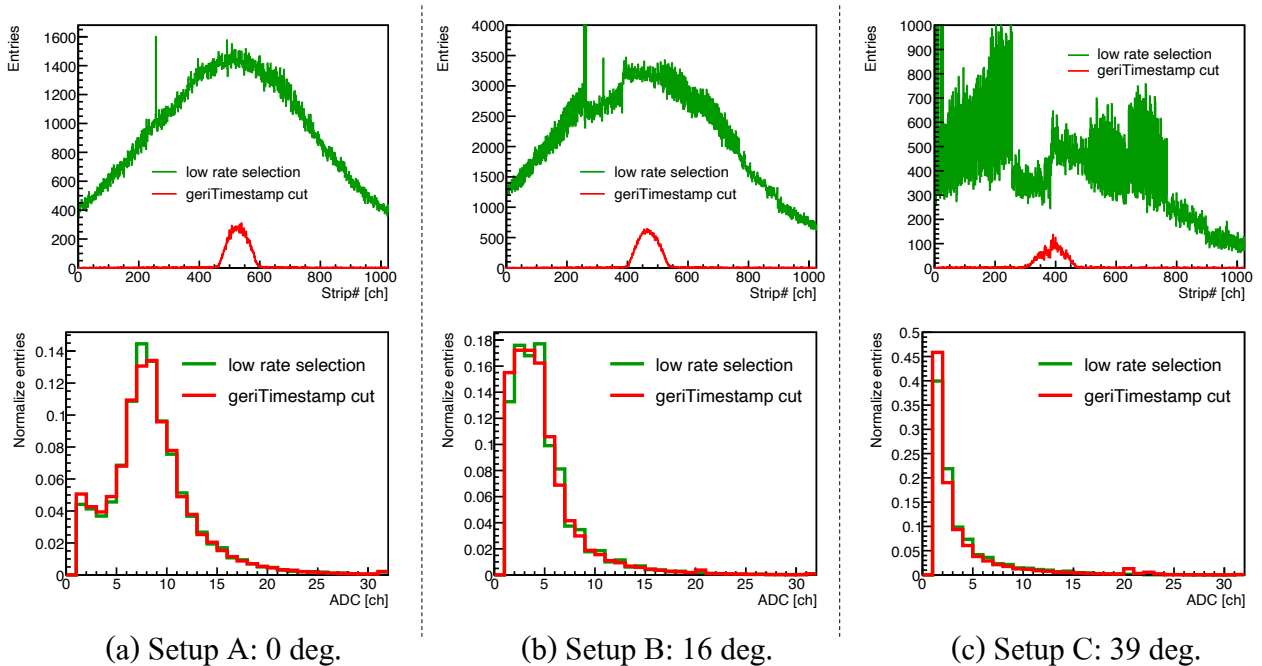

(a) Setup A: 0 deg.   (b) Setup B: 16 deg.   (c) Setup C: 39 deg.

Figure 5.10: Hit profiles (upper) and normalized adc distributions (lower) of the 108 N-side in each setup. Note: $1\,\mathrm{strip}=58\,\mu\mathrm{m}$, $1024\,\mathrm{strip\_ch} = 60\,\mathrm{mm}$.

Furthermore, the green plot, which does not apply the scintillator coincidence signal, represents

the beam profile. Considering Fig. 5.3 and the fact that the sensor is located approximately three meters from the beam extraction point, this profile appears reasonable.

The lower panel of Fig. 5.10 shows the normalized ADC distributions for the green and red regions overlaid. This indicates that the shape of the distribution remains unchanged regardless of whether the scintillator coincidence signal is applied, suggesting that noise components are minimal.

5.4.4   Time resolution

The time resolution of the sensor, σ_{sensor}, can be expressed using the time resolution of the scintillator, $\sigma_{\mathrm{scint.}}$, and the time difference between the scintillator coincidence signal and the sensor hit, $\sigma_{\mathrm{diff.}}$, as shown in the following equation:

$$\sigma_{\mathrm{diff.}} = \sqrt{\sigma_{\mathrm{scinti.}}^2 + \sigma_{\mathrm{sensor}}^2},$$
$$\therefore \sigma_{\mathrm{sensor}} = \sqrt{\sigma_{\mathrm{diff.}}^2 - \sigma_{\mathrm{scinti.}}^2}. \tag{5.1}$$

Since one tick of the `smx_tdc` corresponds to 3.125 nsec, and the scintillator's time resolution is on the order of less than 1 nsec, the following approximation can be made:

$$\therefore \sigma_{\mathrm{sensor}} \simeq \sigma_{\mathrm{diff.}} \tag{5.2}$$

Therefore, the time resolution was evaluated by analyzing the difference between the `smx_tdc` of the scintillator coincidence signal and the hits.

Figure,5.11 shows a histogram of the differences in `smx_tdc` values between the scintillator coincidence signal and the hits. In this analysis, the lower 10-bit of `smx_tdc` are used for the calculation. The hits used for this analysis are those after applying the "`geriTimestamp cut`". Sharp peaks are observed near 0 and around 1000. These peaks represent coincidence hits with the scintillator. The appearance of two peaks is explained by the fact that using `smx_tdc` is 10-bit, causing a wraparound every $3.125\,\mathrm{nsec} \times 2^{10} = 3.2\,\mathrm{\mu sec}$. Hereafter, these peaks will be referred to as peak① and peak②, respectively.

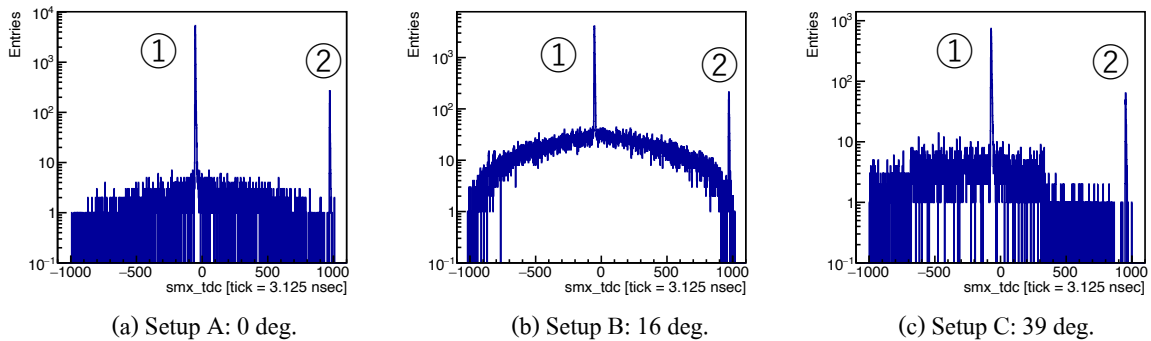(a) Setup A: 0 deg.   (b) Setup B: 16 deg.   (c) Setup C: 39 deg.

Figure 5.11: The lower 10-bit of `smx_tdc` difference between sensor hits and the scintillator coincidence signals in each setup. The peak positions are considered to represent coincidence hits. Due to the wraparound at 3.2 μs, two peaks (peak① and ②) are observed.

In Setup B, the TDC threshold was set significantly higher than the lowest ADC threshold (Fig. 5.7,(b)), resulting in many hits without accurate TDC recordings being distributed outside the peak positions.
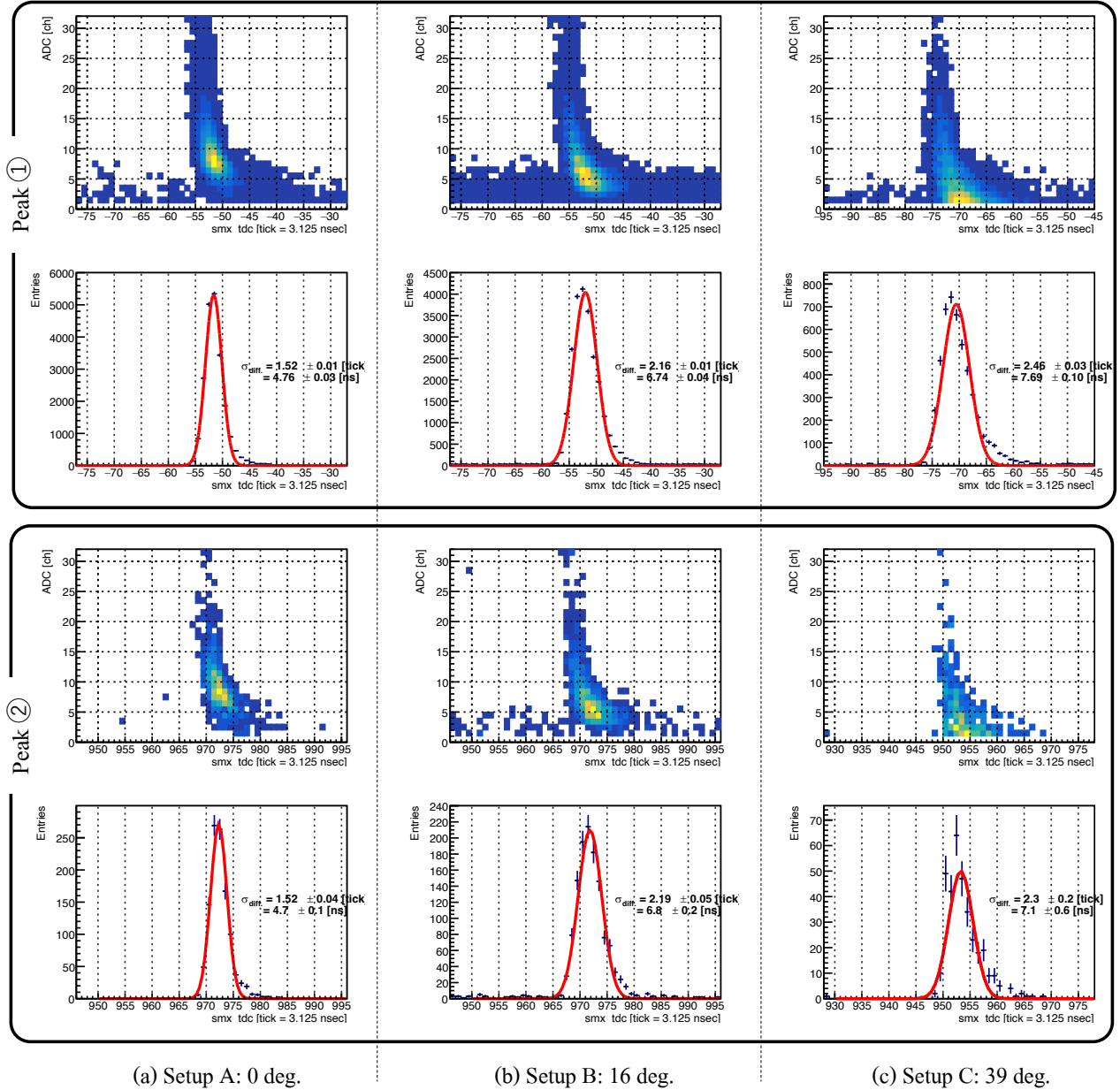

(a) Setup A: 0 deg.   (b) Setup B: 16 deg.   (c) Setup C: 39 deg.

Figure 5.12: The ADC distribution and smx_tdc difference 2D histograms (upper) and the Gaussian fit of the smx_tdc difference (lower) in each setup near the two peaks.

Figure 5.12 shows 2D histograms of ADC values on the vertical axis and `smx_tdc` differences on the horizontal axis for peak① and peak②. The projections onto the time-axis (X-axis) are fitted with Gaussian functions for each peak. From the results of the Gaussian fits, $\sigma_{\mathrm{diff.}} \simeq \sigma_{\mathrm{sensor}}$

60

was found to be approximately 4.8 nsec for Setup A (0 degrees), 6.8 nsec for Setup B (16 degrees), and 7.7 nsec for Setup C (39 degrees). However, examining the 2D histogram, including the ADC distribution, clearly shows that the fit does not adequately cover the regions with small ADC values. Therefore, time walk corrections were applied to further evaluate the time resolution.

Time walk corrections

Time walk refers to a phenomenon where variations in signal amplitude cause deviations in timing measurements. As shown in Figure 5.13, signals with smaller amplitudes take longer to reach the threshold, resulting in delayed timing. Conversely, signals with larger amplitudes reach the threshold more quickly, leading to earlier timing. Additionally, the time resolution is affected by the rise time of the signal. This phenomenon is clearly visible in the 2D histogram in Fig. 5.12.
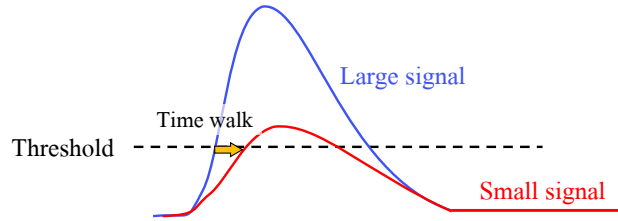

Figure 5.13: Time walk.

Figure 5.14 shows the ADC dependence of the mean (upper) and sigma (lower) values obtained by slicing the 2D histograms of peak① in Fig. 5.12 for each ADC value and fitting each slice with a Gaussian function. From this, it can be observed that both the mean and sigma tend to increase in regions with low ADC values. The red line represents a smooth fit applied to the mean plot using an appropriate fitting function: an exponential function for ADC < 10 ch and a composite function of exponential + linear for ADC ≥ 10 ch. This red line was used as the basis for the time walk corrections.

Figure 5.15 shows the results for peak① after the time walk correction. The upper part of Fig. 5.15 displays the 2D plot of the ADC and TDC distribution, while the lower part shows the TDC distribution along with its Gaussian fit. From the upper plot in Fig. 5.15, it can be seen that the ADC-dependent mean shifts observed in Fig. 5.12 have been corrected. Based on the Gaussian fit results, $\sigma_{\mathrm{diff.}} \simeq \sigma_{\mathrm{sensor}}$ was determined to be approximately 4.3 nsec for Setup A (0 degrees), 5.4 nsec for Setup B (16 degrees), and 7.6 nsec for Setup C (39 degrees).
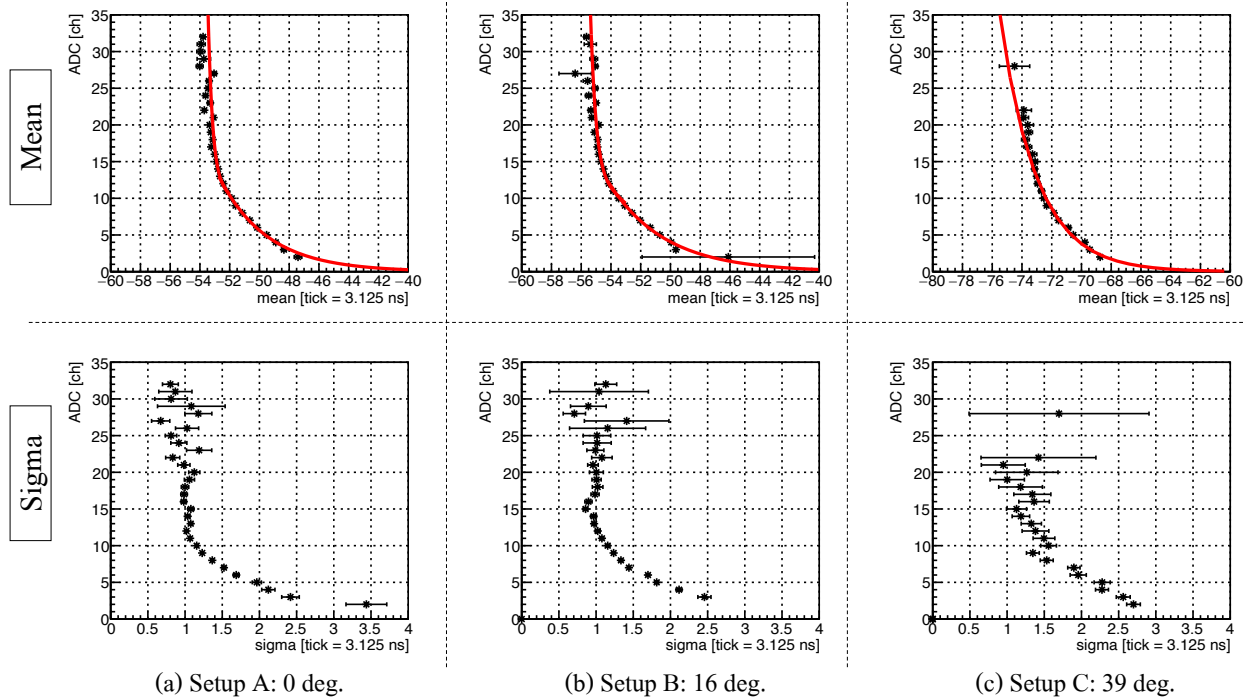
Figure 5.14: The ADC dependence of the mean (upper) and sigma (lower) values for the `smx_tdc` difference (peak①). The red line in the mean plot represents an appropriate fitting function: an exponential function for ADC < 10 ch and a composite function of exponential + linear for ADC ≥ 10 ch.
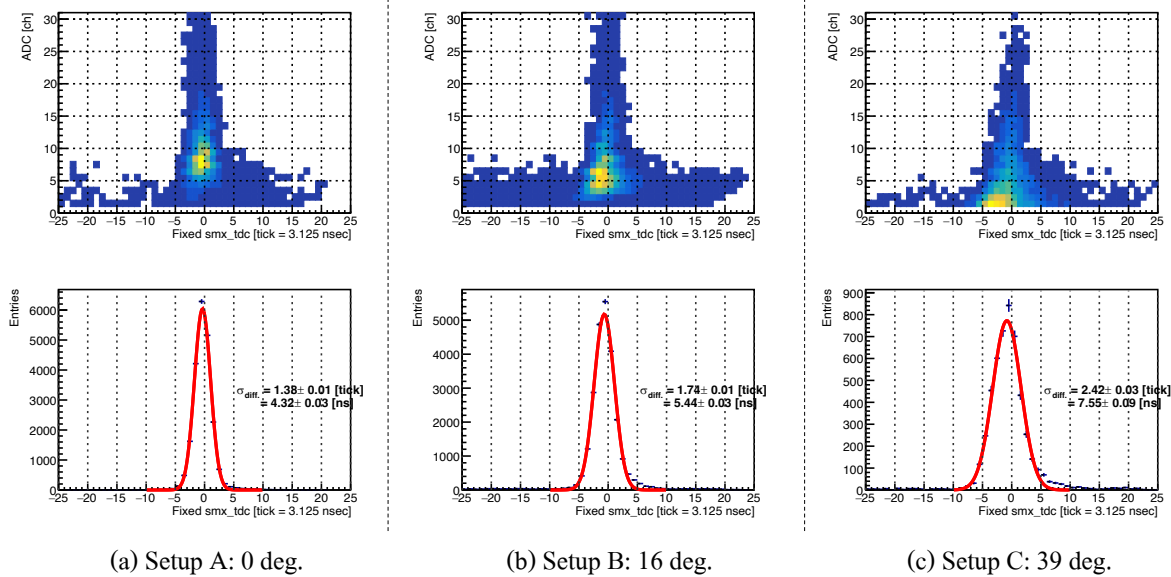

Figure 5.15: The 2D histogram of ADC distribution and the smx_tdc difference (upper), and the Gaussian fit of the `smx_tdc` difference (lower), for each setup after time walk corrections (peak①).

5.4.5 Detection efficiency

The detection efficiency was calculated as follows:

$$\text{Efficiency} = \frac{\begin{array}{c}\text{The number of sensor response events corresponding to}\\\text{the scintillator coincidence signals}\end{array}}{\text{The number of scintillator coincidence signals}} \qquad (5.3)$$

Sensor response events, in other words, refer to cases where a given scintillator coincidence signal resulted in the sensor recording at least one hit. The detection efficiency was then calculated based on this criterion.

Coincidence hits were selected using "`geriTimestamp cut`" as shown in Fig. 5.9. However, as discussed in the previous section, the selection should ideally be performed using `smx_tdc`. Figure 5.16 shows the two peaks from Figure 5.11 plotted on a log scale for the vertical axis. The blue shaded regions in Figure 5.16 were defined as the coincidence hits, and the selection was performed accordingly. Hereafter, this cut will be referred to as "`smxtdc cut`"(Note that this cut includes the "`geriTimestamp cut`").
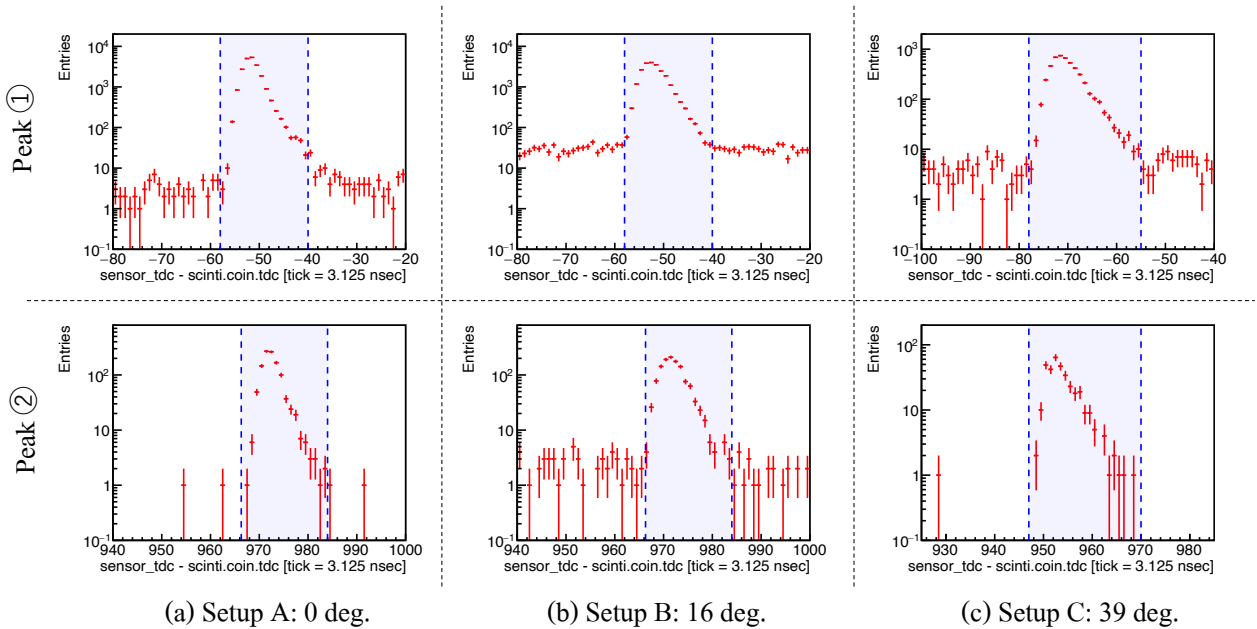

Figure 5.16: Timing distribution and `smxtdc cut` range (blue shaded area).

The upper panel of Figure 5.17 overlays the hit profiles after the `geriTimestamp cut` and `smxtdc cut`. The dashed line represents the geometrical acceptance. The lower panel of Fig. 5.17 shows the ADC distributions for each cut. From this, it can be observed that, in all setups, the `smxtdc cut` excludes hits with low ADC values. As discussed in Section 5.4.1, this is because the TDC threshold was set higher than the ADC threshold. In particular, for Setup B, the large difference between these thresholds results in hits being missed down to around ADC = 7 ch. Examining the hit profiles confirms that the smxtdc_cut does not merely remove backgrounds but also excludes genuine hits.

The calculated detection efficiencies are shown in Table 5.2. The geometrical acceptance was determined using the dashed lines in the hit profiles shown in Fig. 5.17. The background in the third and fourth rows represents the estimated background events within the geometrical acceptance. This estimation is based on the number of events outside the geometrical acceptance and the beam profile (green) shown in Fig. 5.10 (Figure 5.18). The errors were calculated using the Clopper-Pearson interval [48].

As a result, when considering the backgrounds, the detection efficiencies with the `geriTimestamp cut` were 98.6% for Setup A, 98.5% for Setup B, and 57.6% for Setup C. The reduced detection efficiency across all setups when using the `smxtdc cut` is likely due to the impact of the higher threshold settings.
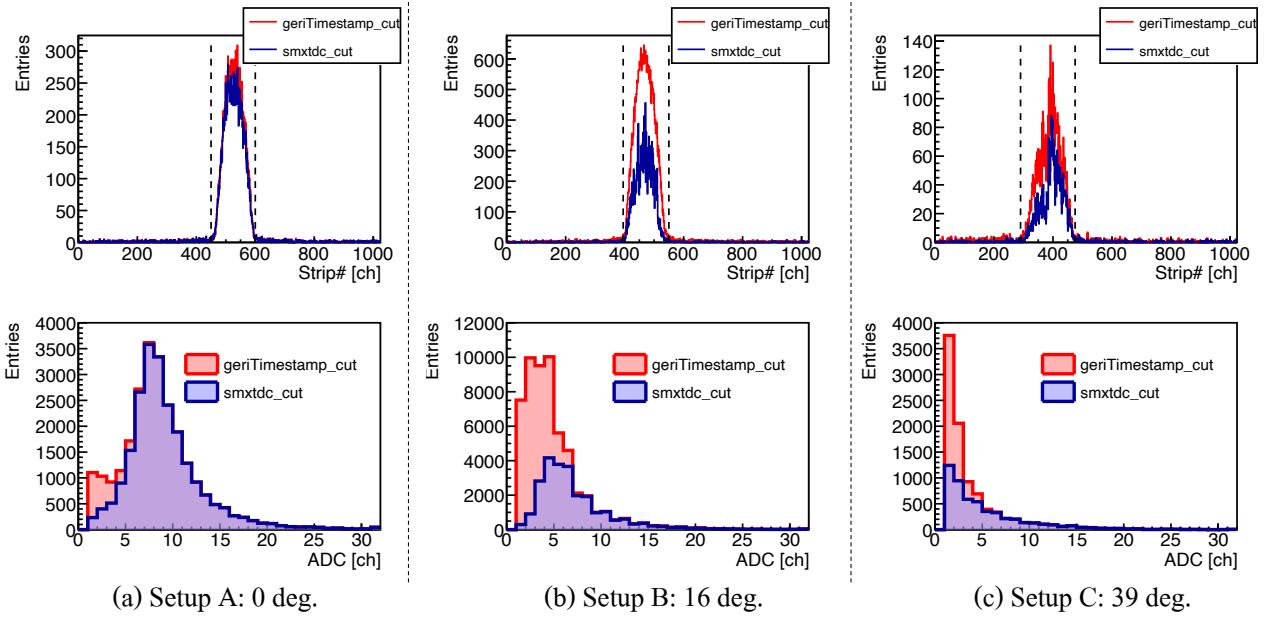

(a) Setup A: 0 deg.   (b) Setup B: 16 deg.   (c) Setup C: 39 deg.

Figure 5.17: The hit profiles (upper) and ADC distributions (lower) for the `geriTimestamp cut` (red) and `smxtdc cut` (blue) in each setup.

Table 5.2: Detection efficiency in each setup. ("GC"= geometrical cut, "BG"= background)

Types of cuts	Setup A (0°)	Setup B (16°)	Setup C (39°)
`geriTimestamp cut` + GC	$99.85^{+0.03}_{-0.03}\%$	$99.78^{+0.03}_{-0.03}\%$	$59.9^{+0.5}_{-0.5}\%$
`smxtdc cut` + GC	$96.1^{+0.1}_{-0.1}\%$	$60.0^{+0.3}_{-0.3}\%$	$37.2^{+0.5}_{-0.5}\%$
BG (`geriTimestamp cut` + GC)	$1.23^{+0.08}_{-0.08}\%$	$1.28^{+0.07}_{-0.06}\%$	$2.3^{+0.2}_{-0.2}\%$
BG (`smxtdc cut` + GC)	$1.12^{+0.08}_{-0.07}\%$	$0.54^{+0.04}_{-0.04}\%$	$0.67^{+0.10}_{-0.09}\%$

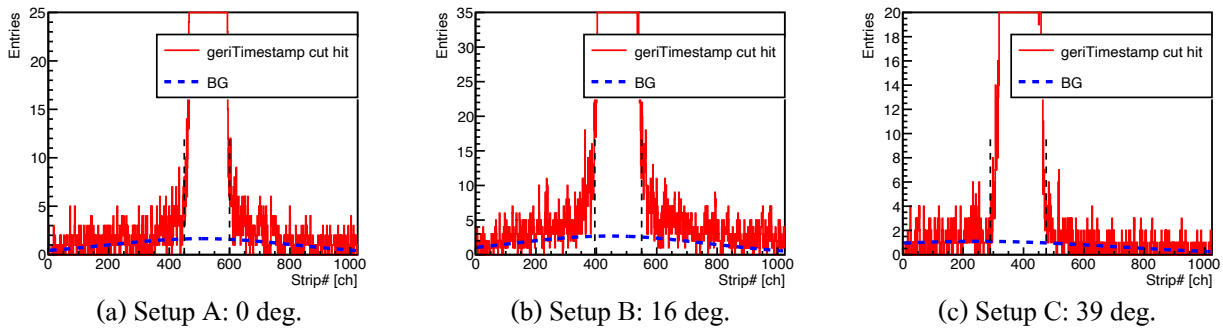| (a) Setup A: 0 deg. | (b) Setup B: 16 deg. | (c) Setup C: 39 deg. |

Figure 5.18: The hit distribution after the `geriTimestamp cut` (red), the beam profile (Fig. 5.10, green), and the estimated background (BG) from the number of events outside the geometrical acceptance (blue dashed line). *Note: There is not necessarily one hit per event.*

5.4.6   Cluster size and charge

When the incident angle increases, charge sharing between strips becomes more significant. A cluster is a group of adjacent hits combined together. In cases where charge sharing occurs between strips, this clustering allows for a more accurate representation of the signal along a charged particle's tracks. In general, the size of a cluster is represented by the number of strips that registered hits, referred to as the "cluster size" (Figure 5.19).
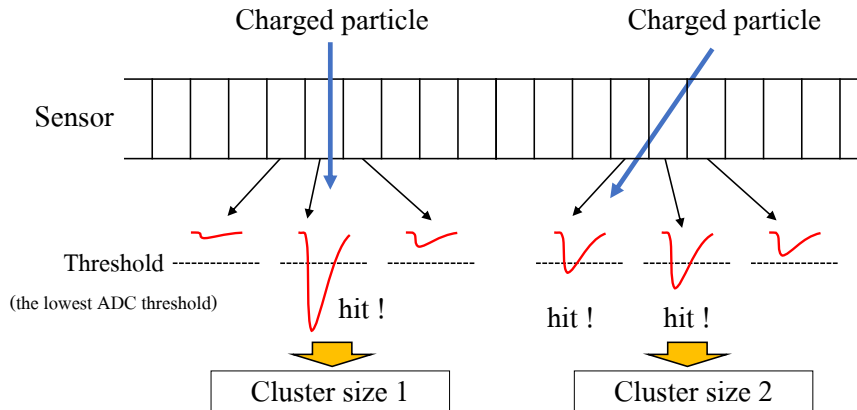

Figure 5.19: cluster

Figure 5.20 shows the cluster size distributions for each setup. The upper panels (red hist) of Fig. 5.20 use hits selected with the `geriTimestamp cut` + geometrical cut, while the lower panels (blue hist) use hits selected with the `smxtdc cut` + geometrical cut to form the clusters. The distributions for Setups A and C show little difference between clusters formed using hits selected with the `geriTimestamp cut` and those selected with the `smxtdc cut`. However, in Setup B, there are more clusters with a size of 2 when using hits selected with the `geriTimestamp cut` only.

Figure 5.21 shows the distribution of cluster charges, which is the sum of the charges of all hits within a cluster. The upper panels of Figure 5.21 show the ADC distributions, while the lower panels

show the distributions converted into the actual charges deposited on the strips. This conversion was performed based on the results of the threshold scan (Appendix C.1). In Setup A, there is little difference in both the ADC distribution and the charge distribution. In Setup C, low values in both the ADC and charge distributions are significantly reduced by the "smxtdc cut". Furthermore, in Setup B, the entire peak of the ADC distribution is substantially reduced by the "smxtdc cut". Additionally, in the charge distribution, two peaks are observed in the clusters formed using only the "geriTimestamp cut".

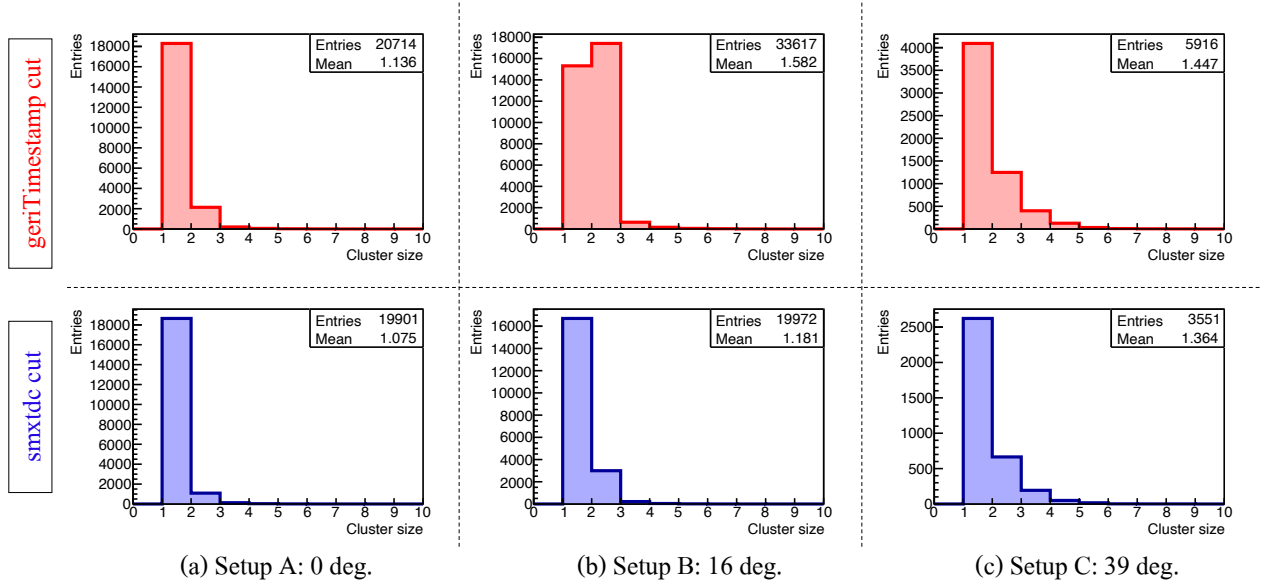(a) Setup A: 0 deg.   (b) Setup B: 16 deg.   (c) Setup C: 39 deg.

Figure 5.20: Cluster size distributions in each setup.

Figure 5.22 shows the cluster charge distributions (from the lower panel of Fig. 5.21) plotted for each cluster size. The upper panels show clusters selected with the "geriTimestamp_cut" only, while the lower panels show clusters selected with the "smxtdc_cut". The orange indicates cluster charges for clusters of size one, and the green indicates cluster charges for clusters of size two or larger. From this, it can be concluded that the two peaks in the red curve in the middle-lower panel of Fig.,5.21 are due to differences in cluster size. Comparing the upper and lower distributions for Setup B in Fig. 5.22, it is clear that the peak corresponding to cluster sizes of two or larger disappears after the smxtdc_cut. This indicates that charge shared between strips is either misidentified as cluster size one or not detected at all due to the high threshold.
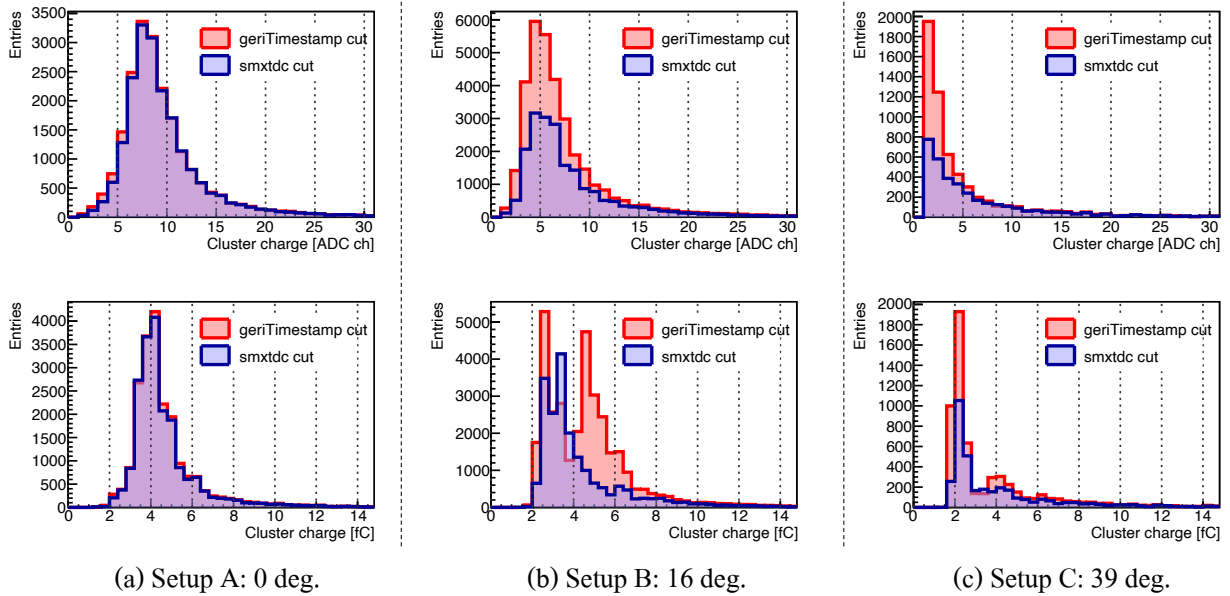
(a) Setup A: 0 deg.   (b) Setup B: 16 deg.   (c) Setup C: 39 deg.

Figure 5.21: Cluster ADC distributions in each setup.

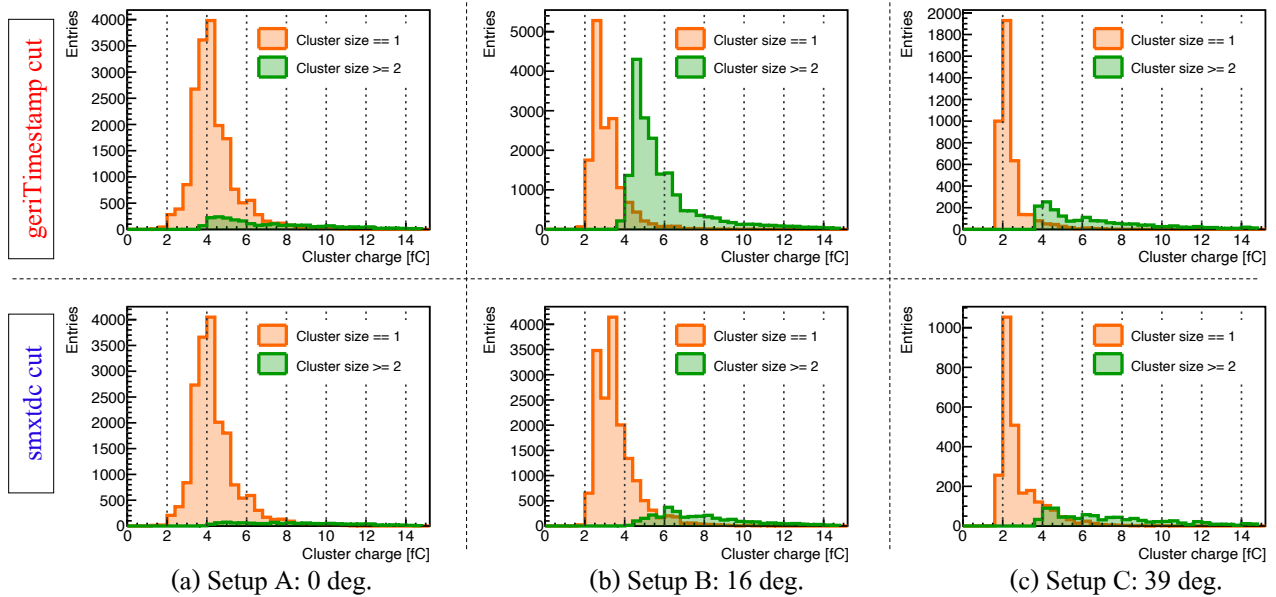(a) Setup A: 0 deg.   (b) Setup B: 16 deg.   (c) Setup C: 39 deg.

Figure 5.22: Cluster charge distributions for each setup and cluster size.

5.5   Discussions

5.5.1   Time resolution

In the analysis of time resolution, applying time walk corrections resulted in a time resolution of 4.3 nsec at an incident angle of 0 degrees and 5.4 nsec at 16 degrees, fully meeting the performance requirements of CBM and E16 experiments. At a larger incident angle of 39 degrees, the time resolution increased to 7.6 nsec. However, it is expected that this resolution can be improved by determining the timing using the cluster centroid calculation, as explained in Section 6.2.1. In this analysis, due to threshold settings, accurate `smx_tdc` values could not be recorded for some hits, and therefore, the evaluation using cluster centroid calculations was not performed.

5.5.2   Detection efficiency

To understand of detection efficiency, a simple simulation was performed using Garfield++ as follows. A silicon sensor with the same geometry as the actual sensor (strip pitch: 58 μm, thickness: 320 μm) was modeled, and electrons with a momentum of 3.0 GeV/c were injected at varying incident angles. The electric field was set to a linear field of 150 V/320 μm, similar to the actual detector. Detector noise and diffusion effects were neglected. A total of 20 strips were simulated, and the hit threshold (referred to here as the lowest ADC threshold) was varied to calculate the detection efficiency using the same method as in Equation (5.3).

Figure 5.23 shows the simulation results. The plots include the three incident angles used in the experiment and the maximum incident angle of 30 degrees under the E16 experimental conditions. The lowest ADC threshold and the TDC threshold used in the test experiment are annotated on the plot. Note that the TDC threshold is plotted as a range due to its significant channel dependence.

As the electron's incident angle increases, the curve in the plot shifts to the left. This is because a larger incident angle causes more charge sharing between strips, distributing the charge across multiple strips rather than concentrating it on a single strip

In comparison with the actual data, the detection efficiency with the "`geriTimestamp cut`" corresponds to the efficiency at the lowest ADC threshold, while the "`smxtdc cut`" corresponds to the efficiency at the TDC threshold. For an incident angle of 16 degrees, the range of TDC thresholds indicates a detection efficiency of between 70% and 20%. The actual data show that the detection efficiency drops to 60% with the "`smxtdc cut`", which is reasonably consistent with the simulation results. For an incident angle of 39 degrees, the lowest ADC threshold corresponds to an efficiency of approximately 80%. In comparison, the actual data show a detection efficiency of 60% with the "`geriTimestamp cut`". Given that the detection efficiency decreases sharply near this threshold, the results are considered reasonable.

The green plot in the figure corresponds to the maximum incident angle of 30 degrees, as expected for the E16 experiment. The detection efficiency drops sharply around 1.4 fC to 1.6 fC, suggesting that the ideal threshold is approximately 1.2 fC. The detector noise is about 1000 electrons (= 0.16 fC), indicating that such a threshold setting is feasible. However, it is important to note that the TDC threshold must also be set below this level.
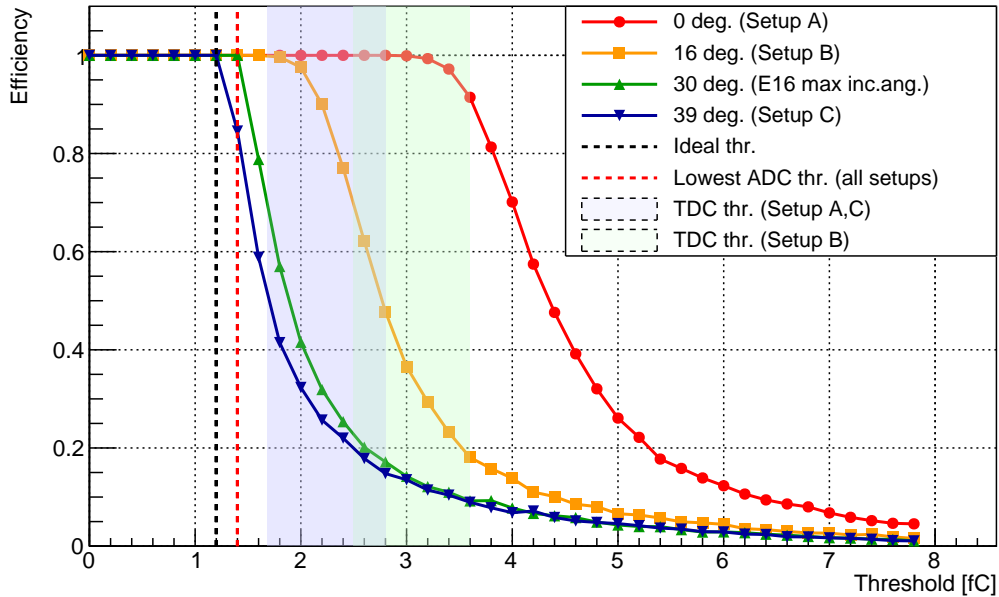
Figure 5.23: Threshold dependence of detection efficiency at each incident angle (simulation with Garfield++).

5.5.3   Cluster size and charge

Using the same simulation as in the previous section, the cluster size and cluster charge were evaluated to determine whether they are qualitatively reasonable. Since the actual experimental TDC thresholds vary significantly, the evaluation was conducted using only the ADC threshold, which exhibits less channel dependence.

Figure 5.24 shows the distributions of cluster size and cluster charge when clusters are formed using only hits exceeding the setup's lowest ADC threshold of 1.4 fC. These correspond to the cluster size distributions with the "`geriTimestamp cut`" in Fig. 5.20 (upper panels) and the cluster charge distributions with the "`geriTimestamp cut`" in Fig. 5.22 (upper panels). Additionally, the distributions correspond to Setup A, B, and C from left to right.

From this, it can be seen that both the cluster size distributions and the cluster charge distributions qualitatively agree well with the experimental data. In this simulation, diffusion effects were not included, which likely results in slightly smaller cluster sizes compared to the experimental values. Additionally, the characteristic two peaks observed in the cluster charge at an incident angle of 16 degrees were also reproduced in the simulation. This is attributed to the threshold level; many strips barely fail to exceed the threshold, causing instances where regions expected to appear as cluster size two are instead detected as cluster size one. While this has little impact on detection efficiency or trajectory detection, it is a factor that must be carefully considered when using the data for particle identification involving charge loss.
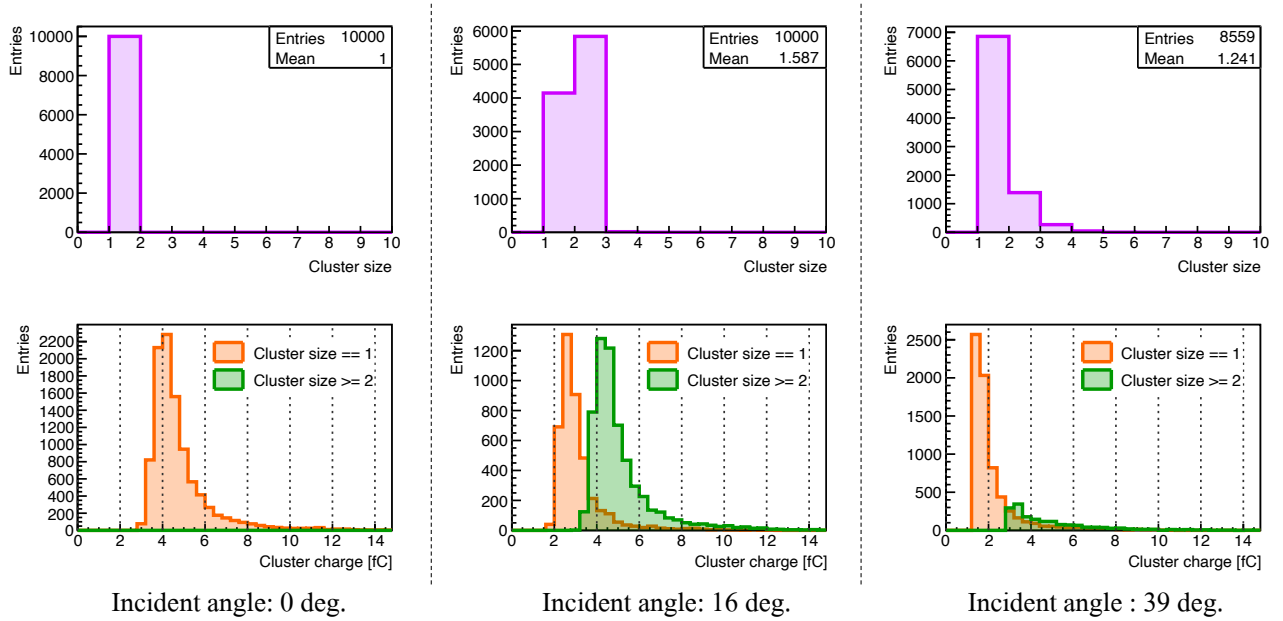
Figure 5.24: Cluster size and charge distributions for each sensor incident angle (simulation with Garfield++). Clusters were formed using only hits exceeding the threshold of 1.4 fC.

5.6   Issues and improvements

Through this experiment, three key issues were identified and addressed. The first is the threshold adjustment, which has been frequently discussed. The second is power operation, and the third is the repeater, a circuit component specific to the E16 experiment. The details are described below.

5.6.1   Threshold adjustment

As described in Section 2.2.3, the TDC threshold must be set sufficiently lower than the lowest ADC threshold. Additionally, each channel is equipped with a trimming DAC, allowing for individual threshold adjustments, which can minimize channel dependence of the thresholds. However, as discussed previously, this test experiment did not have these adjustments implemented, resulting in the inability to obtain correct TDC values.

Learning from this, a threshold adjustment algorithm was implemented. This algorithm is based on the one used in CBM but has been improved and implemented for our experiment. Additionally, a method for verifying the appropriate position of the TDC threshold was devised and established (Appendix C.2).

Figure 5.25 shows the results of the threshold adjustment. The left panel displays the threshold distribution before adjustment, while the right panel shows the distribution after adjustment. From this, it is evident that channel dependence of the thresholds was almost eliminated after adjustment. In the adjusted distribution, the TDC threshold is still higher than the lowest ADC threshold. This is because, due to higher noise in the TDC input compared to the lowest ADC input, all thresholds

were initially raised and aligned. Following this, all TDC thresholds will be lowered to the level of the lowest ADC thresholds.

This implementation was not ready in time for Run-0e, during which thresholds were manually adjusted for each channel to align as closely as possible and set carefully below the ADC threshold. For Run-1, the implemented algorithm will be used to acquire data.
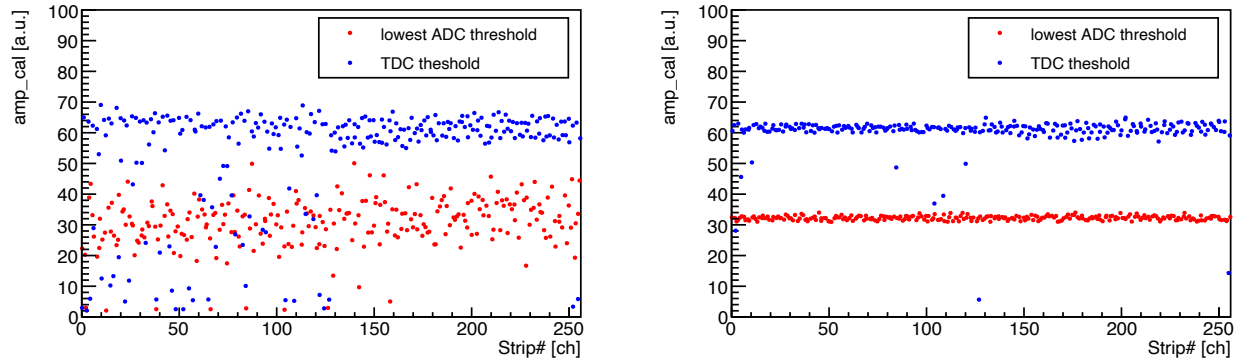

Figure 5.25: The distributions of the lowest ADC threshold (red) and TDC threshold (blue) before (left) and after (right) threshold adjustment. The left shows the state without any corrections applied using the timing DAC. See Appendix C.2 for details.

5.6.2   Power operation error

The original plan was to collect data from the 106 sensor under setups with 0 degrees, 15 degrees, and 30 degrees incident angles. However, during the setup process, I accidentally applied a high voltage of 10 V to the FEB-8, which serves as the readout circuit. Although FEB-8 is designed to prevent subsequent circuits from being damaged by high voltage, it was ultimately damaged, and correct data could no longer be read.

In this test experiment, no safety mechanism was implemented to limit the output terminal voltage for FEB-8's LV channels, leaving it vulnerable to human error. As a result, the high voltage was applied. Learning from this mistake, I modified the system to allow the output terminal voltage limit to be visible in the GUI and ensured careful attention when setting up new channels (Fig. 4.14).

5.6.3   Communication with LVDS repeater

As shown in Section 4.3, the E16 experiment uses LVDS repeaters to amplify signals for long-distance transmission to address magnetic field and radiation concerns. However, during this test experiment, applying bias voltage to the sensors often caused ACK[1] (Acknowledgment) response failures. Therefore, all data used for analysis were collected without using the LVDS repeaters.

Signals from the FEB-8 are transmitted as LVDS differential signals. It was hypothesized that the instability in the potential of these differential signals caused communication issues when bias voltage was applied to the sensors. To address this, one side of the differential signal line was connected to a large GND through a $10\,\mathrm{k\Omega}$ resistor (Figure 5.26). This improvement significantly

---

[1]ACK: An ACK response is a message sent in data communication to confirm that data has been successfully received. For example, in TCP communication, the sender transmits data, and the receiver sends an ACK to confirm receipt. If no ACK is received, the sender retransmits the data to ensure reliable communication.

reduced the communication failure probability due to ACK response errors during slow control to approximately 30-40%. This modification was implemented during the Run-0e installation.
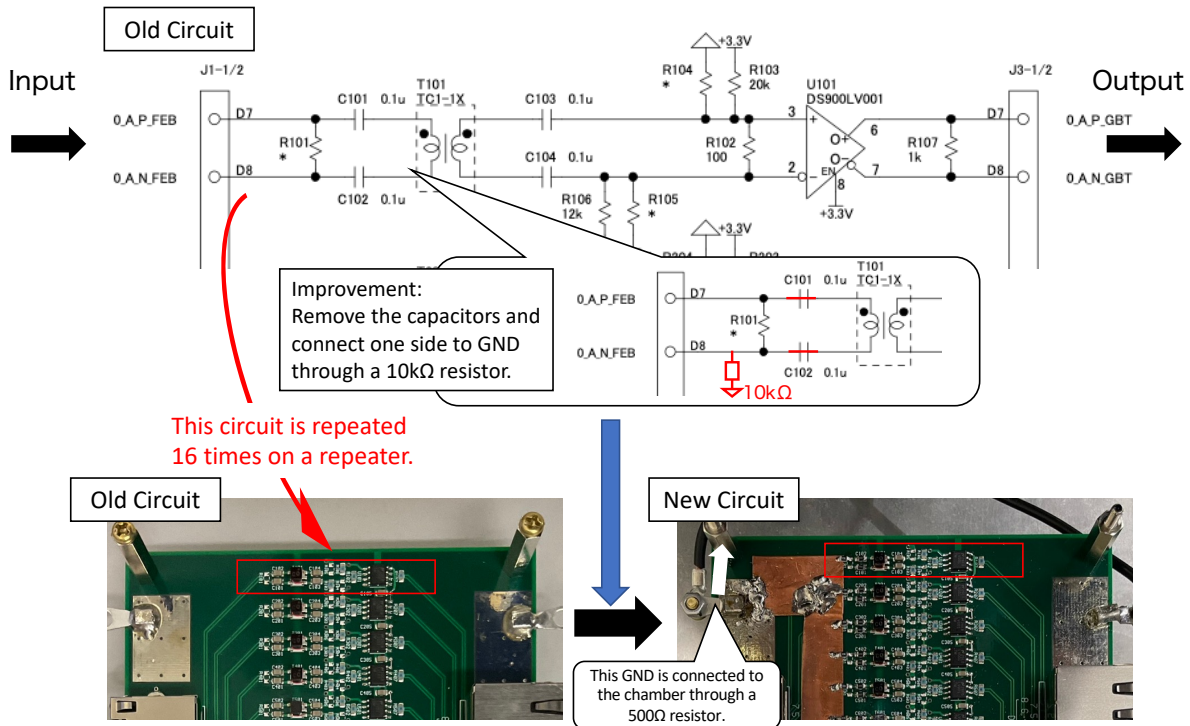

Figure 5.26: LVDS repeater improvement.

However, it is difficult to conclude that this is the only cause, as ACK response errors frequently occur with the FEB-8 of specific modules. This remains an unresolved issue.

5.7   Summary

A test experiment using an electron beam was conducted at the KEK PF-AR detector test beamline, confirming that the DAQ system of the E16 STS was functioning successfully. For sensor performance evaluation, a detection efficiency of 98.5% (at incident angles of 0 degrees and 16 degrees) and time resolutions of 4.3 nsec (at 0 degrees) and 5.4 nsec (at 16 degrees) after the timewalk corrections were achieved. These results meet the performance requirements of CBM and E16 experiments. Furthermore, issues related to STS operation and repeater defects were identified and subsequently improved.

Chapter 6

J-PARC E16 fifth commissioning run (Run-0e)

The commissioning run of the J-PARC E16 experiment, Run-0e, was conducted from April 20 to June 3, 2024. Using beams of 1×10^9 pps[1], 5×10^9 pps, and 1×10^{10} pps, data were collected for detector performance evaluation, calibration, and physics data acquisition using the physics trigger. For the evaluation of the STS, data were acquired for approximately three hours using a beam intensity of 1×10^9 pps without a magnetic field.

The first installation of the STS for the J-PARC E16 experiment was at Run-0d. However, due to insufficient preparation and a beam time reduction caused by a fire, enough data collection could not be conducted. In contrast, Run-0e was the first full-scale data acquisition for the STS using an online trigger system.

This chapter explains the implementation results of the online trigger system and evaluates the performance of the STS using data obtained from Run-0e. Additionally, some issues that occurred during Run-0e are also reported.

---

[1]pps: protons per spill, an indicator of beam intensity. In the E16 experiment, a beam of 1×10^{10} pps is used to collect physics data.

6.1   Results of online trigger selection in Run-0e

In Run-0e, the search window for coarse selection was set to 12.8 µsec, and the match window for fine selection was set to 3.2 µsec (Appendix D). Figure 6.1 shows the timing difference distribution of `smx_tdc` ⭐ and `trg_emu_tdc` ⭐ after the online trigger selection (1 tick = 3.125 nsec). A sharp peak is observed around -95 tick, indicating that the online trigger selection was successful. Additionally, the fine structures visible outside the peak are considered to correspond to the 21 nsec transverse RF[2].
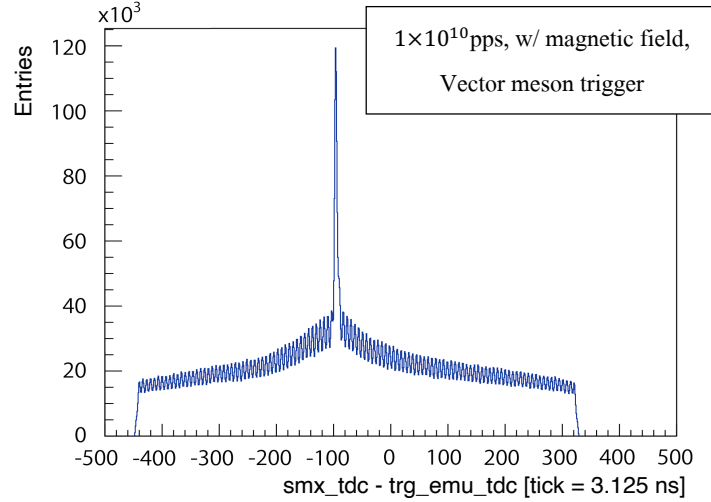
Figure 6.1: Distribution of the difference between hit timing (`smx_tdc` ⭐) and trigger timing (`trg_emu_tdc` ⭐). This data was acquired using a beam intensity of 1×10^{10} pps, with a magnetic field, and a vector meson trigger (physics data acquisition trigger).

6.2   Analysis and Results

This section describes the performance of the STS based on data obtained without a magnetic field using a beam of 1×10^9 pps. The evaluation focuses on the residuals and detection efficiency of STS clusters relative to tracks reconstructed using only the three GTR layers. The data used for this evaluation was acquired using triggers generated when GTR300 and LG were simultaneously hit (GTR × LG 1track tirgger). First, the methods of clustering STS hits and reconstructing tracks using only the three GTR layers will be explained, followed by the analysis and results. Furthermore, finally, the operational performance of STS under a magnetic field is discussed.

6.2.1   Clustering of hits of the STS

This section explains the method of clustering STS hits.

First, hits corresponding to the trigger are identified. In this analysis, the timing of hits recorded by the SMX (`smx_tdc` ⭐: 320 MHz, 14-bit) and the timing when the trigger arrived at the GBTx-

---

[2]A high-frequency electric field (47.47 MHz, corresponding to 21 nsec) introduced to improve the spill time structure by flattening the beam intensity distribution and enhancing the duty factor [49].

EMU (`trg_emu_tdc`⭐: 320 MHz, 64-bit) were used. Figure 6.2 shows the distribution of the timing difference. A sharp peak appears around -95 ticks, which is considered to correspond to the hits triggered by the event. Based on this distribution, the timing window is defined to select hits. In this analysis, hits within the light yellow range, -95 ± 100 ticks, were selected as hits corresponding to the trigger.
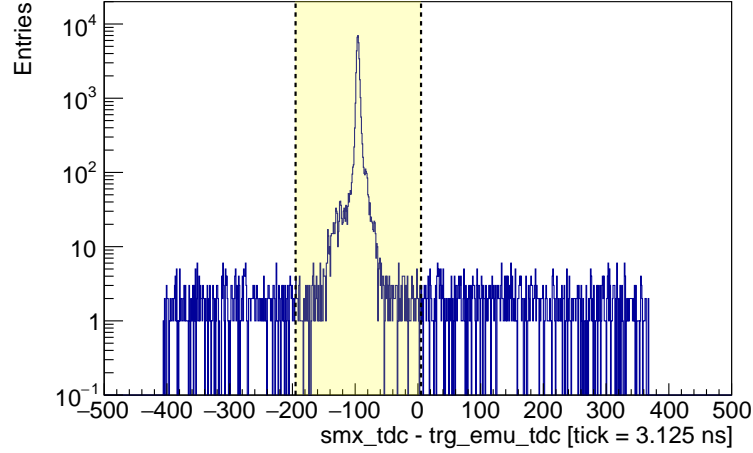

Figure 6.2: Distribution of the between hit timing (`smx_tdc`⭐) and trigger timing (`trg_emu_-tdc`⭐). The vertical axis is displayed on a log scale. This data was acquired using a beam intensity of 1×10^9 pps, without a magnetic field, and GTR $\times$ LG 1track tirgger. The yellow-colored area is the selected hit area.

Using these hits, clustering was performed by grouping adjacent strips where the timing difference between hits was 60 ticks or less. The one-dimensional cluster positions (x_{cog}) and times (t_{cog}) were determined using the Center of Gravity method, where the charge deposited on each strip is used as a weight as follows.

$$x_{\text{cog}} = \frac{\sum_{i=1}^{N} q_i x_i}{\sum_{i=1}^{N} q_i}, \qquad t_{\text{cog}} = \frac{\sum_{i=1}^{N} q_i t_i}{\sum_{i=1}^{N} q_i} \tag{6.1}$$

Here, N is the cluster size, x_i is the position of the hit strip, q_i is the ADC value of the hit, and t_i is the timing of the hit. Time walk corrections for t_{cog} were not applied in this analysis. In this analysis, only the sensor N-side (x-axis) was evaluated, so only 1D clustering was performed for STS. The position of this cluster was determined using sensor local coordinates, and for analysis using tracks, it was converted to global coordinates.

6.2.2   Track reconstruction

In this analysis, the tracks reconstructed with only three layers of the GTR are used. This section focuses to explain how to reconstruct these tracks. The process starts by clustering strip signals to determine local cluster positions in each layer. These positions are then converted into global coordinates, which are subsequently used for tracking charged particles.

Specifically, the track is determined by recursively performing the following analyses Ⓐ, Ⓑ, and Ⓒ.

Ⓐ Cluster position determination in GTR

The cluster position determination in each GTR layer follows these steps:

1. The cluster centroid position (x_{cog}) and centroid time (t_{cog}) are determined through hit centroid calculation.

2. Using the cluster centroid time (t_{cog}) and the drift velocity (v_d), the ionization position along the z-axis is calculated as Δz.

3. The correction term (Δx) is calculated using the derived (Δz) and the incident angle (θ) obtained from Ⓑ or Ⓒ, and x_{det} is determined.

First, clustering in each layer begins by identifying clusters from the hits on the strips. Using a group of adjacent hits, the centroid position (x_{cog}) and centroid time (t_{cog}) of the cluster are determined using the Center of Gravity method (Eq. 6.1), with the charge deposited on each strip serving as a weight (In this thesis, the explanation of how the charge deposited on the strips and their timing are determined is omitted.).
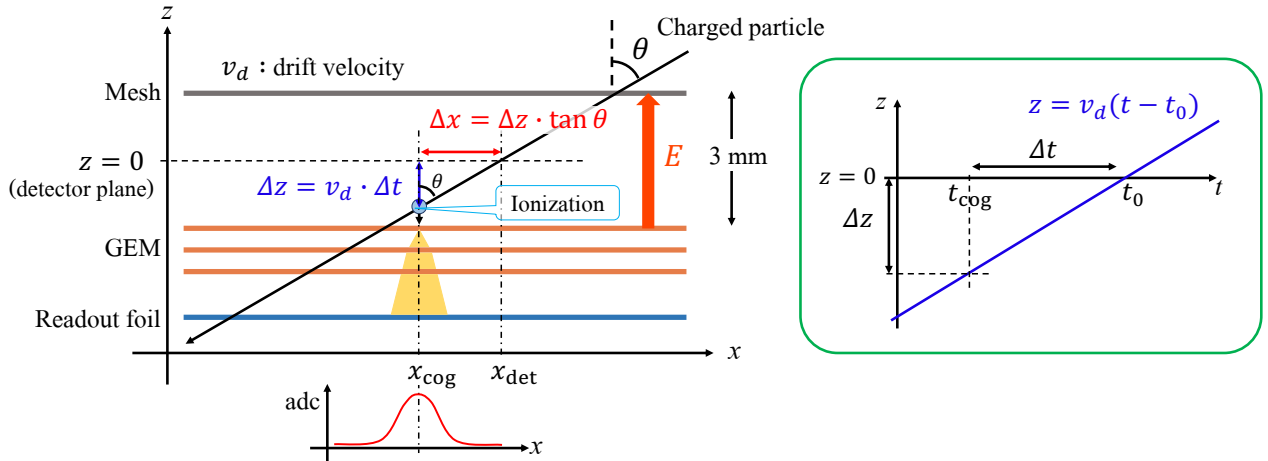

Figure 6.3: Cluster position determination in GTR.

In the GTR, ionization occurs as a charged particle passes between the MESH and the GEM. Electrons generated during this process are amplified to determine the passage position of the charged particle. The detection position of a charged particle is defined as x_{det} on the plane at the center of the MESH and GEM, i.e., at $z = 0$. For vertical tracks, x_{cog} and x_{det} are identical, and the Center of Gravity method provides sufficient position resolution. However, for angled tracks, these

values differ, requiring a correction based on the time differences of the arrival signals to achieve accurate position determination.

A drift electric field of $600\,\mathrm{V/cm}$ is applied between the MESH and the GEM. The time it takes for electrons generated by ionization to reach the first layer of the GEM varies depending on the z-axis position where the ionization occurs. By using this time difference, x_{cog} is corrected to determine x_{det}.

The dependence of detection time on the ionization position is represented as a straight line with a slope of v_d (electron drift velocity), as shown on the right in Fig. 6.3. This line is calculated using data from detector calibration runs. The time at $z = 0$ is defined as t_0, and the deviation from t_0 is denoted as Δt. Using this Δt, Δz is calculated (Eq. 6.2).

$$\Delta z = v_d \cdot \Delta t = v_d \cdot (t_{\mathrm{cog}} - t_0) \tag{6.2}$$

Then, using the incident angle θ for each layer obtained from Ⓑ and Ⓒ, Δx is calculated, and the detection position x_{det} is determined (Eq. 6.3).

$$\Delta x = \Delta z \cdot \tan\theta, \qquad \therefore x_{\mathrm{det}} = x_{\mathrm{cog}} + \Delta x \tag{6.3}$$

In this way, the detection position of the cluster, x_{det}, is calculated.

The drift velocity is typically $0.01\,\mathrm{mm/nsec}$. Given that the distance between the MESH and GEM is $3\,\mathrm{mm}$, the drift time (Δt) spans a width of $300\,\mathrm{nsec}$. This means that for a single event, the GTR timing window scans within this $300\,\mathrm{nsec}$ range[3].

Ⓑ Track finding

Track reconstruction begins with track finding. Using the cluster positions $((x_{\mathrm{cog}}, y_{\mathrm{cog}}))$ calculated in Ⓐ, all combinations of clusters from the three layers are exhaustively searched, with the constraint that only adjacent modules are allowed. A rough linear fit is then performed in the xz and ry planes to identify track candidates.

Next, for each of the three layers, the timing of x and y clusters is matched. If the timing of all three layers falls within the configured time window ($\backsim 50\,\mathrm{nsec}$), the candidate is retained as a track candidate. Duplicate tracks using the same clusters are allowed at this stage.

Ⓒ Track reconstruction

Tracking is performed using the Runge-Kutta method with the track candidates from Ⓑ, including the target position in the calculations. This tracking uses the least-squares method to search for the track.

---

[3]If hits from another event are mixed within this $300\,\mathrm{ns}$ timing window, it becomes impossible to distinguish them. The timing window mentioned in Section 4.1 refers to this issue, and this is why the STS is important for the E16 experiment.

Using these steps (Ⓐ, Ⓑ, and Ⓒ), the tracks are determined as follows:

1. Calculate x_{cog} (Ⓐ).
2. Create track candidates (Ⓑ).
3. (Correct x_{det} (Ⓐ).)
4. Track with the Runge-Kutta method (Ⓒ).
5. Correct x_{det} (Ⓐ).
6. Retrack with the Runge-Kutta method (Ⓒ).

This sequence determines the tracks.

6.2.3 Track selection

To ensure track quality in the performance evaluation of the STS, track selection was applied. The details of the track selection are shown in Table 6.1. LG timing refers to the time difference between the trigger and LG hit timing, LG residual represents the residual between the track and the LG hit, and GTR xy timing corresponds to the timing of the clusters in the xy plane.

Table 6.1: GTR track selection.

Parameter	Cut value
χ^2	$\chi^2 \leqq 5$
LG timing	$40 < t_{\mathrm{LG}} < 120$ tick [1tick=1.04 nsec]
LG residual	$|\mathrm{residual}_x| < 100\,\mathrm{mm}$, $|\mathrm{residual}_y| < 100\,\mathrm{mm}$
GTR xy timing (100)	$|t_x - t_y - 7| < 25\,\mathrm{nsec}$
GTR xy timing (200)	$|t_x - t_y - 7| < 25\,\mathrm{nsec}$
GTR xy timing (300)	$|t_x - t_y - 4| < 25\,\mathrm{nsec}$

Using the tracks selected based on Table 6.1, an analysis of the residuals and detection efficiency was conducted for the most forward module, 106 N-side (x) only.

6.2.4   Results of residual distribution

The intersection position of the track with the STS sensor is defined as x_{gtr}, and the residual between this position and the STS cluster position x_{sts} was calculated (Fig. 6.5, left). Here, the residuals were calculated for all STS clusters corresponding to any given track.
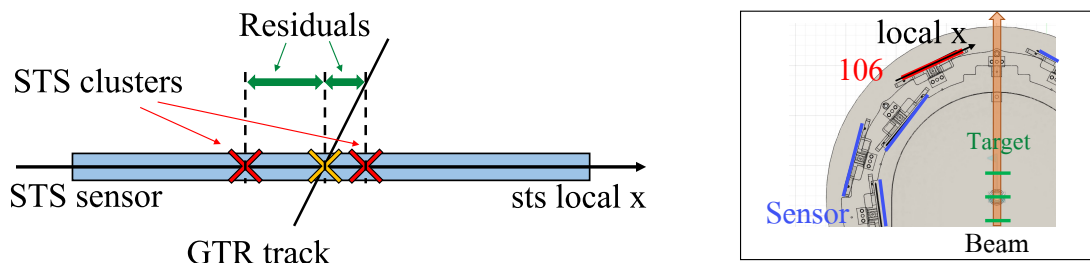
Figure 6.4: Definition of the residual between tracks and STS clusters (left) and the definition of sts_local$_x$ (right).

The left panel of Figure 6.5 shows a 2D histogram with the horizontal axis as sts_local$_x$ and the vertical axis as the residuals. The sts_local$_x$ axis is oriented with $x = 0$ at the center of the sensor, pointing toward the beam side (Fig. 6.4, right). The right panel of Fig. 6.5 shows the residual distribution over the entire local$_x$ range of the 106 sensor (a projection of the vertical axis in the left plot) and its Gaussian fit result. The Gaussian fit is performed within a range of $\pm 0.3\,\text{mm}$, resulting in a sigma of $172\,\mu\text{m}$.

Figure 6.6 shows the sts_local$_x$ dependence of the residual distribution. It is obtained by slicing the plot in Fig. 6.5 (left) into bins of $0.6\,\text{mm}$ in sts_local$_x$, fitting each slice with a Gaussian, and plotting the mean and sigma. The mean aligns well with zero in the range of local $x = -5$ to $15\,\text{mm}$ but shifts outside this range. The sigma is approximately $200\,\mu\text{m}$ for $x \geq -10\,\text{mm}$, but it increases for $x < -10\,\text{mm}$.

The residual distribution projected within the range of $x = 0\,\text{mm}$ to $10\,\text{mm}$, where the residual results are good, is shown in Figure 6.7. In this range, the residual was found to be $144\,\mu\text{m}$.
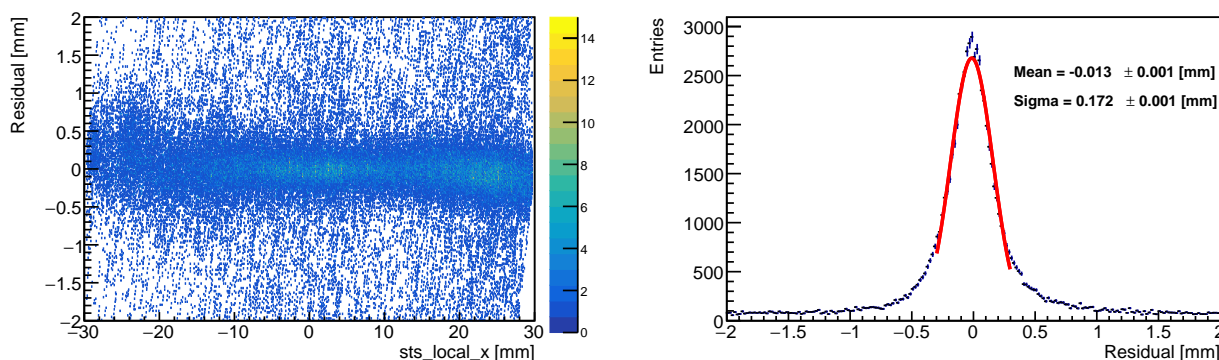
Figure 6.5: The 2D histogram with the horizontal axis as sts_local$_x$ and the vertical axis as the residuals (left) and the residual distribution over the entire sts_local$_x$ range of the 106 N-side (right).
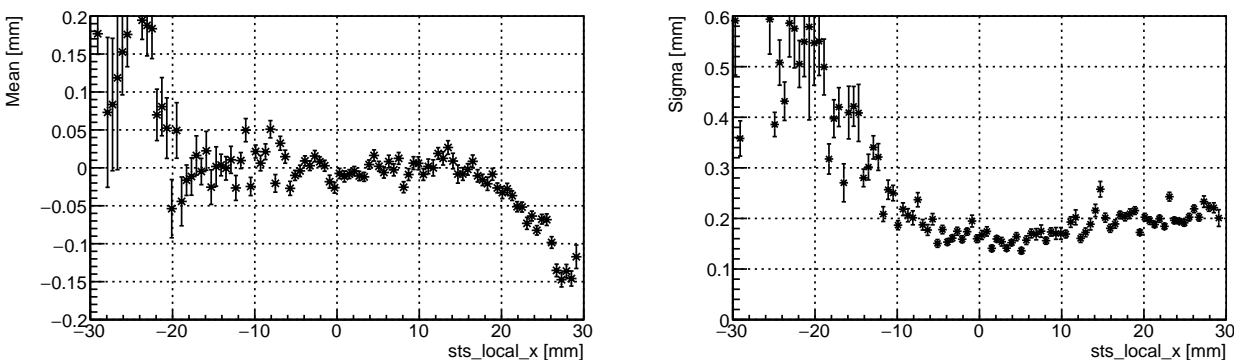
Figure 6.6: The sts_local$_x$ dependence of the residual distribution. Mean (left) and sigma (right) from the Gaussian fits.
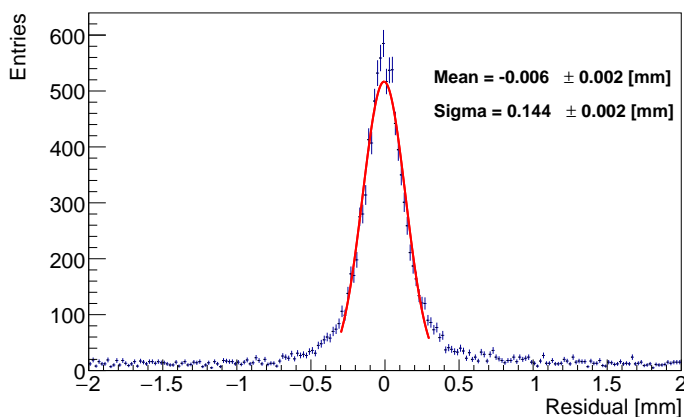

Figure 6.7: The residual distribution over the sts_local$_x$ range of 0-10 mm on the 106 N-side.

6.2.5   Results of detection efficiency

The detection efficiency was calculated as follows.

$$\text{Efficiency} = \frac{\text{The number of sensor response events corresponding to tracks}}{\text{The number of tracks}} \tag{6.4}$$

The detection efficiency analyzed here is based on tracks in the denominator and does not fully correspond to the true detection efficiency. The cut based on the residuals between STS cluster position and track used the STS cluster closest to each track.

Figure 6.8 shows a plot of detection efficiency calculated by dividing the entire range of the 106 N-side into 100 segments. The left panel presents the results when a uniform cut of $< 0.8\,\text{mm}$ (4σ @ sts_local_x $> -10\,\text{mm}$) is applied to all closest cluster residuals. In contrast, the right panel shows the results where the σ values for each sts_local$_x$ were obtained from the σ plot on the right side of Fig. 6.7, and a 4σ cut was applied based on those values. The errors are added symmetrically up

and down, as shown in Equation 6.5. For simplicity, events with tracks at the edge of the sensor ($|\text{sts\_local}_x| > 28\,\text{mm}$, $|\text{sts\_local}_y| > 28\,\text{mm}$).

$$\Delta\epsilon = \sqrt{\frac{\epsilon(1-\epsilon)}{N_{\text{trk}}}} \tag{6.5}$$

Here, ϵ represents the detection efficiency, and N_{trk} denotes the number of tracks.
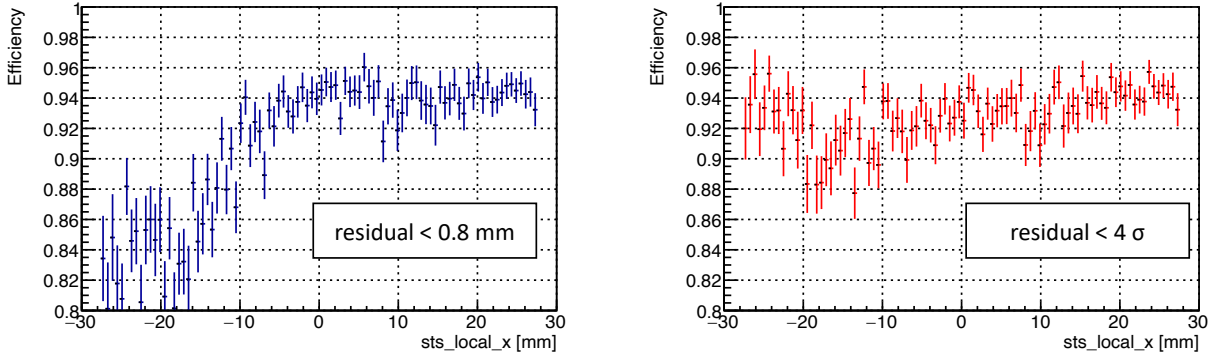
Figure 6.8: Detection efficiency for the 106 N-side, calculated by dividing the entire range into 100 segments.

6.3   Performance in under a magnetic field

The performance of the STS under a magnetic field was also investigated using a beam of 1×10^9 pps. Figure 6.9 shows the charge deposited at the STS in fC versus the track momentum. The deposited charge, which corresponds to the cluster charge after hit clustering, is obtained through threshold scan calibration (Appendix C.1). The tracks used were reconstructed using four layers: the STS and the three GTR layers. The calculated most probable values (MPV) of energy losses for pions, kaons, protons, and deuterons are also plotted. Clear bands corresponding to pions and protons are distinctly identified. This indicates that hit clustering and calibration in the STS were successful and further confirms that the STS functions properly with the E16 DAQ system.
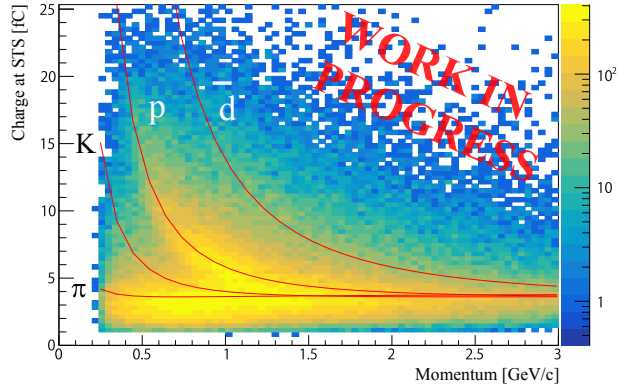
Figure 6.9: Charge of STS cluster vs track momentum.

6.4   Discussions

6.4.1   Residual distribution

Residuals in the range of $[0\,\mathrm{mm} < \mathrm{sts\_local}_x < 10\,\mathrm{mm}]$

From Fig. 6.6, the residuals width was smallest in the range $[0\,\mathrm{mm} < \mathrm{sts\_local}_x < 10\,\mathrm{mm}]$, measuring 144 µm (Fig. 6.7). To verify whether this result is reasonable, the following simple Monte Carlo simulation was conducted for evaluation.

Using the actual geometry, a setup with one STS layer and three GTR layers was modeled, and particles were injected from the target position. Gaussian smearing with $\sigma = 120\,\mu\mathrm{m}$ (the estimated position resolution of the GTR) was applied to the particle's true crossing points at each GTR layer, resulting in calculated GTR hit positions. These three hit positions were fitted to a straight line, and the residual distribution was determined as the difference between the intersection of this line with the STS ($x_{\mathrm{trk\_STS}}$) and the particle's true crossing point at the STS ($x_{\mathrm{true\_STS}}$). The result is shown on the left panel of Figure 6.10.

Additionally, the detected position of the STS ($x_{\mathrm{hit\_STS}}$) was smeared using a Gaussian distribution with $\sigma = 58\,\mu\mathrm{m}/\sqrt{12} = 16.7\,\mu\mathrm{m}$ (the estimated position resolution of the STS) relative to the true incident position ($x_{\mathrm{true\_STS}}$). The residual distribution between the intersection of the fitted line with the STS ($x_{\mathrm{trk\_STS}}$) and the detected position of the STS ($x_{\mathrm{hit\_STS}}$) is shown on the right panel of Fig. 6.10.

This simulation ignores multiple coulomb scattering, so it slightly underestimates the results.

As a result of this simulation, the residual distribution between the track reconstructed using only the three GTR layers and the STS was approximately $\sigma = 140\,\mu\mathrm{m}$, regardless of whether the STS position resolution was considered. This value is close to the experimental result of 144 µm. Since the position resolution of the GTR is much larger than that of the STS, the STS position resolution cannot be observed. However, under the assumption that the GTR position resolution is 120 µm, this result is reasonable.
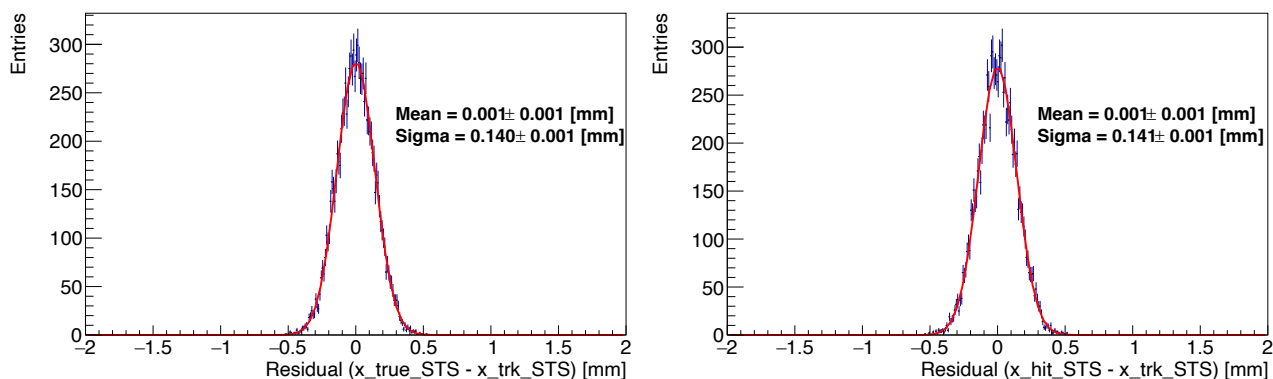

Figure 6.10: Residual distributions between the STS intersection of the track reconstructed using only the three GTR layers and the true STS incident position (left), and between the STS intersection and the detected STS position (right) from the Monte Carlo simulation.

Residuals in the range of sts_local$_x$ < -10 mm

From Fig. 6.6, the residuals width significantly increases in the range of sts_local$_x$ < -10 mm. This is likely due to the effects of multiple coulomb scattering caused by the frame of the 107 GTR module.
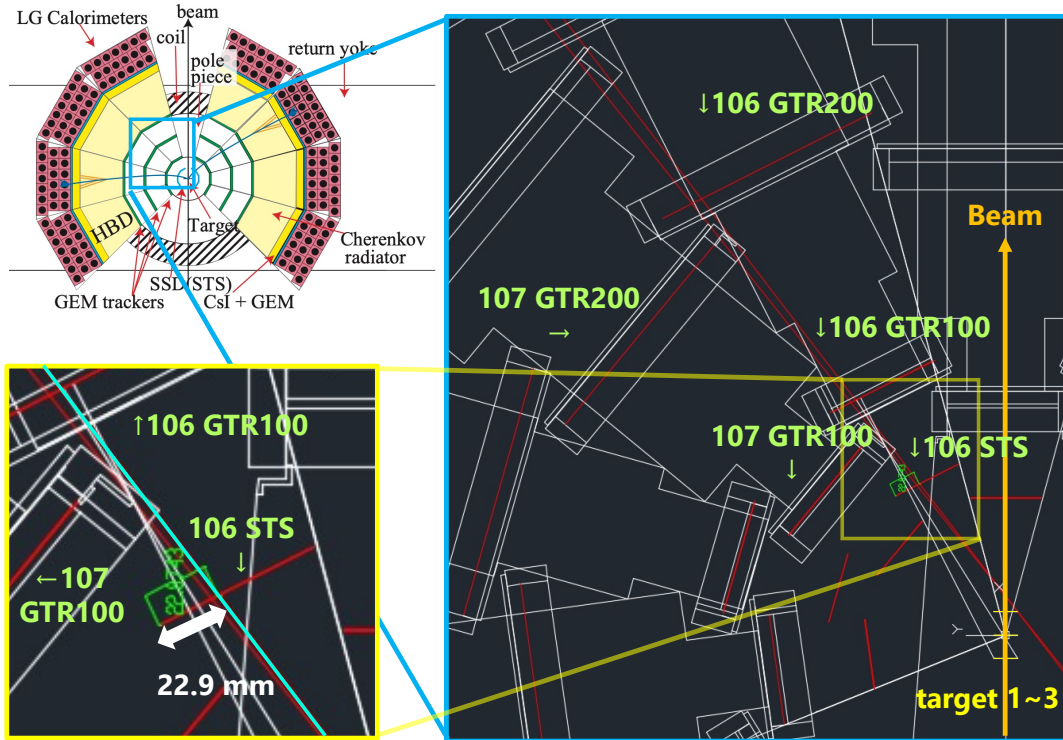

Figure 6.11: 2D CAD view of spectrometer and module overlap.

Figure 6.11 shows a 2D CAD view of the spectrometer from above. By drawing a straight line (light blue line) through the target position and the edge of the 107 GTR frame, it was found that the 106 module of the STS overlaps with the 107 GTR module in the range of approximately 23 mm from the beam's outer side, i.e., sts_local$_x$ < -7 mm. Therefore, it is considered that this overlap increases the residuals width due to the effects of multiple coulomb scattering.

6.4.2   Detection efficiency

In the left panel of Fig. 6.8, the drop in detection efficiency for sts_local$_x$ < -7 mm is likely due to the increased residuals width caused by multiple Coulomb scattering, as discussed in the previous section. Taking this into account, the detection efficiency was recalculated within a 4-sigma range of the residuals width, considering its sts_local$_x$-dependence. As a result, the dependence on sts_local$_x$ decreased, and the detection efficiency improved to approximately 93-94%. This is close to the E16 performance requirement of 95% (Section 4.1), confirming that the requirement is nearly met.

However, this result is worse than the results from test experiment at KEK PF-AR. As mentioned in the analysis part, this difference is attributed to the denominator being the reconstructed tracks,

making the efficiency highly dependent on the quality of the tracks. Evaluation of track purity is underway.

6.5   Detector status and issues

Various issues were identified during Run-0e, and countermeasures were implemented. This section describes the identified issues and improvements.

6.5.1   Increase of leakage current

The E16 STS sensors are operated by applying $+75\,\mathrm{V}$ to the N-side and $-75\,\mathrm{V}$ to the P-side, forming a depletion layer with a reverse bias voltage of $150\,\mathrm{V}$. Under reverse bias, almost no current flows through the sensors; however, a small amount of current may flow, known as "leakage current". During Run-0e, an increase in leakage current was observed in each sensor.

Figure 6.12 shows a plot of the leakage current variation in the 106 module during Run-0e, overlaid with the beam intensity used in the experiment. It was observed that when the beam intensity exceeded 5×10^9 pps, the leakage current gradually increased. This increase was not temporary. Measurements in the laboratory after Run-0e showed that the leakage current increase had accumulated and persisted even after the beam exposure ended.

Table 6.2 shows a comparison of the leakage current for each sensor before and after Run-0e. The measurements after Run-0e were conducted in the laboratory following the conclusion of the experiment. Typically, the leakage current was $3\,\mathrm{\mu A}$ before Run-0e, but it increased by nearly $10\,\mathrm{\mu A}$ in the forward-most 104 and 106 modules. Additionally, module 101 showed a significant increase, with leakage current rising by nearly $40\,\mathrm{\mu A}$.
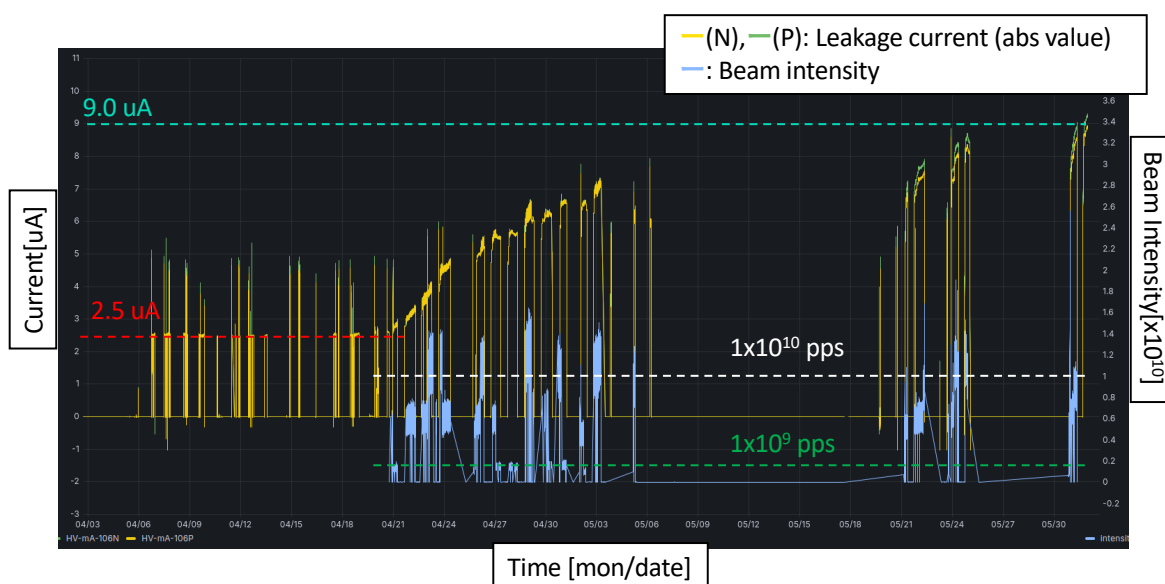
Figure 6.12: Variation of leakage current (106 module) and beam intensity.

Table 6.2: Comparison of leakage current before and after Run-0e. (*See Section 6.5.3)

Module	Before Run-0e (N/P) [µA]	After Run-0e (N/P) [µA] (24th July 2024)
101	+3.1 / -3.0	+38.7 / -38.7
102	+3.3 / -3.2	+8.1 / -7.7
103	-	+12.5 / -12.1
104	+2.4 / -2.2	+11.1 / -10.2 (+100 V/-2 V)*
108 (106 in Run-0e)	+2.5 / -2.4	+10.2 / -9.8
107	+2.3 / -2.0	+9.7 / -9.3
109	+2.1 / -2.0	+6.4 / -6.0

The increase in leakage current was initially attributed to potential radiation damage. However, an estimate of the number of irradiated neutrons revealed that the radiation dose was insufficient to cause bulk degradation leading to an increase in leakage current. Therefore, it is considered to be an issue on the circuit side (FEB-8s) rather than sensor damage.

Additionally, laboratory tests conducted after Run-0e showed that leakage current fluctuated significantly with room temperature changes. For instance, in an unheated laboratory in December (approximately 15°C), the leakage current of the 104 module dropped to around $\pm 5 \, \mu A$.

Although the exact cause of this issue remains unknown, plans for the next run include embedding a thermometer near the sensor inside the chamber to record temperature changes and circulating dry air to control humidity.

6.5.2 Time-zero shift in SMX TDC

In the test experiment conducted at Tohoku University ELPH in 2021, a phenomenon involving a time-zero shift in `smx_tdc` was observed [41]. However, since the FEB-8s are time-synchronized during initialization, such a phenomenon should not occur. At present, the root cause of this issue remains unexplained. A similar phenomenon was occasionally observed suddenly during data acquisition in Run-0e.

This issue was rarely observed in the FEB-8s of 104 N-side and 102 N-side during Run-0e. For these two FEBs, problems occurred during data acquisition with the 1×10^{10} pps under a magnetic field. Figure 6.13 shows the distribution of the difference between `smx_tdc` and `trg_emu_tdc` for hits in 104 N-side when this phenomenon occurred. The left panel shows the distribution for all SMX chips in 104 N-side, while the right panel overlays the distribution for each SMX chip using different colors. Under normal circumstances, all chips are time-synchronized, and the peaks align. However, when this phenomenon occurs, a time-zero shift happens, causing the peaks to become misaligned.

Although the cause remains unknown, the following two characteristics were consistently observed when this phenomenon occurred:

- The issue occurs only occurs when the DAQ is restarted.

- When the phenomenon occurs, slow control for the SMX becomes unresponsive.

As a temporary solution, shifters monitor the timing distribution (Fig. 6.13 left) using online monitors. If the distribution shows multiple peaks, the FEB-8 is re-synchronized, and the run

is restarted. Since this issue occurs only rarely, this approach is currently considered sufficient. However, it remains unclear whether the root cause lies in the E16 DAQ circuit or the SMX itself.
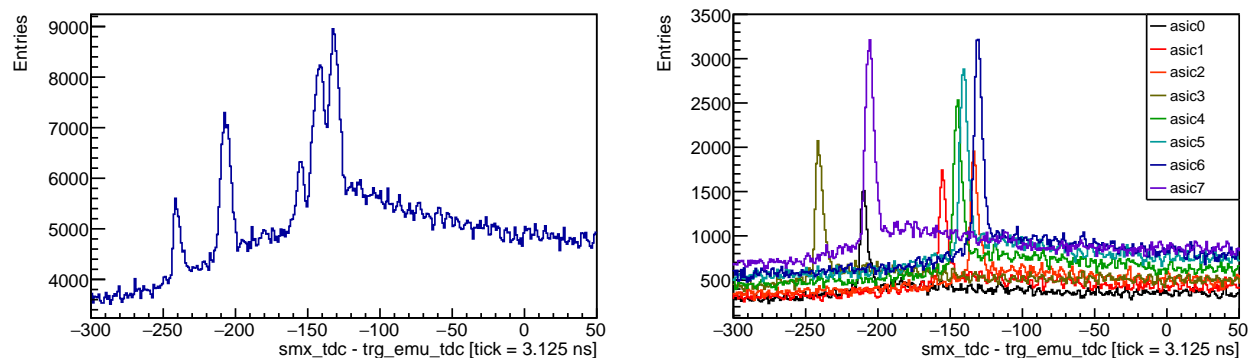

Figure 6.13: Timing distribution in `smx_tdc` misalignment (104 N-side).

6.5.3   Power supply failure

Two power supply failures occurred during Run-0e. The first failure involved the simultaneous shutdown of power to all channels. The second failure resulted in a loss of control, causing a high reverse bias voltage to be applied to the sensors, which led to a breakdown of the 104 module. These failures are believed to be caused by radiation effects.

The power supply was installed in a position directly exposed to radiation in the event of an abnormal beam, as there were no barriers between it and the beamline. As a result, the two failures occurred, with the second failure causing severe damage to the 104 module.

During the second failure, the 104 module experienced a reverse bias voltage of $\sim 600\,\mathrm{V}$, with $+490\,\mathrm{V}$ applied to the N-side and $-100\,\mathrm{V}$ to the P-side. This condition lasted for 2-3 minutes. When attempting to adjust the abnormal output voltage caused by the failure, the power supply malfunctioned, resulting in this high voltage being applied. After the incident, applying a bias voltage to the 104 module revealed normal behavior on the N-side, but the P-side exhibited a leakage current of $30\,\mathrm{\mu A}$ (typically around $1\,\mathrm{\mu A}$) at $\pm 5\,\mathrm{V}$. Consequently, an asymmetric bias voltage of $+100\,\mathrm{V}$ on the N-side and $-2\,\mathrm{V}$ on the P-side was applied to continue operation during Run-0e. Investigations conducted in the laboratory after Run-0e confirmed that the HV power supply through the connectors functioned without issues and that symmetric bias voltage could be applied. This led to the conclusion that the sensor itself was undamaged.

To prevent such incidents in the future, the following measures were implemented:

- Relocating the power supply behind a magnet yoke to reduce radiation exposure.

- Reconfiguring the power supply to automatically shut down if abnormal currents are detected.

- Installing 200 V zener diodes between the +/- terminals of the HV cables to limit the maximum voltage.

- Establishing a strict protocol to immediately shut down the power supply without attempting to adjust output voltage in the event of an issue.

With these measures in place, unexpected high voltages should no longer occur, and even if they do, significant damage is unlikely to result.

6.6   Summary

Run-0e, conducted in May 2024, was the first full-scale data acquisition for the E16 STS. It was also the first time that data acquisition using an online trigger selection was performed with the STS, and its successful operation was confirmed.

Furthermore, analysis of data collected without magnetic field showed that the detection efficiency for tracks reconstructed using only the three layers of the outer tracking detector (GTR) was approximately 94% (for one side of the STS sensor). Although further evaluation of track quality is necessary, this result is considered to meet the performance requirements of the E16 experiment. Moreover, the residual distribution between these tracks and the STS clusters also showed reasonable results, assuming a GTR position resolution of 120 μm.

In addition, the analysis of data acquired with a magnetic field confirmed that the STS functioned properly with other E16 detectors and the DAQ system. This was demonstrated by the distribution of cluster charges vs momentum, indicating successful hit clustering, calibration, and event selection.

Future performance evaluations will require further advancements in the analysis of data acquired with a magnetic field, as well as assessments of 2D cluster detection efficiency and position resolution using both sides of the sensors. Additionally, since data acquisition was also conducted in a streaming mode (triggerless data acquisition), evaluating the rate tolerance remains an important future challenge.

Chapter 7

Summary

This study focuses on the development and performance evaluation of the Silicon Tracking System (STS), the primary tracking detector for the next-generation high-luminosity heavy-ion collision experiment, Compressed Baryonic Matter (CBM) experiment.

The STS is a double-sided silicon strip detector with a thickness of $320\,\mu m$ and a strip pitch of $58\,\mu m$. It consists of eight layers of sensors capable of reconstructing the tracks of charged particles. Currently, the STS sensors are being implemented as the innermost tracking detector in the J-PARC E16 experiment, which uses a high-intensity proton beam. The purpose of this study is to implement the STS sensors in the J-PARC E16 experiment and evaluate their performance under a magnetic field.

In a test experiment conducted at the KEK in November 2023 using an electron beam, the STS sensors achieved a time resolution of approximately $5\,nsec$ and a detection efficiency exceeding 98.5%, meeting the performance requirements for both the CBM and E16 experiments. Following this test, issues identified during the experiment were addressed, and the implementation of the STS sensors for the E16 experiment was completed.

During the commissioning run of the E16 experiment (Run-0e) conducted in May 2024, the STS successfully operated stably in a magnetic field environment. It was also the first time that data acquisition using an online trigger selection was performed with the STS, and its successful operation was confirmed. Data analysis conducted without magnetic field showed that the detection efficiency of one side of the STS sensors was approximately 94% for tracks reconstructed using only the three layers of the outer tracking detector (GTR). Furthermore, the residual distribution between these tracks and the STS clusters showed reasonable results when a GTR position resolution of $120\,\mu m$ was assumed. In addition, the analysis of data acquired with a magnetic field confirmed that the STS functioned properly with other E16 detectors and the DAQ system.

Future challenges include further detailed analysis of the data obtained with a magnetic field environment and evaluations of the 2D cluster detection efficiency, position resolution using both sides of the STS sensors and rate tolerance. Currently, efforts are underway to address the issues identified in Run-0e and prepare for Run-1. In Run-1, the operation time is expected to be approximately 3,000 hours, which is about ten times longer than that of Run-0e. Therefore, the long-term operation of the modules will also be demonstrated.

Acknowledgments

謝辞

Appendix A

Sensor topology and E16 new ladders

A.1   STS sensor topology

The strips at the edge of the P-side of the STS sensor are electrically connected to the strips at the opposite edge through double-metal-layer (DML) wiring. This design is implemented because the strips on the P-side are tilted by 7.5 degrees, requiring the signals from the short strips at the edges to be read. These strips are referred to as "z-strips". As mentioned earlier, the DML often increases the total capacitance of the strips, which can affect signal quality and overall detector performance. Consequently, the noise level in this sensor region increases. For the 60-mm-long sensors used in the E16 experiment, the z-strips occupy a region of $60\,\mathrm{mm} \times \tan(7.5°) = 8.25\,\mathrm{mm}$ from the edges (Figure A.1).
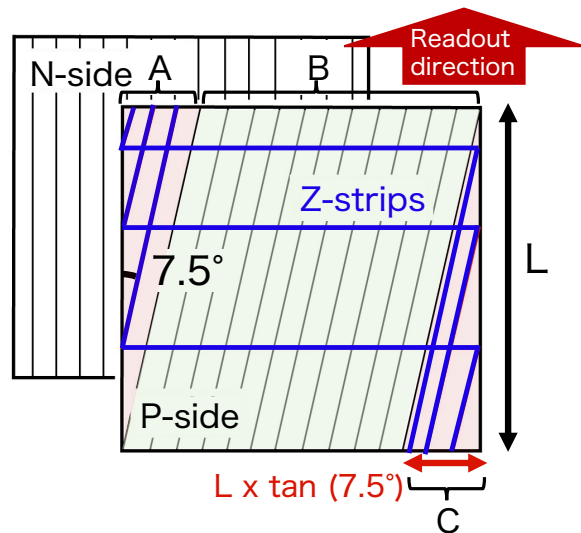
Figure A.1: Schematic of the STS sensor with a stereo angle of 7.5 degrees on the front p-side. The sensor is divided into three regions: corner regions (A, C) and central region (B). Horizontal metal lines (DML) interconnect read-out strips in the corner region (C) to avoid connectivity issues [18,50].

A.2   E16 STS new ladders

For Run-1, some ladders were rebuilt. This was due to issues such as modules where high voltage was mistakenly applied to the FEB-8s and modules with unusually high levels of noise. The following table lists the newly rebuilt modules. Additionally, L4 (106-v2-GSI) and L6 (104-v2-GSI) are on the N-side instead of the P-side, which is against the E16 ladder rule: "The ladder side faces the P-side".

Table A.1: E16 version2 ladders for Run-1.

Ladder No.	Sensor No.	Micro-cable [mm] N	Micro-cable [mm] P	Radius ± 0.16 [mm]	Ladder rule N↑P↓/ P↑N↓
L6	104-v2-GSI (106-v2-JP)	121	121	148.81	P↑N↓
L4	106-v2-GSI (104-v2-JP)	121	121	148.81	P↑N↓
L3	103-v2	172.5	163.1	117.386	N↑P↓
L1	101-v2	142	131	117.386	N↑P↓

Appendix B

Data structure from SMX ASIC

The following table lists the types of data frames sent from the STS-XYTER ASIC via the uplink.

Table B.1: Types of data frames from the STS-XYTER ASIC.

Type	Description
Dummy Hit	A frame sent to synchronize timestamps when no hit occurs
Hit	A frame that sends regular hit information
TS_MSB	A frame recording the upper 6 bits of the timestamp, sent when necessary
RDdata_ack	An acknowledgment frame sent in response to a successful data read command
Ack	An acknowledgment frame sent for purposes other than data readout
ALERT_FRM	A frame sent based on the status register to record the chip's state
SEQ_ERR	A sequence error frame

Each data frame consists of 24-bit and is converted to 30-bit via 8b10b encoding when sent to the GBTxEMU. Figure B.1 shows the detailed structure of the data frames [25]. While preparing the E16 STS DAQ environment, errors in the table from this manual were identified. The table below Fig. B.1 is the revised version.

Structure of the uplink frames (before 8b/10b encoding)

BYTE<0>: frame_bits<23:16>, bits_8b10b<29:20> — BYTE<1>: frame_bits<15:8>, bits_8b10b<19:10> — BYTE<2>: frame_bits<7:0>, bits_8b10b<9:0>

Type	23	22	21	20	19	18	17	16	15	14	13	12	11	10	9	8	7	6	5	4	3	2	1	0
Dummy Hit	0	7-bit channel address = 0x00							5-bit ADC = 0x00					0x0		0x0 (SMX2.1: Timestamp<13:0> (actual state of counter) can be switched on by CONFIG register 192, 3) <2> [crossed out]								0
Hit	0	7-bit channel address							5-bit ADC > 0x00					TS<9:8> (overlap)		Timestamp<7:0>								EM
TS_MSB	1	1	Timestamp<13:8>						Timestamp<13:8> [crossed, orig. Timestamp<13:0>]								Timestamp<13:8> [crossed]				4-bit CRC poly 0x9 = (x⁴)+x+1			
RDdata_ack (implemented)	1	0	1	15-bit register content																	3-bit sequence number (LSB)			3-bit CRC poly 0x5 = (x³)+x+1
Ack (SMX2)	1	0	0	ACK	4-bit sequence number				CP	4-bit status value				0x00 or Timestamp<7:2> depending on CONFIG<1> register setting							4-bit CRC poly 0x9 = (x⁴)+x+1			
Ack (SMX2.1)	1	0	0	ACK 0x1 Or NACK 0x2	4-bit sequence number				CP	4-bit status value				0x00 or Timestamp<13:8> Depending on the config register col=3 bit <1>.							4-bit CRC poly 0x9 = (x⁴)+x+1			
ALERT_FRM (SMX2.1)	1	0	0	0x3	11-bit STATUS register content (not masked by Col=36 register!)																4-bit CRC poly 0x9 = (x⁴)+x+1			
SEQ_ERR	1	0	0	0x0	TBU																TBU			

BYTE<0>: frame_bits<23:16>, bits_8b10b<29:20> — BYTE<1>: frame_bits<15:8>, bits_8b10b<19:10> — BYTE<2>: frame_bits<7:0>, bits_8b10b<9:0>

type	23	22	21	20	19	18	17	16	15	14	13	12	11	10	9	8	7	6	5	4	3	2	1	0
Dummy Hit	0	7-bit ch addr = 0x00							5-bit ADC = 0x00					Timestamp<8:0>									0	0
Hit	0	7-bit ch addr							5-bit ADC					TS<9:8>		Timestamp<7:0>								EM
TS_MSB (sent by dummy hit)	1	1	Timestamp<12:7>						Timestamp<12:7>								Timestamp<12:7>				4-bit CRC			
TS_MSB (sent by hit)	1	1	Timestamp<13:8>						Timestamp<13:8>								Timestamp<13:8>				4-bit CRC			

Figure B.1: Structure of the uplink frames [25].

Appendix C

Threshold

C.1 Threshold scan (pscan)

Threshold scanning (pscan) is performed to verify the ADC fC conversion, noise levels, and threshold values. The procedure and analysis of threshold scanning are conducted as follows:

1. Threshold scanning for each chip and each strip channel of FEB-8 The ADC uses 5-bit for digitization, which corresponds to 31 threshold levels. It is equipped with an internal counter that records the number of pulses exceeding each threshold. Calibration pulses can be generated with amplitudes ranging from 0 to 255 (corresponding to approximately 0 fC to 14 fC). For each strip, pulses are input N times, and the counter values are read. By repeating this process while gradually changing the pulse amplitude, ADC calibration can be performed. This calibration yields a graph like the one shown in Figure C.1. The horizontal axis represents the amplitude of the calibration pulse, and the vertical axis indicates the counter value corresponding to a specific ADC threshold. This plot is referred to as "S-curve". This plot is created for each ADC value and TDC threshold of every channel. A step size of 1 for the pulse height and $N = 100$ pulses is recommended for the pscan. Figure C.1 shows the S-curve for a specific strip channel and ADC channel with a step size of 4 and $N = 200$ pulses.

Figure C.1: S-curve.

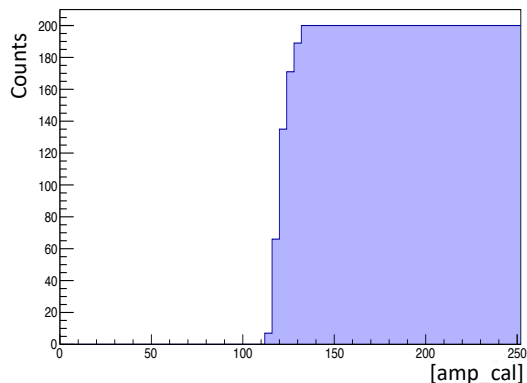**2.Fitting of S-curve** For each chip, each strip channel, and each ADC channel, the graph obtained in step 1 is fitted using the following error function with the mean value μ, standard deviation σ, and amplitude $A = N$:

$$A \cdot \mathrm{erf}\left(\frac{x - \mu}{\sqrt{2}\sigma}\right) = A \cdot \frac{2}{\sqrt{\pi}} \int_0^{\frac{x-\mu}{\sqrt{2}\sigma}} e^{-t^2}\, dt, \tag{C.1}$$

Here, the obtained mean (μ) corresponds to the threshold level of the channel, and the sigma (σ) corresponds to the noise of the channel.

3. Charge and ENC conversion   The pulse height in arbitrary units (`amp_cal`) is converted to charge or the number of electrons. We perform this conversion using the following equation.

$$1\,[\texttt{amp\_cal}] = 0.056\,[\text{fC}] \simeq 350\,\text{e}^- \tag{C.2}$$

C.2   Threshold adjustment

Threshold adjustment is performed for each ADC threshold and FAST (TDC) threshold, and is performed for each ASIC. The details of the threshold adjustment method for each threshold are explained below. The following adjustment algorithm is a slightly improved version based on the method used in CBM experiment.

C.2.1   ADC thresholds adjustment

The SMXv2 chip has a 5-bit flash ADC and a digital peak detector in each channel. This ADC can measure signals within a range of about 0 fC to 14 fC. The range is controlled by two reference voltages, $V_{\text{ref P}}$ and $V_{\text{ref N}}$, which can be adjusted using 6-bit registers (`VERF_P`, `VERF_N`). A resistor ladder between these reference voltages sets the threshold for the comparators (also called discriminators).

However, there are mismatches in offset values between channels and comparators. To fix this, "trimming corrections" are used to make the ADC performance uniform across all channels. Each ADC contains 31 comparators, one for each non-zero ADC value. These comparators have 8-bit trimming thresholds, which can adjust the offset by ± 150 mV.

The threshold for each comparator, V_i (i= adc ch) can be written as follows:

Figure C.2: Block diagram of the SMXv2 flash ADC [19].

$$V_i = V_{\text{ref P}} + \left(\frac{V_{\text{ref P}} - V_{\text{ref N}}}{31} \right) \times d_i \tag{C.3}$$

where d_i is ideally $(i - 1)$ to obtain V_i in equal spacing. However, in reality, there is deviation. To correct the deviation, a trimming DAC applies a correction term, δv_i.

Figure C.3 illustrates the concept of this threshold adjustment. Each strip channel is represented by a spring (corresponding to the ADC range), and each spring has 31 graduations, which correspond to individual ADC thresholds. These 128 springs are positioned between two plates, $V_{\text{ref P}}$ and $V_{\text{ref N}}$. Additionally, $V_{\text{ref T}}$ controls the height of the input pulses.

The threshold adjustment is performed as follows: ① The input pulse pedestal voltage is adjusted using `VERF_T` (6-bit register). ② The spring (the range of the ADC) is adjusted using `VERF_P` and `VERF_N`. ③ Each ADC threshold for each strip channel is finely adjusted using trimming DAC. The following sections provide a detailed explanation of these adjustment methods.
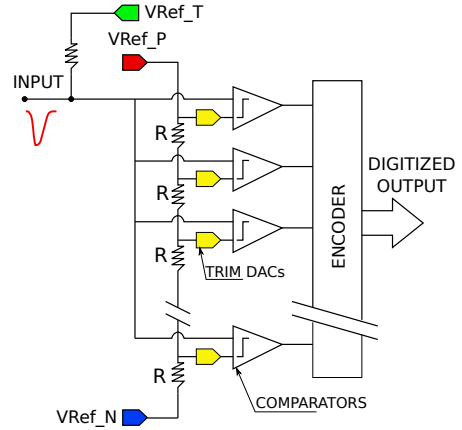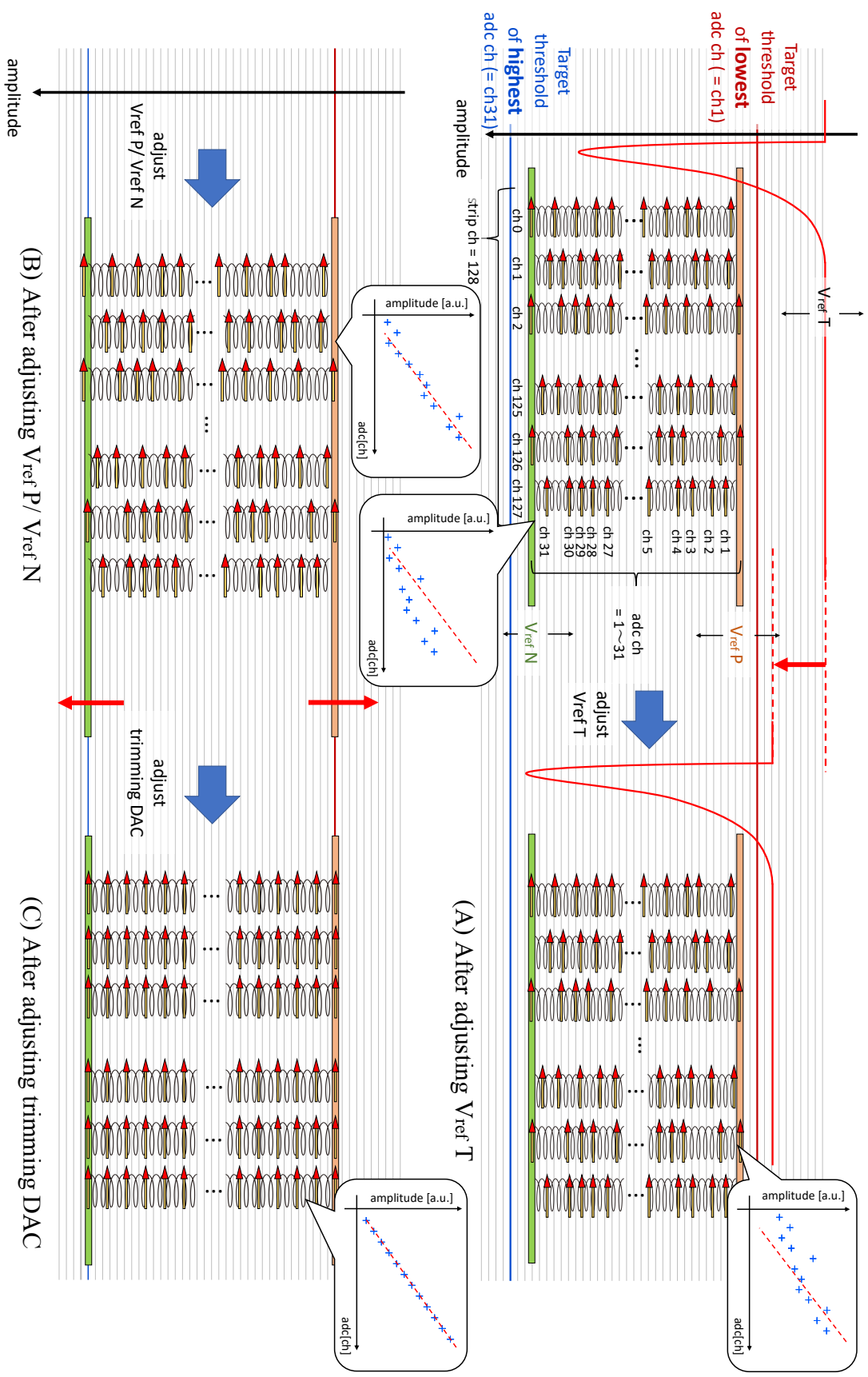
Figure C.3: Illustrative diagram of ADC thresholds adjustment.

① Adjustment of $V_{\text{ref T}}$

$V_{\text{ref T}}$ is adjusted using a 6-bit register, `VERF_T`. In SMXv2, the step size of `VERF_T` adjustment for 1 LSB (1 tick) can be selected from four options. For our purposes, we use a step size of 1 LSB $\sim 700\,e^{-}$.

$V_{\text{ref T}}$ should be set to an optimal and appropriate value. When setting the ADC range to approximately 30 to 240 `amp_cal` (1.7 to 13.4 fC), it is generally initialized to `VERF_T` = 58. By default, $V_{\text{ref T}}$ should be set slightly below $V_{\text{ref P}}$ [25].

② Adjustment of $V_{\text{ref P}}$ and $V_{\text{ref N}}$

$V_{\text{ref P}}$ and $V_{\text{ref N}}$ are adjusted with 6-bit registers, `VERF_P`, `VERF_N`. These adjustments are performed after aligning $V_{\text{ref T}}$. The procedure for these adjustments is as follows, with improvements over the CBM method highlighted in red.

---

1. Determine the height V_{low} for the **adc = 1 threshold (lowest adc thr)** and the height V_{high} for the **adc = 31 threshold (highest adc thr)**. It is recommended that $V_{\text{high}} - V_{\text{low}}$ be set to a value divisible by 30 when converted to `amp_cal`.

2. Align the trimming DAC value "`trim`" (8-bit) of each strip channel and ADC channel to the median value of 128.

3. `VREF_P`/`VREF_N` adjustment

   (a) Input pulses with a height of V_{low} / V_{high} a total of N times. Then, gradually increment `VREF_P` / `VREF_N` from a lower value and record the number of events where the ADC value exceeds 1.

   (b) The optimal `VREF_P` / `VREF_N` is defined as the value at which this event count reaches $N/2$.

   (c) To determine this optimal value, consider only the strip channels that are multiples of 5.

   (d) From these channels, exclude the three highest and three lowest event counts, then compute the average of the remaining `VREF_P` / `VREF_N` values.

Optimal $V_{\text{ref P}}$ and $V_{\text{ref N}}$ differ strip by strip. Therefore, an average is taken and adopted (step 3,4). The average is calculated over strip channels that are multiple of 5, excluding highest and lowest three $V_{\text{ref P}}$ and $V_{\text{ref N}}$ values.

Currently, this configuration is typically performed in the range of 30 to 240 `amp_cal`.

③ Adjustment of triming DACs

First, the target value V_i for each ADC channel (ADC [ch] $= i$) is determined using the following equation.

$$V_i \,[\texttt{amp\_cal}] = V_\text{low} + \frac{V_\text{high} - V_\text{low}}{\mathbf{30}} \times (i - 1) \tag{C.4}$$

Note: $V_{low} = V_{ref\,P}$, $V_{high} \neq V_{ref\,N}$.

The optimal trimming values for the target V_i is determined in two steps: "coarse adjustment" and "fine adjustment". The details of the algorithm are described below.

Coarse adjustment

First, the trimming DAC (8-bit) for each strip channel and ADC channel is set to a median value of 128. Then, the following loop is repeated N times to determine the optimal trimming values (`trim_coarse`):

---

1. For each strip channel, a pulse with an target amplitude V_i is input M times.

2. For each strip channel, the count C_i of events exceeding the ADC value i is recorded.

3. The trimming DAC value (`trim`) is adjusted based on the following conditions:

   - If $C_i > \frac{N}{2}$: **Subtract** $\frac{\texttt{width}}{j}$ from the current `trim`.
   - If $C_i < \frac{N}{2}$: **Add** $\frac{\texttt{width}}{j}$ to the current `trim`.
   - If $C_i = \frac{N}{2}$: Do not change the `trim`.

Here, j represents the trial count (starting at 1) and `width` is the initial adjustment range. The current settings are $N = 12$ (number of trials), $M = 40$, and `width` $= 25$.

Increasing the trimming value (`trim`) lowers the threshold. Therefore:

- When $C_i > \frac{N}{2}$: The `trim` is **decreased** to **raise** the threshold.

- When $C_i < \frac{N}{2}$: The `trim` is **increased** to **lower** the threshold.

Additionally, the adjustment range is gradually reduced with each trial. This approach minimizes the impact of anomalous count values. By reducing the adjustment range using $\frac{1}{j}$ while increasing the trial count, the system becomes more robust to outliers.

The `trim` determined in this way is referred to as "`trim_coarse`".

Fine adjustment

Based on the coarse trimming value (`trim_coarse`) obtained from the coarse adjustment, the optimal `trim` are determined as follows.

First, the following loop is executed N times:

---

1. Set the trimming value to `trimng_j` $=$ `trim_coarse` $+ j \times \mathrm{Step}_{\mathrm{fine}} -$ offset.

2. For each strip channel, a pulse with an amplitude V_i is input M times.

3. For each strip channel, record the number of counts $C_i(j)$ that exceed the ADC value i.

Here, j represents the trial number (starting from 1), $\mathrm{Step}_{\mathrm{fine}}$ is the adjustment step size for trimming, and offset is the starting position for trimming adjustments. The current settings are $N = 20$ (number of trials), $M = 40$, $\mathrm{Step}_{\mathrm{fine}} = 1$, and offset $= 5$. This operation involves raising the threshold slightly above `trim_coarse` and gradually lowering the trimming value step by step.

After completing the loop, calculate the average value of the last five counts $C_i(j)$, specifically $C_i(N-4)$ to $C_i(N)$, and denote it as "$C_i\_\mathrm{max\_avg}$". If the count exceeds $M \times 1.1$, **correct the count to M** for the calculation. This correction accounts for a double-counting case.

Define $C_i\_\mathrm{max\_avg}/2$ as the half-height count: "C_i_hh". The position in $C_i(j)$ where it just exceeds C_i_hh is determined as the final trimming value "`trim_fine`".

④ Readjustment of $V_{\mathrm{ref\ T}}$

After the trimming DAC adjustment is completed, the channel dependence of the threshold is minimized, and the ADC thresholds align in a straight line. Once this is achieved, further adjustments to the threshold height are allowed only by modifying $V_{\mathrm{ref\ T}}$. The threshold shift corresponding to 1 LSB of `VREF_T` differs slightly between the N-side (electrons) and P-side (holes), as follows (Figure C.4):

$$\text{N-side (electrons): 1 [LSB]} = 788\,e^- \tag{C.5}$$

$$\text{P-side (holes): 1 [LSB]} = 671\,e^- \tag{C.6}$$

Since adjustments are often made by observing `amp_cal`, the conversion is noted here. If an adjustment of x [`amp_cal`] is desired, the corresponding values can be calculated as follows:

$$\text{Adjustment for N-side (electrons): } x\,[\texttt{amp\_cal}] \to x/2.25\,[\text{LSB}] \tag{C.7}$$

$$\text{Adjustment for P-side (holes): } x\,[\texttt{amp\_cal}] \to x/1.91\,[\text{LSB}] \tag{C.8}$$

For example, if an adjustment of $x = 10$ [`amp_cal`] is required, the corresponding values for each side are calculated as follows:

$$\text{N-side: } 10\,[\texttt{amp\_cal}]/2.25 \approx 4\,[\text{LSB}] \tag{C.9}$$

$$\text{P-side: } 10\,[\texttt{amp\_cal}]/1.91 \approx 5\,[\text{LSB}] \tag{C.10}$$

Thus, the necessary adjustment in `VREF_T` can be determined for both N-side and P-side using the above conversion. Care should be taken to apply the adjustments separately for each side, as the sensitivity differs slightly between electrons and holes.

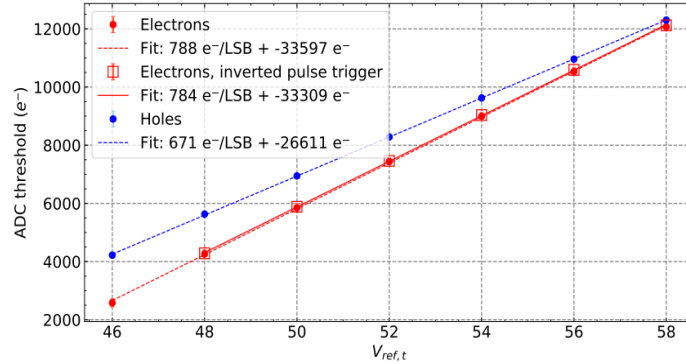This method ensures precise threshold control while maintaining alignment between the channels.

Figure C.4: The relationship between $V_{\text{ref T}}$ and the ADC lowest threshold. The slope is slightly different on the N-side (electrons) and P-side (holes).

C.2.2   FAST (TDC) threshold adjustment

The discriminator following the FAST shaper includes an 8-bit adjustable parameter, `Thr2_glb`, for each ASIC, and a 6-bit trimming DAC for each strip channel (Figure C.5). Therefore, the FAST threshold for each strip can be expressed as follows:

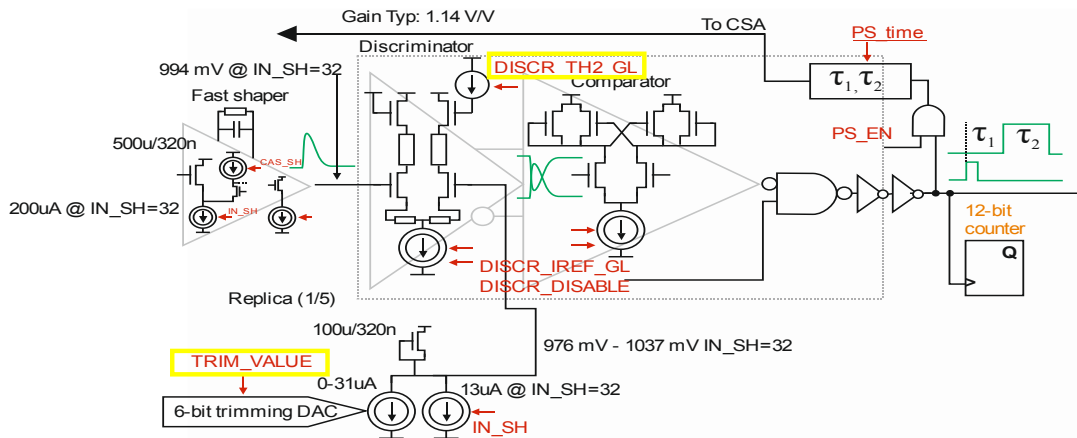$$V_{\text{fast}} = V_{\texttt{Thr2\_glb}} + \underbrace{\Delta v}_{\text{trim correction}} \tag{C.11}$$

Figure C.5: FAST discriminator [25].

The method for adjusting the FAST threshold is almost identical to that for ADC thresholds. Broadly, it involves: ① Adjusting the approximate threshold using `Thr2_glb`, and ② Tuning the

threshold for each strip channel using trimming DAC. The following sections provide a detailed explanation of this adjustment method.

① Adjustment of Thr2_glb

The parameter `Thr2_glb` is adjusted with 8-bit precision. This adjustment is similar to those of $V_{\text{ref N}}$ and $V_{\text{ref P}}$ and is performed using the following procedure. Improvements over the CBM method are highlighted in red.

---

1. Determine the target threshold height V_{fast}.

2. Align the trimming DAC (6-bit) of each channel to the median value of 31 (or 32).

3. Input pulses with a height of V_{fast} N times, then increment `Thr2_glb` from a lower value. Record the number of counts that exceed the threshold. The value of `Thr2_glb` where the count equals $N/2$ is considered optimal. This value is determined by taking the average of counts, excluding the highest three and lowest three counts, from strip channels that are multiples of 5.

4. `Thr2_glb` adjustment

   (a) Input pulses with a height of V_{fast} a total of N times. Then, gradually increment `Thr2_glb` from a lower value and record the number of counts that exceed the FAST threshold.

   (b) The optimal `Thr2_glb` is defined as the value at which this event count reaches $N/2$.

   (c) To determine this optimal value, consider only the strip channels that are multiples of 5.

   (d) From these channels, exclude the three highest and three lowest event counts, then compute the average of the remaining `Thr2_glb` values.

When adjusting the FAST threshold, the red-highlighted part of step 3 is particularly important. This is because the variation in the appropriate `Thr2_glb` values among strip channels is more significant for FAST thresholds compared to ADC thresholds.

One important note is that the fast threshold tends to befired frequently by noise at `amp_cal` values below 40. Therefore, when performing this adjustment, it is recommended to increase `amp_cal` sufficiently beforehand. The optimal range for `amp_cal` is 40 to 60.

② Adjustment of triming DAC

The S-curve created by the FAST threshold becomes complex due to noise or **slight decreases in voltage supply to SMX**. Therefore, it is challenging to adjust it using the same algorithm as ADC trimming. Instead, a different approach is used for adjustment. The method described below

is currently the most optimal solution.

1. For each strip channel, the trimming value (i) from 0 to 63, and a pulse with an amplitude V_{fast} is input M times. The current setting for M is 111.

2. Record the count: $C(i)$ that exceeds the FAST threshold for each strip channel.

3. Create a plot `trim_s-curve` for each strip channel, where the horizontal axis is the trimming value: i and the vertical axis is the count: $C(i)$.

4. Smooth `trim_s-curve` to generate `trim_s-curve_sm`.

   (a) $\cancel{C_{sm}(i) = \{C(i-1) + C(i) + C(i+1)\}/3}$

   (b) $C_{sm}(i) = \{C(i-1) + C(i)\}/2$

5. Fit `trim_s-curve_sm` using an error function (Eq. C.1).

   (a) If the fit is successful, set the trimming value: i at which the fit function equals $M/2$ as `trim_best`. (or the fit function mean (μ) as `trim_best`.)

   (b) If the fit fails, set `trim_best` to the trimming value: i that corresponds to the count closest to $M/2$.

6. Set the trimming value to `trim_best`.

7. Perform a pscan **by 1 step** in the range of $V_{\text{fast}} \pm 20$ `amp_cal` to verify proper adjustment.

8. If there is significant noise, increase V_{fast} and restart from step ① Adjustment of `Thr2_glb`.

The S-curve created in Step 3 appears as the orange "x" marks in Figure C.6. A normal ASIC produces a single curve, as shown in the left plot, while some ASICs produce two curves, as shown in the right plot[1]. The purpose of the adjustment here is to eliminate the strip channel dependence of the FAST threshold. Therefore, adjustments are made by averaging between the two curves. To achieve this, the S-curve is smoothed.

In the algorithm used in the CBM experiment, the curve was smoothed by averaging the count at the current trimming value ($C(i)$) with the counts at the preceding ($C(i-1)$) and following ($C(i+1)$) trimming values. However, there was a tendency for the count values to fluctuate significantly with each change in the trimming value. Therefore, the smoothing was adjusted to average only the count at the current trimming value ($C(i)$) and the count at the preceding trimming value ($C(i-1)$). This smoothed value, $C_{sm}(i)$, is shown as the blue "o" marks in Figure C.6.

---

[1]However, it is clear that resolving the root cause of this issue would be preferable. The root cause is likely the decrease in VDDM (voltage value [mV] driving CSA). To resolve this issue, optimization such as adjusting the current of the CSA is considered necessary; however, a definitive method has not yet been established. This remains a challenge for future work.
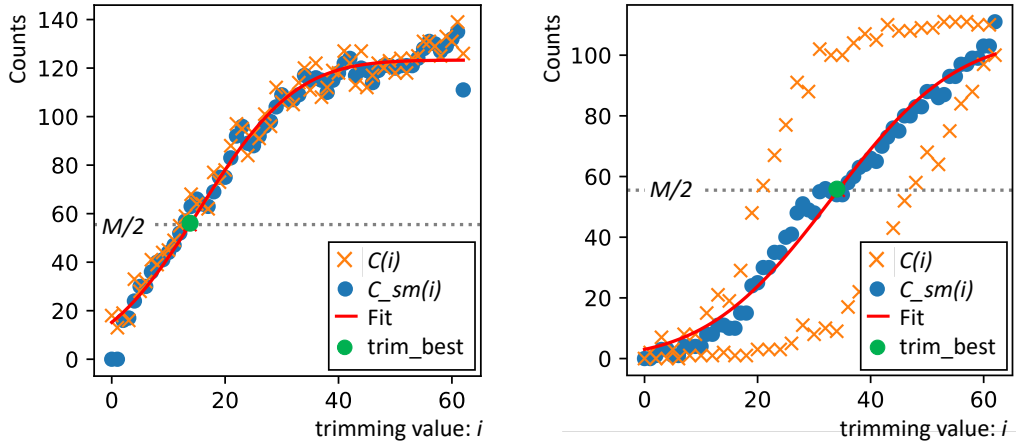
Figure C.6: Count values vs trimming values. The plot on the left shows an ASIC with a single S-curve, and the plot on the right shows an ASIC with two S-curves. The VDDM value of the ASIC on the right is relatively low.
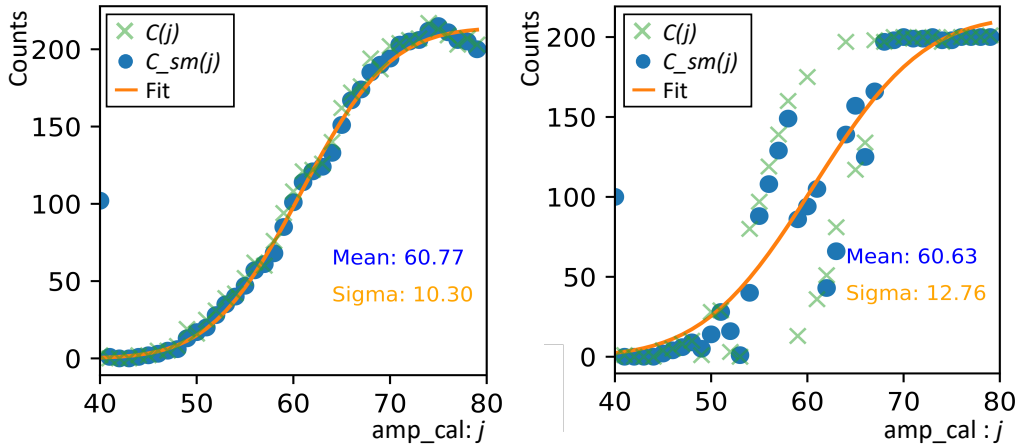

Figure C.7: Pscan of the FAST thresholds performed with `trim_best` set. The plot on the left shows an ASIC with a single S-curve, and the plot on the right shows an ASIC with two S-curves. The VDDM value of the ASIC on the right is relatively low.

The calculated $C_{sm}(i)$ is fitted using an error function (Eq. C.1). The trimming value at which the fitted function equals $M/2$ is defined as "`trim_best`". Although it is also possible to use the mean of the fitted error function as "`trim_best`", the current approach adopts the former method for now.

Set the trimming value to `trim_best` and perform a pscan (Figure C.7). To verify where the threshold is set, it is essential to scan by 1 step. At this stage, the focus should be on checking the position and shape of the S-curve for each strip channel, as well as its fluctuations (not limited to σ alone). Taking these factors into account, the next step (③) should be performed.

③ **Readjustment of Thr2_glb**

After the trimming DAC adjustment is completed, the channel dependence of the threshold is minimized. Once this is achieved, further adjustments to the threshold height are allowed only by modifying `Thr_glb2`, in the same way as $V_{\text{ref T}}$. The threshold shift corresponding to 1 LSB of `Thr_glb2` is nearly identical between the N-side (electrons) and P-side (holes), as shown below (Figure C.8).

$$1 \text{ [LSB]} = 0.047 \text{ [fC]} \sim 294 \, \text{e}^- \tag{C.12}$$

Since adjustments are often made by observing `amp_cal`, the conversion is noted here. If an adjustment of x [`amp_cal`] is desired, the corresponding values can be calculated as follows:

$$\text{Adjustment: } x \, [\texttt{amp\_cal}] \to x/0.84 \, [\text{LSB}] \tag{C.13}$$

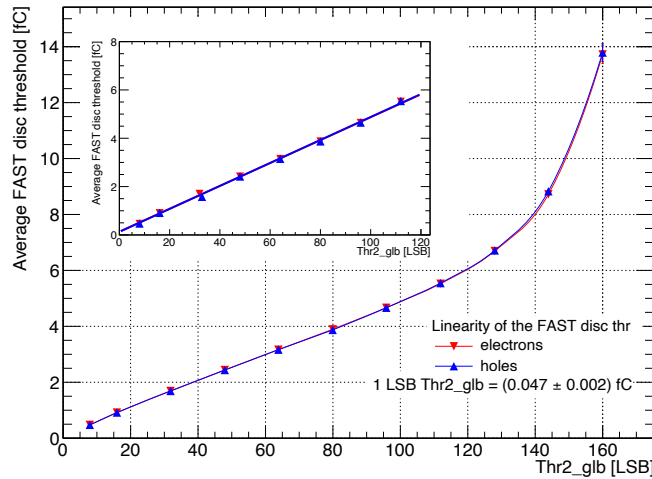This adjustment should be carried out carefully while checking the position of the threshold using ④ below.

Figure C.8: Thr2 glb register linearity [19].

④ **Confirming whether the FAST thresholds are set to the appropriate level.**

The FAST thresholds must be set significantly lower than the ADC thresholds. However, when `amp_cal` is below 40, noise increases, making it difficult to accurately determine the thresholds through pscan. I devised a method for checking the FAST thresholds by leveraging the principle in a counterintuitive way: if a hit is detected without exceeding the FAST threshold, the TDC of the previous hit is recorded instead. This method was established before Run-0e. The procedure for this method is as follows:

107

1. Input pulses of height equivalent to the lowest ADC threshold M times and perform data acquisition. The current setting for M is 200.

2. For each strip channel, plot the difference between the TDC of a given hit and the TDC of the previously recorded hit.

3. If a peak appears at zero in the TDC difference distribution, it confirms that the FAST threshold has not been lowered sufficiently (Figure C.9 left).

4. Additionally, by plotting the strip numbers of hits with a TDC difference of zero and creating a hit profile, it is possible to identify which channels have not had their thresholds sufficiently lowered (Figure C.9 right).
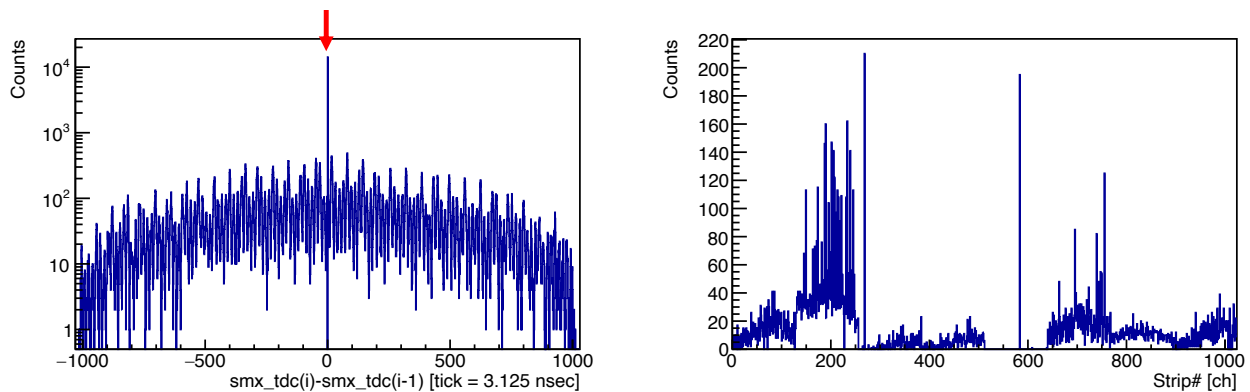

Figure C.9: FAST threshold confirming method. The left plot shows the distribution of the difference between the TDC of a given hit and the TDC of the previously recorded hit. The red arrow indicates the position where the difference is 0. The right plot shows the strip channels where the difference is 0. It can be observed that the ASIC around strip_ch = 200 has its FAST threshold set slightly higher than the ADC threshold.

Appendix D

Online trigger selection

As mentioned earlier in the text, the online trigger selection is performed in two stages: "coarse selection" and "fine selection". This chapter provides an explanation of these stages.

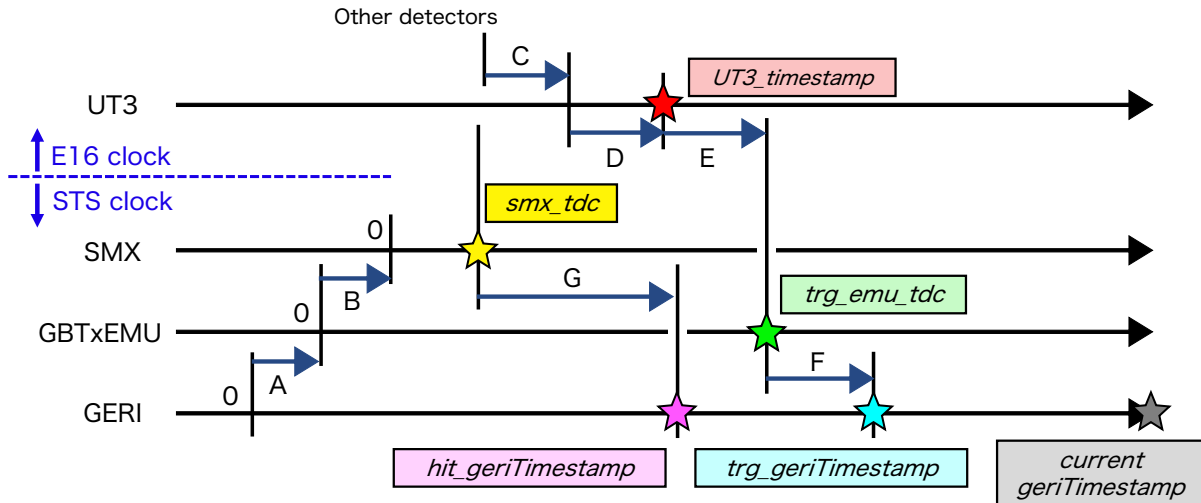Figure D.1: Illustration of time axes and event timing in the STS readout system (reposted).

Coarse selection

When no trigger is received Using `hit_geriTimestamp`⭐ and `current_geriTimestamp`⭐, old data is searched for and removed from the buffer.

When a trigger is received When trigger data is received, `trg_geriTimestamp`⭐ and `current_-geriTimestamp`⭐ are used to discard data without the defined search window. Additionally, the process of removing old hit data from the buffer is suspended while fine selection is being performed after receiving a trigger. The selection window, referred to as the "search window", has a width of several µsec to several tens of µsec and is used for hit selection.

Fine selection

The fine selection is performed on the data after the coarse selection using `smx_tdc` ⭐ and `trg_geriTimestamp` ⭐. The selection window, referred to as the "match window", has a width of several hundred nsec to a few μsec.
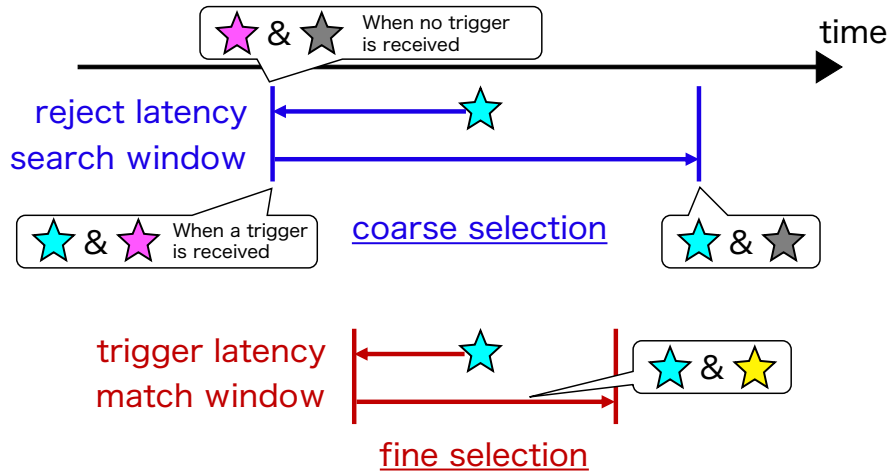
Figure D.2: The timestamps used for coarse selection and fine selection. The colors of the stars correspond to those in Figure D.1.

References

[1] Szabolcs Borsányi, Zoltán Fodor, Christian Hoelbling, Sándor D. Katz, Stefan Krieg, Claudia Ratti, and Kálmán K. Szabó. Is there still any T_c mystery in lattice QCD? Results with physical masses in the continuum limit III. Journal of High Energy Physics, 2010(9):073, September 2010. http://dx.doi.org/10.1007/JHEP09(2010)073.

[2] Szabolcs Borsányi, Zoltán Fodor, Christian Hoelbling, Sándor D. Katz, Stefan Krieg, and Kálmán K. Szabó. Full result for the QCD equation of state with 2+1 flavors. Physics Letters B, 730:99–104, 2014. https://www.sciencedirect.com/science/article/pii/S0370269314000197.

[3] L. McLerran and S. Reddy. Quarkyonic matter and neutron stars. Physical Review Letters, 122(12):122701, 2019. https://link.aps.org/doi/10.1103/PhysRevLett.122.122701.

[4] J. Xu. Revisiting the hyperon puzzle: implications of quarkyonic matter. arXiv preprint, 2023. https://arxiv.org/abs/2410.22758.

[5] Mark G. Alford, Andreas Schmitt, Krishna Rajagopal, and Thomas Schäfer. Color superconductivity in dense quark matter. Reviews of Modern Physics, 80(4):1455–1515, November 2008. http://dx.doi.org/10.1103/RevModPhys.80.1455.

[6] M. A. Stephanov. QCD PHASE DIAGRAM AND THE CRITICAL POINT. International Journal of Modern Physics A, 20(19):4387–4392, July 2005. http://dx.doi.org/10.1142/S0217751X05027965.

[7] Kenji Fukushima and Tetsuo Hatsuda. The phase diagram of dense QCD. Reports on Progress in Physics, 74(1):014001, dec 2010. https://dx.doi.org/10.1088/0034-4885/74/1/014001.

[8] Gert Aarts. Complex Langevin dynamics and other approaches at finite chemical potential, 2013. https://arxiv.org/abs/1302.3028.

[9] Owe Philipsen. Status of lattice studies of the qcd phase diagram. Progress of Theoretical Physics Supplement, 174:206–213, 2008. http://dx.doi.org/10.1143/PTPS.174.206.

[10] I. G. Bearden, D. Beavis, C. Besliu, Budick, et al. Nuclear Stopping in Au + Au Collisions at $\sqrt{s_{NN}} = 200$ GeV. Phys. Rev. Lett., 93:102301, Aug 2004. https://link.aps.org/doi/10.1103/PhysRevLett.93.102301.

[11] Masaharu Kitazawa and Teiji Kunihiro. Quark Matter under Extreme Conditions: Phase Transitions in the World of Elementary Particles. Frontiers in Physics, Volume 29. Kyoritsu Shuppan Co., Ltd., Tokyo, Japan, first edition edition, September 2022. Printed in Japan.

[12] Yasuyuki Akiba. Physics of Quark Plasma Gluon: Recreating Hot Matter in Early Universe in Laboratory. Frontiers in Physics, Volume 3. Kyoritsu Shuppan Co., Ltd., Tokyo, Japan, first edition edition, April 2014. Printed in Japan.

[13] K. Adcox, S.S. Adler, Afanasiev, et al. Formation of dense partonic matter in relativistic nucleus-nucleus collisions at RHIC: Experimental evaluation by the PHENIX Collaboration. Nuclear Physics A, 757(1-2):184–283, August 2005. http://dx.doi.org/10.1016/j.nuclphysa.2005.03.086.

[14] I. Arsene, I.G. Bearden, Beavis, et al. Quark-gluon plasma and color glass condensate at RHIC The perspective from the BRAHMS experiment. Nuclear Physics A, 757(1-2):1–27, August 2005. http://dx.doi.org/10.1016/j.nuclphysa.2005.02.130.

[15] D. Almaalol et al. QCD phase structure and interactions at high baryon density: Continuation of BES physics program with CBM at FAIR. arXiv preprint arXiv:2209.05009, 2022. arXiv:2209.05009 [nucl-ex] https://arxiv.org/abs/2209.05009.

[16] Tetyana Galatyuk. Future facilities for high µB physics. Nuclear Physics A, 982:163–169, 2019. The 27th International Conference on Ultrarelativistic Nucleus-Nucleus Collisions: Quark Matter 2018. https://www.sciencedirect.com/science/article/pii/S0375947418304172.

[17] Hans Gutbrod, Ingo Augustin, H. Eickhoff, K Groß, Walter Henning, D Krämer, and G Walter. FAIR Baseline Technical Report. 01 2006. https://www.researchgate.net/publication/230785058_FAIR_Baseline_Technical_Report.

[18] J.M. Heuser, W.F.J. Müller, V. Pugatch, P. Senger, C.J. Schmidt, C. Sturm, and U. Frankenfeld. Technical Design Report for the CBM Silicon Tracking System (STS). Technical Report GSI Report 2013-4, GSI, City, Country, 2013. https://repository.gsi.de/record/54798/.

[19] Adrian Rodríguez Rodríguez. The CBM Silicon Tracking System front-end electronics: from bare ASIC to detector characterization, commissioning and performance. Dissertation, Johann Wolfgang Goethe-Universität, Frankfurt am Main, Frankfurt am Main, Germany, 2019. zur Erlangung des Doktorgrades der Naturwissenschaften.

[20] Ionut-Cristian Arsene, L. Bravina, W. Cassing, Yu Ivanov, A. Larionov, Jorgen Randrup, V. Russkikh, Viacheslav Toneev, Gebhard Zeeb, and Detlef Zschiesche. Dynamical phase trajectories for relativistic nuclear collisions. Physical Review C, 75:034902, 03 2007. https://journals.aps.org/prc/abstract/10.1103/PhysRevC.75.034902.

[21] GSI Helmholtzzentrum für Schwerionenforschung. Mini-CBM Experiment, 2025. https://www.gsi.de/work/forschung/cbmnqm/cbm/activities/mcbm Accessed: 2025-01-18.

[22] 佐甲 博之 and 原田 寛之. 高密度クォーク物質探索の展望と J-PARC-HI (Future Prospects of Research on High-Baryon Density Quark Matter and J-PARC-HI). Journal of Plasma and Fusion Research, 100(6):266–273, 2024. https://www.jspf.or.jp/Journal/PDF_JSPF/jspf2024_06/jspf2024_06-266.pdf.

[23] William R. Leo. Techniques for Nuclear and Particle Physics Experiments: A How-to Approach. Springer-Verlag Berlin Heidelberg, Berlin, Heidelberg, second revised edition edition, 1994.

[24] Hamamatsu photonics K.K. Si detectors for high energy particles. Technical report, Hamamatsu photonics, 2021. https://www.hamamatsu.com/content/dam/hamamatsu-photonics/sites/documents/99_SALES_LIBRARY/ssd/high_energy_kspd9002e.pdf.

[25] K. Kasinski, W. Zabolotny, R. Szczygiel, W. Zubrzycka, A. Rodriguez-Rodriguez, J. Lehnert, and C. J. Schmidt. SMX2.0, SMX2.1, SMX2.2 Manual v4.00. Technical report, AGH University of Science and Technology Cracow, Warsaw University of Technology, GSI Helmholtzzentrum für Schwerionenforschung, 2021.

[26] M. Dogan, R. Kapell, J. Lehnert, A. Lymanets, A.R. Rodriguez, C.J. Schmidt, and C. Simons. Quality assurance test of the STS-XYTERv2 ASIC for the silicon tracking system of the CBM experiment. Nuclear Instruments and Methods in Physics Research Section A: Accelerators, Spectrometers, Detectors and Associated Equipment, 976:164278, 2020. https://www.sciencedirect.com/science/article/pii/S0168900220306744.

[27] Tetsuo Hatsuda and Teiji Kunihiro. QCD phenomenology based on a chiral effective Lagrangian. Physics Reports, 247(5):221–367, 1994. https://www.sciencedirect.com/science/article/pii/0370157394900221.

[28] W. Weise. Nuclear aspects of chiral symmetry. Nuclear Physics A, 553:59–72, 1993. https://www.sciencedirect.com/science/article/pii/0375947493906155.

[29] Y. Nambu and G. Jona-Lasinio. Dynamical Model of Elementary Particles Based on an Analogy with Superconductivity. I. Phys. Rev., 122:345–358, Apr 1961. https://link.aps.org/doi/10.1103/PhysRev.122.345.

[30] Tetsuo Hatsuda and Su Houng Lee. Qcd sum rules for vector mesons in the nuclear medium. Phys. Rev. C, 46:R34–R38, Jul 1992. https://link.aps.org/doi/10.1103/PhysRevC.46.R34.

[31] Philipp Gubler and Keisuke Ohtani. Constraining the strangeness content of the nucleon by measuring the ϕ meson mass shift in nuclear matter. Phys. Rev. D, 90:094002, Nov 2014. https://link.aps.org/doi/10.1103/PhysRevD.90.094002.

[32] M. et al. Naruki. Experimental Signature of Medium Modifications for ρ and ω Mesons in the 12 GeV $p + A$ Reactions. Phys. Rev. Lett., 96:092301, Mar 2006. https://link.aps.org/doi/10.1103/PhysRevLett.96.092301.

[33] R. et al. Muto. Evidence for In-Medium Modification of the ϕ Meson at Normal Nuclear Density. Phys. Rev. Lett., 98:042501, Jan 2007. https://link.aps.org/doi/10.1103/PhysRevLett.98.042501.

[34] J-PARC Center. J-PARC Photo Gallery, 2024. http://j-parc.jp/c/photo_gallery/index.html Accessed: 2024-12-10.

[35] S. Yokkaichi and et al. Addendum to the J-PARC E16 Technical Design Report for Run-1 approval. Technical report, J-PARC, jun 2022. Run-1 Approval Document.

[36] T. N. Murakami. Development and construction of GEM tracker system for the J-PARC E16 experiment, 2020. https://indico2.riken.jp/event/3353/contributions/14087/attachments/9222/11966/Murakami_master.pdf.

[37] LCTPC Collaboration. Gas Electron Multipliers, 2025. `https://www.lctpc.org/e8/e46/e47/` Accessed: 2025-01-15.

[38] Y. Giomataris and G. Charpak. Nuclear Instruments and Methods in Physics Research Section A: Accelerators, Spectrometers, Detectors and Associated Equipment. Nuclear Instruments and Methods in Physics Research Section A, 310(3):589–595, 1991.

[39] W. Anderson and et al. Nuclear Instruments and Methods in Physics Research Section A: Accelerators, Spectrometers, Detectors and Associated Equipment. Nuclear Instruments and Methods in Physics Research Section A, 646(1):35–58, 2011.

[40] S. Nakasuga. 電子対測定のための粒子識別検出器群における背景事象除去性能の評価, 2021. `https://indico2.riken.jp/event/3676/contributions/15905/attachments/10038/14158/master_nakasuga_final.pdf`.

[41] D. Arimizu. J-PARC E16 実験での飛跡検出に用いるシリコン半導体検出器の性能評価, 2022. `https://www-nh.scphys.kyoto-u.ac.jp/articles/thesis/mron/2021/arimizu_master.pdf`.

[42] K. Yamaguchi. J-PARC E16 実験での飛跡検出に用いるシリコンストリップ検出器の読み出し回路の開発, 2023. `https://indico2.riken.jp/event/4428/sessions/1817/attachments/11852/17159/master_thesis_final_yamaguchi.pdf`.

[43] M. Barros Marin, S. Baron, S. S. Feger, P. Leitao, E. S. Lupu, C. Soos, P. Vichoudis, and K. Wyllie. The GBT-FPGA core: features and challenges. Journal of Instrumentation, 10(03):C03021, mar 2015.

[44] Institute of Materials Structure Science KEK. Beamlines of Photon Factory, 2024. `https://www2.kek.jp/imss/pf/eng/apparatus/bl/` Accessed: 2025-01-15.

[45] Institute of Materials Structure Science KEK. Photon Accelerator, 2024. `https://www2.kek.jp/imss/pf/apparatus/acc/` Accessed: 2025-01-15.

[46] Toru Honda, Yoichi Ikegami, and Takashi Uchiyama. Design of the GeV range test beamline at the PF-AR. In Proceedings of the 18th Annual Meeting of Particle Accelerator Society of Japan, page 998, Japan, 2021. `https://inis.iaea.org/search/search.aspx?orig_q=RN:53086766`.

[47] Y. Okazaki. Beam profiles of PF-AR test beamline, 2024. `https://wiki.kek.jp/pages/viewpage.action?pageId=411961546` Accessed: 2025-01-15.

[48] Lawrence D. Brown, T. Tony Cai, and Anirban DasGupta. Interval Estimation for a Binomial Proportion. Statistical Science, 16(2):101 – 133, 2001. `https://doi.org/10.1214/ss/1009213286`.

[49] Takuro Kimura, Katsuya Okamura, Yoshihisa Shirakabe, Tetsushi Shimogawa, Masahito Tomizawa, Hidetoshi Nakagawa, Ryotaro Muto, Eiichi Yanaoka, and Akio Kiyomichi. The Research of Spill Structure for J-PARC Slow Extraction. In Proceedings of the 10th Annual Meeting of Particle Accelerator Society of Japan, pages 1130–1133, Nagoya, Japan, August 3-5 2013. In Japanese `https://www.pasj.jp/web_publish/pasj10/proceedings/PDF/SUP0/SUP087.pdf`.

[50] A. Rodríguez Rodríguez, O. Maragoto Rodríguez, J. Lehnert, A. Toia, M. Teklishyn, A. Lymanets, D. Rodríguez Garcés, J.M. Heuser, and C.J. Schmidt. Functional characterization of modules for the Silicon Tracking System of the CBM experiment. Nuclear Instruments and Methods in Physics Research Section A: Accelerators, Spectrometers, Detectors and Associated Equipment, 1058:168813, 2024. https://www.sciencedirect.com/science/article/pii/S0168900223008045.